UNIVERSITÀ DEGLI STUDI DI CAMERINO

School of Advanced Studies

DOCTORAL COURSE IN

SCIENCES AND TECHNOLOGY PHYSICAL AND CHEMICAL PROCESSES IN EARTH SYSTEMS

XXXIII Cycle

UNMANNED AERIAL VEHICLE (UAV) AND GROUND-BASED STRUCTURE FROM MOTION PHOTOGRAMMETRY FOR STRATIGRAPHIC AND STRUCTURAL ANALYSIS

PhD Student
Alan David Pitts

Supervisors
Prof. Claudio Di Celma
Prof. Emanuele Tondi

Table of Contents

Abstract---------- 3

1. Introduction---------- 4

2. Photogrammetry in Geoscience---------- 8

3. *Integrating traditional field methods with emerging digital techniques for enhanced outcrop analysis* – Published in Journal of Marine and Petroleum Geology 2017---------- 17

4. *Detailed outcrop characterization of high frequency sequence boundaries in the Pliocene Peri-Adriatic shallow marine succession revealed through UAV cliff-side digital outcrop mapping*. Published in the International Association of Sedimentologists Field Trip Guide A4 2019---------- 42

5. *Sedimentological and Stratigraphic signature of the Plio-Pleistocene tectonic events in the Southern Apennines, Italy. The Calvello Basin case study*. Published in the Journal of Marine and Petroleum Geology---------- 62

6. Analysis of fracture roughness control on permeability using SfM and fluid flow simulations: Implications for carbonate reservoir characterization ---------- 105

7. Discussion and Conclusions---------- 151

8. Acknowledgements----------

Abstract

Structure from Motion (SfM) is a recently developed tool for advanced topographic surveys. This technique may be applied either from airborne or ground-based platforms. This new innovative approach has become a more accessible, cost-effective, and practical means of produce high quality 3D outcrop and geological models, which were traditional produced using expensive and highly technical laser scanning technology. This work illustrates four case studies in which aerial-based SfM photogrammetry has been used as a complementary data acquisition tool, in order to enhance and calibrate other data sets, and in an effort to build a more complete interpretation of stratigraphic and structural outcrop features. The results of these studies apply directly to the fields of sedimentology/stratigraphy, field mapping, basin analysis, and reservoir characterization. Furthermore, these studies apply this technique to geological aspects ranging in scale from millimeter variations of fracture surface topography, to centimeter-scale sedimentary structures, to decameter scale outcrop geometries.

Chapter

1

Introduction

1.1 Introduction

High resolution 3D outcrop and rock data provides a new powerful tool for describing and measuring physical parameters in geoscience (McCaffrey et al., 2005, Bemis et al., 2014). Methods for obtaining 3D outcrop datasets have traditionally involved the use of Light Detection and Ranging (LIDAR), either airborne or ground-based, and other laser scanning technologies. More recently, however, the substantial advancements in the field of Structure from Motion (SfM) photogrammetry offer a means to produce datasets with nearly the same quality as the often more expensive laser technologies. The SfM approach represents a platform for 3D data collection which is more flexible, more cost-efficient, and applicable to a wider range of geoscience disciplines.

While this tool has been designed to serve many different applications in geosciences, with several case studies documenting its utility at multiple scales, there has not yet been a comprehensive study to test the true scale-independent limitations of the technology. Such a study should incorporate millimeter-scale utilization, focused on objects that are at the interface between microscopic and macroscopic rock features, centimeter-scale outcrops, and the architecture of basin-scale structures.

The goal of this thesis is to use unmanned aerial vehicle (UAV) and ground-based SfM as **complimentary data acquisition and analysis tools** that can help calibrate and enhance other stratigraphic and structural datasets. This study presents four specific case studies, which fall into two general categories of sedimentological and stratigraphic analysis, followed by two works focused on structural analysis at both the large scale, aimed at basin analysis, and the micro-scale, looking into fracture surface topography control on reservoir characterization.

The following **Chapter 2**, *Structure from Motion in Geoscience,* provides a general background, covering the fundamentals of SfM workflows and the relevancy to geoscience research.

Chapter 3 details an application of ground-based and aerial photogrammetry for enhanced facies analysis, in the article by Pitts et al., 2017, titled *Integrating traditional field methods*

with emerging digital techniques for enhanced outcrop analysis of deep-water channel-fill deposits, published in the Journal of Marine and Petroleum Geology. This work illustrates the utility and capability of applying both SfM photogrammetry and Gigapixel imagery to supplement traditional field methods, as an improvement and enhancement on existing techniques. The main results of this work illustrate an enhanced protocol for characterizing physically inaccessible stratigraphic sections of deep-water deposits from the Gorgoglione Flysch Formation in the Southern Apennine chain, Basilicata, Italy.

Chapter 4 presents a case study, titled *Detailed outcrop characterization of high-frequency sequence boundaries in the Pliocene Peri-Adriatic shallow marine succession revealed through UAV cliff-side digital outcrop mapping*, and describes the use of UAV-acquired drone imagery to characterize cliff-side outcrops in the Plio-Pleistocene Peri-Adriatic basin of the Apennines, beneath the town of Montefalcone Appennino. This study shows how the technique helps bring geologists' "noses to the outcrop" of physically inaccessible vertical successions, to investigate the centimeter-scale bedding features that help reconstruct the sequence stratigraphic framework and interpretations of high-frequency change in base level. In this study, the UAV-acquired imagery and 3D outcrop reconstructions served as the primary investigative tool for building the stratigraphic framework which provided the fundamental understanding, launching further studies focused on provenance by heavy mineral analysis and depositional history. The work was published in the volume as a portion of the Field Trip Guide A4 at the International Association of Sedimentologists in Rome, 2019.

Chapter 5 is a case study, titled *Sedimentological and Stratigraphic signature of the Plio-Pleistocene tectonic events in the Southern Apennines, Italy. Calvello Basin case study*. This work was published in the Journal of Marine and Petroleum Geology, and demonstrates the addition of UAV-based SfM as an aid for bedrock geologic mapping. In this case, the SfM approach was used to search for additional outcrops in the mapping area, several of which were scanned to produce digital outcrop models (DOMs) for extraction of physical outcrop data and evaluation of stratigraphic architecture.

The final case study, Chapter **6,** is comprised of a study using SfM photogrammetry in a highly controlled laboratory setting, applied to millimeter-scale features affecting reservoir

quality, including fracture surface micro-topography. This featured as a published article, titled *Analysis of Fracture Roughness Control on Permeability Using SfM and Fluid Flow Simulations: Implications for Carbonate Reservoir Characterization.* Samples for this work were selected from the Mesozoic carbonate grainstones of the Majella Mountain succession, which are active source rocks for hydrocarbons in which bitumen seeps are controlled by the presence of large-scale faults and lower-order fracture networks. These provide fluid migratory pathways in rocks that are otherwise impermeable. This study incorporates fluid flow simulations, using the Lorentz-Boltzmann equation, and the use of synthetic computer-generated fractures for estimation of the joint roughness coefficient. The quantitative analysis of fault surface roughness was achieved by implementing the power spectral density (PSD), which provides an objective description of the roughness, based on the frequency distribution of the asperities in the Fourier domain. The positive results from this study have led to additional research focused on the same topic, however, applying the technique to a more diverse suite of lithologies and rock types, using opening fractures, shear fractures and more data points, to improve the representativeness of the initial results.

Chapter 7, draws conclusions, summarizes, and critically discusses the main findings of the research, and reflects on future works.

Chapter

2

Structure from Motion in Geosciences

Introduction

This chapter provides a brief introduction to SfM photogrammetry and its relevance to geoscience research, while comparing it with other laser scanning technologies. Photogrammetry protocols are further described in Chapter 4, for ground-based and aerial photo acquisition, and Chapter 6, for lab-based procedures.

Structure from Motion (SfM), used as a shorthand for the longer and more technical term, Structure from Motion Multi-View Stereo (SfM-MVS), is an analytical surface scanning tool, used to create 3D volumes and topographic data from sets of individual overlapping 2D photos. SfM represents one of the most recent and emerging tools for 3D data acquisition, which has shown great flexibility (Westoby et al., 2012; Carrivick et al., 2013; Tavani et al., 2014; Bilmes et al., 2019). However, there are several other platforms and digital survey techniques that are also widely used, such as LIDAR and other laser scanning tools.

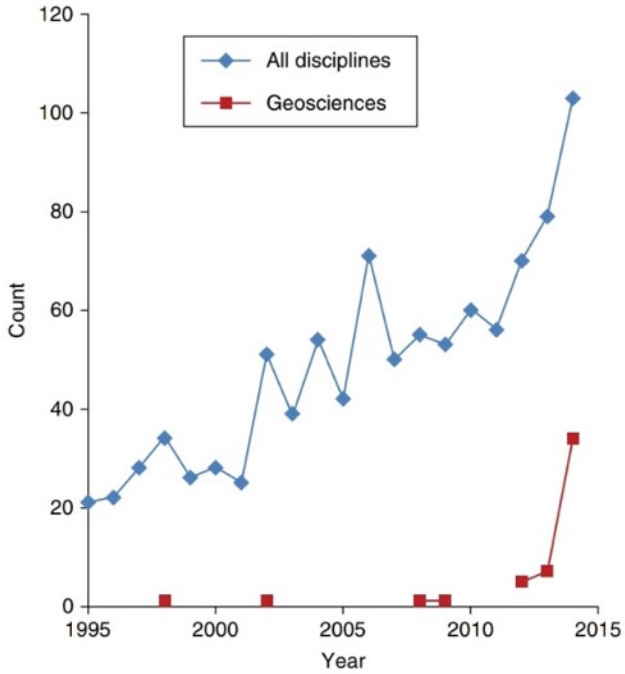

Figure 2.1. Search in Web of Knowlegde for articles included SfM photogrammetry in their titles.

Over a period from 1995 - 2015, SfM photogrammetry has seen a huge growth in geoscience literature (Fig.2.1), with search terms in academic literature over a 3-year period showing a

sharp increase. This roughly corresponds to dramatic improvements in “off the shelf”, commercial grade, SfM technology. This approach has been successfully employed from various platforms including Unmanned Aerial Vehicle- (UAV), Balloons, fixed-wing small aircraft, ground-based, and within fixed lab conditions (Fig 2.2). SfM has grown from being once considered a novel and experimental imaging technique to become well-recognized as a powerful tool for quantitative remote data acquisition, greatly enhancing traditional physical field, and laboratory-derived, datasets in a wide range of geoscience applications. In recent years, this type of technology has been applied to a wide range of topics, including sedimentary facies characterization in deep water systems (Pitts et al., 2017), fault and fold analysis (Corradetti et al., 2017; Volatili et al., 2017), surface fault rupture characterization (Johnson et al., 2014), paleontological analysis (Zimmer et al., 2018), and fracture surface roughness and microtopography analysis (Zambrano et al., 2019).

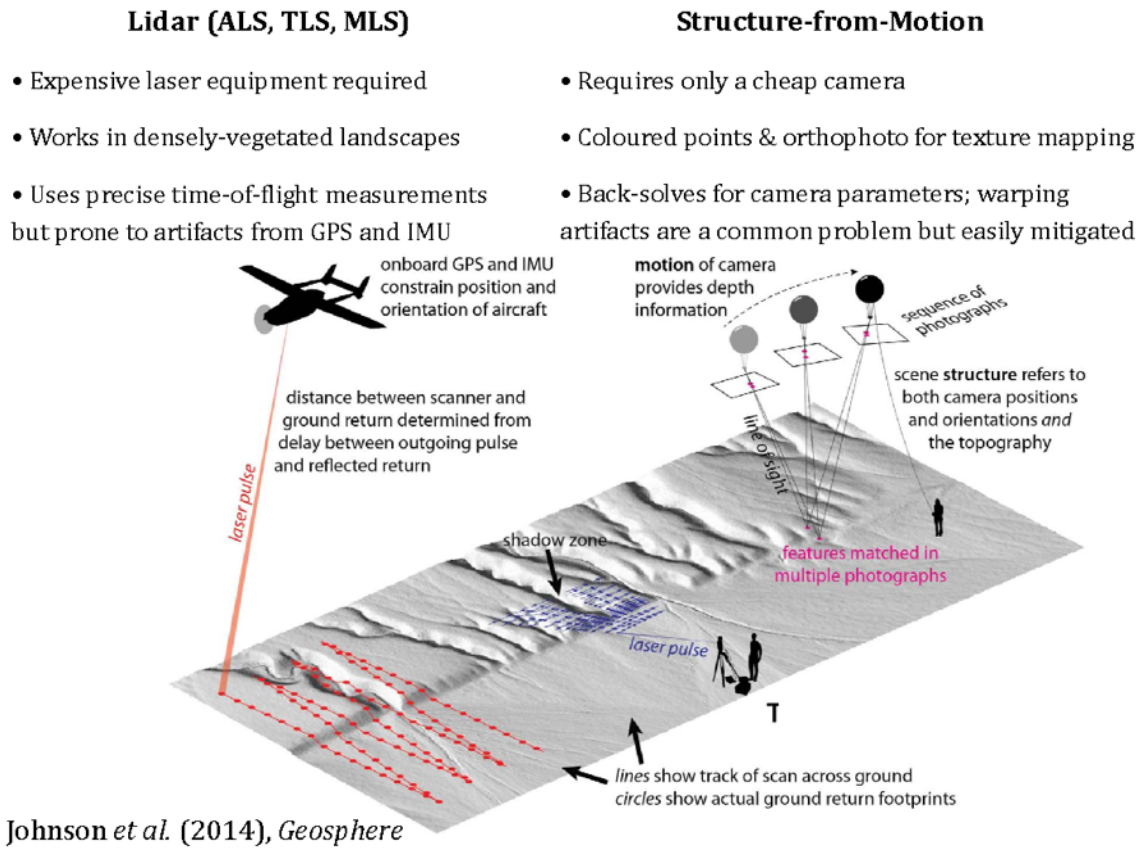

Figure 2.2. Illustration showing terrestrial and aerial laser scanning and aerial-based SfM (from John et al., 2014).

SfM technology was born from standard photogrammetry, which has been present in geoscience for several decades (Chandler, 1999; Lane et al., 2000). However, this procedure is very rigid in that it requires very precise input parameters. Standard photogrammetry involves using photos taken from known and measured locations, with very strict overlap requirements and precise locations of tie-points. This process is extremely laborious and it is time consuming to create the final digital elevation model. These processes primarily use overhead aerial images which are taken perpendicular to the surface of interest.

This type of analysis is related to the classical approach that has been commonly used for several decades to create “stereographic photo pairs” (Fig 2.3). Constructing stereographic images is primarily achieved by assembling pairs of overlapping and adjacent aerial photos, with each photo providing a slightly different view of the object. When observed through a special device called a stereoscope, these photos give the viewer a 3D perspective on the object.

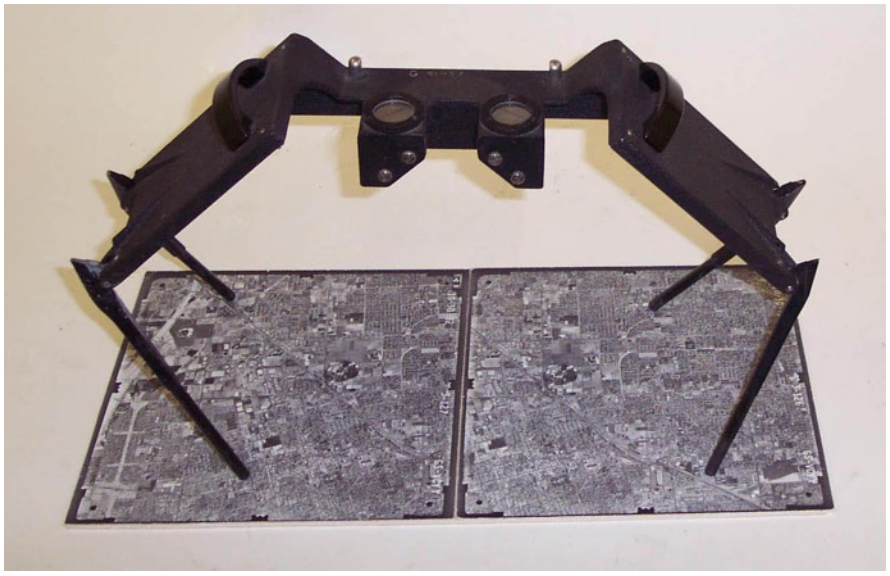

Figure 2.3. Stereoscope used to view stereo-pair photos. Image courtesy of USGS

The utility of stereographic photo-pairs, however, is very limiting. They do provide a means to qualitatively appreciate terrain features and landscapes, which can be used to make very broad-scale interpretations – something that may not be possible from normal aerial photos. However, stereographic photo-pairs are largely an antiquated tool, primarily used by introductory geomorphology/physical geography students, since computer-based geo-imager

viewers like Google Earth have largely replaced fixed image analysis. Additionally, since photo stereo-pairs only provide an “apparent” three-dimensional view, it is not possible to take quantitative data from them or to use them for serious data acquisition.

SfM-MVS photogrammetry is instead a workflow that involves using series of photos taken from multiple locations and random orientations from the surface, including normal to the object of interest and also from an oblique position. Rather than the time-consuming procedure in standard photogrammetry, SfM uses software that calculates camera position, orientation, and tie points, automatically, without the need for a user to indicate the specific details.

In contrast, LIDAR is the modern standard for collecting 3D digital outcrop data. This technique is used either from an aircraft, as Aerial LIDAR Scanning (ALS), or from the ground, known as Terrestrial LIDAR Scanning (TLS) (Johnson et al., 2014). In either case, to acquire this type of data is extremely costly. Currently, an entry level TLS system costs upwards of $85,000, after which there could be associated costs for the training of staff and upkeep for the equipment. ALS, on the other hand can cost much more, as the survey has to be produced by a trained pilot along with an instrument operator onboard with scanning equipment. The costs of this type of data acquisition implies that only research institutes with large research budgets can afford to purchase of hire LIDAR scanning for research.

The main advantages of SfM in comparison to other methods is primarily the cost. SfM is the most cost effective in terms of equipment, labor costs, and software for processing and analysis. As a comparison to LIDAR, and other digital geologic field data and point cloud generation, SfM procedures are very competitive. One small drawback is that SfM functions over shorter ranges than LIDAR, since the images have a limited focal range. However, mounting cameras on UAVs provides a solution that can allow a spatial extent of several kilometers, similar to LIDAR ranges. Equally, it can produce datasets which have a resolution very close in data density to LIDAR. Generally, this represents a slightly reduced range to that of LIDAR, however using drone mounted cameras can resolve this problem.

Table 2.3 Summary of properties and pros and cons of different digital survey methods.

Survey equipment and workflow	Typical spatial extent (km)/ typical spatial resolution (pt.m²)	Possible data acquisition rate (points per hour)	Possible 3D point accuracy (m)	Advantages	Disadvantages
TS	0.1–1.0/0.1–5.0	Hundreds	<0.001	Low cost Accurate	Line of sight required Low productivity Accuracy decreases with distance from base
dGPS	2.4–1.0/0.1–5.0	Thousands	0.005	High accuracy Range of methods have been developed to suit different surveying requirements Line of sight not required	High cost Some methods have low productivity Lock on 6+ satellites required
Photogrammetry	5.0–50.0/ 0.5–10.0	Tens of thousands	0.5	High productivity Once set up, no operator required Continuous information can be captured	Low resolution Equipment must be left in position for long periods of time (depending on survey) and may be vandalised or damaged Does not work in fog, mist, etc.
ALS	5.0–100.0/ 0.2–10.0	Millions	0.2	High productivity Can be used during the night Airborne LiDAR can survey areas that are difficult to access Not affected by vegetation cover	Very high cost Resolution may be insufficient to measure small changes Systematic errors on some landforms
TLS	0.01–5.0/ 100–10,000	Millions	0.05	High accuracy	Unable to capture all aspects of complex topographies (depending on equipment positioning)
SfM	0.01–1.0/ 1–10,000	Millions	0.01–0.2	Cheap Fast Method is independent of spatial scale	Reproducibility? Reliability?

Figure 2.4. Advantages and disadvantages adapted from Young (2015). Extent and resolution vales from Bangen et al. (2014). Table from Carrivick et al. 2016

Other advantages of SfM over ALS and TLS are shown in the data resolution for possible 3D point count accuracy in meters (Fig 2.4). In this case, SfM shows greater resolution than both TLS and ALS due to its greater flexibility in range, being able to move from distant and close ranges to the object in question.

Other advantages of SfM over ALS and TLS are shown in the data resolution for possible 3D point count accuracy in meters (Fig 2.4). In this case, SfM shows greater resolution than both TLs and ALS due to its greater flexibility in range being able to move from distant and close ranges to the object in question.

References:

Bangen, S.G., Wheaton, J.M., Bouwes, N., Bouwes, B. & Jordan, C. (2014) A methodological intercomparison of topographic survey techniques for characterizing wadeable streams and rivers. *Geomorphology*, **206**, 343‐361.

Bemis, S. P., Micklethwaite, S., Turner, D., James, M. R., Akciz, S., Thiele, S. T., & Bangash, H. A. (2014). Ground-based and UAV-Based photogrammetry: A multi-scale, high-resolution mapping tool for structural geology and paleoseismology. *Journal of Structural Geology*, *69*(PA), 163–178. Retrieved from http://dx.doi.org/10.1016/j.jsg.2014.10.007

Bilmes, A., D'Elia, L., Lopez, L., Richiano, S., Varela, A., Alvarez, M. del P., … Ariztegui, D. (2019). Digital outcrop modelling using "structure-from- motion" photogrammetry: Acquisition strategies, validation and interpretations to different sedimentary environments. *Journal of South American Earth Sciences*, *96*(July), 102325. https://doi.org/10.1016/j.jsames.2019.102325

Carrivick, J.L., Smith, M.W., Quincey, D.J. & Carver, S.J. (2013a) Developments in budget remote sensing for the geosciences. *Geology Today*, **29** (**4**), 138‐143.

Corradetti, A., McCaffrey, K., De Paola, N., & Tavani, S. (2017). Evaluating roughness scaling properties of natural active fault surfaces by means of multi-view photogrammetry. *Tectonophysics*, *717*, 599–606. https://doi.org/10.1016/j.tecto.2017.08.023

Johnson, K., Nissen, E., Saripalli, S., Arrowsmith, J. R., McGarey, P., Scharer, K., … Blisniuk, K. (2014). Rapid mapping of ultrafine fault zone topography with structure from motion. *Geosphere*, *10*(5), 969–986. https://doi.org/10.1130/GES01017.1

Tavani, S., Granado, P., Corradetti, A., Girundo, M., Iannace, A., Arbués, P., Mazzoli, S. (2014). Building a virtual outcrop, extracting geological information from it, and sharing the results in Google Earth via OpenPlot and Photoscan: An example from the Khaviz

Anticline (Iran). *Computers and Geosciences*, *63*, 44–53. https://doi.org/10.1016/j.cageo.2013.10.013

Westoby, M.J., Brasington, J., Glasser, N.F., Hambrey, M.J. & Reynolds, J.M. (2012) "Structure‐from‐Motion" photogrammetry: a low‐cost, effective tool for geoscience applications. *Geomorphology*, **179**, 300‐314.

Young, E.J. (2013) Section 2.1.3: dGPS. In: S.J. Cook, L.E. Clarke & J.M. Nield (eds), *Geomorphological Techniques (Online Edition)*. British Society for Geomorphology, London.

Zimmer, B., Liutkus-pierce, C., Marshall, S. T., Hatala, K. G., Metallo, A., & Rossi, V. (2018). Using differential structure-from-motion photogrammetry to quantify erosion at the Engare Sero footprint site , Tanzania. *Quaternary Science Reviews*. https://doi.org/10.1016/j.quascirev.2018.07.006

Chapter

3

Integrating traditional field methods with emerging digital techniques for enhanced outcrop analysis of deep-water channel-fill deposits

Marine and Petroleum Geology
Volume 87, November 2017, Pages 2-13

Research paper

Integrating traditional field methods with emerging digital techniques for enhanced outcrop analysis of deep water channel-fill deposits

Alan D. Pitts [a], Claudio Ivan Casciano [a], Marco Patacci [b], Sergio G. Longhitano [c], Claudio Di Celma [a], William D. McCaffrey [b]

[a] Scuola di Scienze e Tecnologie, Sezione di Geologia, Università degli Studi di Camerino, Via Gentile III da Varano 1, 62032 Camerino, MC, Italy
[b] Turbidites Research Group, School of Earth and Environment, University of Leeds, Leeds LS2 9JT, UK
[c] Dipartimento di Scienze, Università degli Studi della Basilicata, Campus di Macchia Romana, 85100 Potenza, Italy

Preface:

This chapter presents a published study in its pre-journal format. This work comprises an integrated approach combining field stratigraphic methods, aerial and ground based SfM, and giga-pixel imagery to create an enhanced workflow for characterizing facies distributions in channelized turbidite systems.

The results of this study provide an initial methodology and point for further investigations which incorporate similar methods.

Integrating traditional field methods with emerging digital techniques for enhanced outcrop analysis of deep water channel-fill deposits

Pitts, A.D[1]., Casciano, C.I[1]., Patacci, M[2]., Longhitano, S.G[3]., Di Celma, C[1]., McCaffrey; W.D[2].

1. University of Camerino School of Science and Technology Geology Division
2. University of Leeds School of Earth and Environment, Turbidites Research Group,
3. University of Basilicata Department of Geological Sciences

Corresponding Author – Alan Pitts: alan.pitts@unicam.it

Published in Marine and Petroleum Geology 2017 (Vol. 87, pg. 2-13)

Abstract

The development of emerging digital technologies that allow the collection and analysis of field data represents a significant innovation in field-based geological studies. The integration of these digital techniques to traditional sedimentological field methods determines considerable improvements in outcrop characterization of ancient successions. An example of this integrated modern approach for geological data collection is employed for the detailed characterization of a turbidite channel-lobe system of the Gorgoglione Flysch Formation in Southern Italy. The studied section, exposed above the village of Castelmezzano, has been measured and described in detailed stratigraphic sections, providing data for both sedimentological analysis and correlation of the stratigraphy. In order to gain a complete perspective on the exposure and stratigraphic elements, analysis of physical outcrop data was enhanced by the use of high-resolution Gigapixel imagery and 3D photogrammetric outcrop reconstructions. The Santa Maria section has been assessed in terms of vertical and lateral facies stacking arrangements and subdivided into two component facies associations separated by a prominent concave-up erosional boundary. The lower facies association, interpreted as a frontal lobe complex, consists of tabular, thick-bedded coarse sandstones interbedded with persistent heterolithic packages of thin-bedded sandstones and mudstones, and minor soft-sediment deformed strata. The upper facies association represents the infill of a channel-form and consists of a basal conglomerate, passing gradually upwards into massive amalgamated sandstones overlain by large-scale cross-laminated sandstones. The excellent exposure of the Santa Maria section records the complete evolution of a channel-lobe system, transiting from frontal lobe deposition through channel incision and bypass, to progressive backfilling. This study shows how facies characterization, stratigraphic

correlations and reconstruction of the depositional architectures have been substantially enhanced by the use of emerging digital techniques for geological data collection.

1. Introduction

The improved capabilities of Gigapixel imagery systems and 3D photogrammetry software suites in recent years provide useful tools that can strengthen traditional stratigraphic field data. Gigapixel imagery systems are able to record very high resolution photomosaics, which allow an unprecedented level of inspection of outcrops, while photogrammetry software, such as Agisoft Photoscan allows 3D outcrop reconstructions from ground-based or aerial photos to be manipulated and viewed from multiple angles. These tools can fill critical gaps in stratigraphic data by permitting the inspection of both bed-scale and outcrop-scale details from distances and angles unachievable in person.

Turbidite channels are one of the most important pathways for sediment transport into ocean basins and their sedimentary infill has proven to be one of the most common types of hydrocarbon reservoirs found in deep water settings (e.g. Mayall et al., 2006). Seismic stratigraphy applied to conventional and high-resolution three-dimensional (3D) data sets offered a compelling method to understanding their internal stratal and architectural complexity (Mayall and Stewart, 2000; Posamentier and Kolla, 2003; Deptuck et al., 2003). However, a high degree of spatial variability of reservoir properties is associated with differences in the nature of channel fill and their stacking patterns occurring at scales below the resolution of 3D seismic datasets. Over the past years, to improve the sub-seismic characterization of submarine channel fills, numerous studies have focused on the details of suitable outcrop analogues, greatly improving our knowledge on distribution of sedimentary facies, grain size, and small-scale architectural elements and factors that may control the observed changes in stratigraphic architecture (e.g. Mutti and Normark, 1987; Posamentier et al., 1991; Pickering et al., 2001; Camacho et al., 2002; Brunt and McCaffrey, 2007; Schwarz and Arnott, 2007; Navarro et al., 2007; Kane et al., 2009; Pyles et al., 2010; McHargue et al., 2011; Di Celma et al., 2011; Figueiredo et al., 2013; Hubbard et al., 2014; Bain and Hubbard, 2016). Field methods for data collection, however, have remained the same for nearly the last two hundred years. Considering the rapid state of improvement and increased availability in digital technologies, there is a need to update the traditional techniques by integrating emerging digital field methods (e.g. McCaffrey et al., 2005; Wynn et al., 2005; Thurmond et al., 2006; Nieminski and Graham, 2017).

For this study, we consider a well exposed channel-lobe system from a key stratigraphic interval of the Upper Miocene Gorgoglione Flysch Formation (GFF), a coarse-grained siliciclastic turbidite succession that crops out in the Southern Apennines of Italy (Fig. 3.1). The studied section, informally named the Santa Maria section, is of primary importance in the interpretation of the stratigraphic evolution of the

whole GFF, since it represents one of the best-preserved isolated channels characterizing the upper portion of the turbidite succession (Casciano et al., 2017). This section was analyzed using standard field methods integrated with new digital field methods using a GigaPan imagery system and 3D photogrammetry. The goal of using these additional tools is to develop new methodologies for creating digital outcrop reconstructions that can supplement physical data for enhanced facies characterization of bed-scale architecture and facies distribution. The methods for creating GigaPan and 3D outcrop reconstructions, as well as their utility for research are described in this text. However, they are best seen in their digital format and can be found at a permanent online location at www.geode.net as part of a larger collection of digital geologic materials.

2. Geologic and depositional setting

The Southern Apennine Chain is a fold-and-thrust belt developed from late Oligocene to Pleistocene within the general framework of Africa-Europe major plate convergence on an eastward-retreating, W-dipping subduction zone (Doglioni, 1991; Patacca and Scandone, 2007 and references therein). The resulting north-eastward migration of the thrust front determined the progressive involvement in the thrust belt of several intervening Meso-Cenozoic basin and platform successions covering the Adria passive margin and adjacent Tethyan ocean. Accordingly, the structure of the Southern Apennine orogenic wedge is configured as a thick thrust pile of heavily deformed rootless nappes, tectonically overlying the subducted Apulian platform carbonates and associated foredeep deposits (Vezzani et al., 2010 and references therein). Thrust-top clastic successions of upper Eocene to Plio-Pleistocene age unconformably cover the whole thrust-pile (Patacca and Scandone, 2007). Among them, one of the better-preserved units is the late Burdigalian – early Tortonian GFF (Selli, 1962; Ciaranfi, 1972; Pescatore, 1978; Pescatore and Senatore, 1986; Patacca and Scandone, 1989; Pescatore, 1992). This ~1,950 m thick siliciclastic turbidite succession consists of coarse sandy turbidites and mudstones with subordinate conglomerates, filling a narrow and NNW-SSE oriented wedge-top basin (Boiano, 1997). Primary exposures of the GFF occur along the eastern edge of

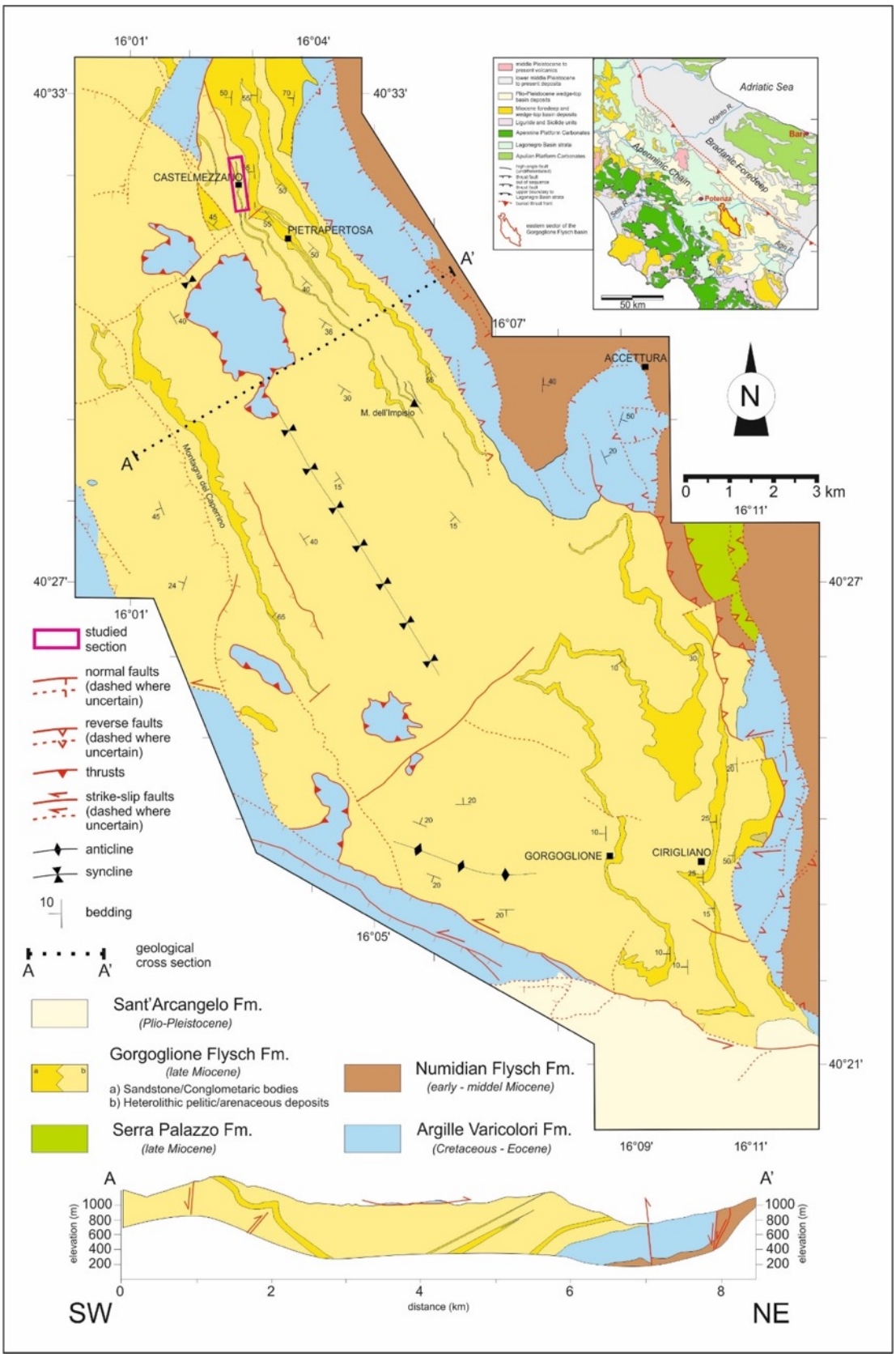

Figure 3.1. Map of the eastern sector of the Gorgoglione Flysch Formation in the Southern Apennines of Italy (from Giannandrea et al., 2016, modified).

the former basin, in a 25 km wide outcrop belt, between the towns of Castelmezzano and Gorgoglione, 25 km SE of Potenza (Fig. 3.1). In this area, the GFF unconformably overlies the Cretaceous - Eocene mud-rich succession of the Argille Varicolori Fm. (Fig. 3.1; Boiano, 1997). Deposition of the GFF was strictly controlled by the contractional tectonic deformations affecting the Apenninic accretionary wedge (Patacca et al., 1990; Boiano, 1997; Giannandrea et al., 2016). Provenance data shows that the GFF was sourced from a crystalline basement terrane located within the growing orogen to the West (Critelli and Loiacono, 1988). However, paleocurrent data document a prevalent paleoflow direction from NNW to SSE, along the longitudinal axis of the basin (Loiacono, 1974). Consequently, many authors invoked a paleogeographic scenario with sediment gravity flows initiated from an inferred shelf in the orogenic hinterland, which were directed down a NE-facing paleoslope and were successively deviated toward SSE along the basin axis near the base of slope (Boiano, 1997).

In the Castelmezzano – Pietrapertosa area, the lower ~ 1200 m of the succession are characterized by the occurrence of amalgamated sand bodies up to 25 m thick, systematically stacked to form extensive channel complex sets. A ~ 700 m thick clay-prone succession incised by isolated arenaceous-conglomeratic channels constitutes the topmost part of the basin-fill succession, where the studied section is located. The vertical architectural and grain-size evolution of channel types documented in the upper 1000 m of the turbidite succession (from amalgamated sand-filled channels to isolated conglomerate-rich channels), together with the gradual upward change in the background sedimentation (from sand-prone to clay-prone heterolithic deposits), likely reflects a shift along the depositional profile, passing from a near base-of-slope to a slope setting as a result of slope progradation (Casciano et al., 2017).

3. Methodology

The Santa Maria section was recorded and measured using both traditional sedimentary facies analysis data collection and emerging digital field techniques for outcrop mapping and data collection. Traditional methods included bed-scale characterization of sedimentological and stratigraphic elements and a paleoflow analysis. Stratigraphic data were collected in 8 measured sections logged at centimeter resolution, recording grain size distribution, bed thickness, internal bedding divisions, and bounding surfaces. Paleoflow data were recorded from 361 basal paleoflow indicators, such as flutes and grooves, and cross bed stratification. Additional digital data collection methods included the construction of ultra-high-resolution outcrop panoramas produced by the GigaPan® imagery system and 3D outcrop models obtained from aerial and ground-based imagery using structure-from-motion (SFM) 3D photogrammetry to aid in identification of key surfaces and the depositional architectures of stratigraphic units. The GigaPan image system is a tripod mounted robotic device, which functions with both point-and-shoot or

DSLR cameras, and guides the camera through precise photo grid with each photo at the maximum zoom level. The resulting photo set is stitched together using GigaPan Stitch® software to render a massive photomosaic image built from hundreds of individual photos (Fig. 3.2). The resulting images are viewed in the GigaPan® viewer or on their online site, www.gigapan.com, as "tiled" dynamic images in which the resolution increases at deeper levels of zoom. The GigaPan® device was used at four key locations for recording the section, two medium-range positions to record outcrop sections and two close-range positions to record detailed bed-scale features of two basal surfaces showing large numbers of scour structures (Fig. 3.2A). Our methods for creating 3D outcrop models involved large numbers of overlapping photos acquired from multiple positions and angles from the outcrop, taking advantage of all available ground-based viewpoints of the exposure. Photos were taken from unoriented positions and varying distances from the outcrop within approximately 50 m, maintaining photo overlap at values greater than 50%. An aerial-based photo set was acquired under the same general procedure from a helicopter above the study area. The photos were processed using Agisoft PhotoScan® software to produce 3D outcrop models (Fig. 3.3). Physical outcrop and GigaPan data sets were merged together by converting the large GigaPan images from their propriety GigaPan format into a static image format such as Photoshop RAW or TIFF at maximum resolution. The reformatted images were carefully annotated at full scale, transcribing the measured stratigraphic data directly on to the images recording centimeter scale features (Fig. 3.4). Correlations of stratigraphic intervals and surfaces were made directly onto the annotated GigaPan image supported by the use of the 3D outcrop models to verify interpretations.

4. Results

The studied interval of the Santa Maria section is approximately 40 m high and 280 m wide. In the following paragraphs, the results obtained from the analysis of physical and digital outcrop data are presented.

4.1. Sedimentary Facies and Facies Associations

At the smallest scale, sedimentary units are represented by beds, indicating a single sedimentation event. They are recognized as the products of gravity flow processes, based on bed-scale characteristics (cf., Bouma, 1962; Lowe, 1982, Talling et al. 2012). Six facies,

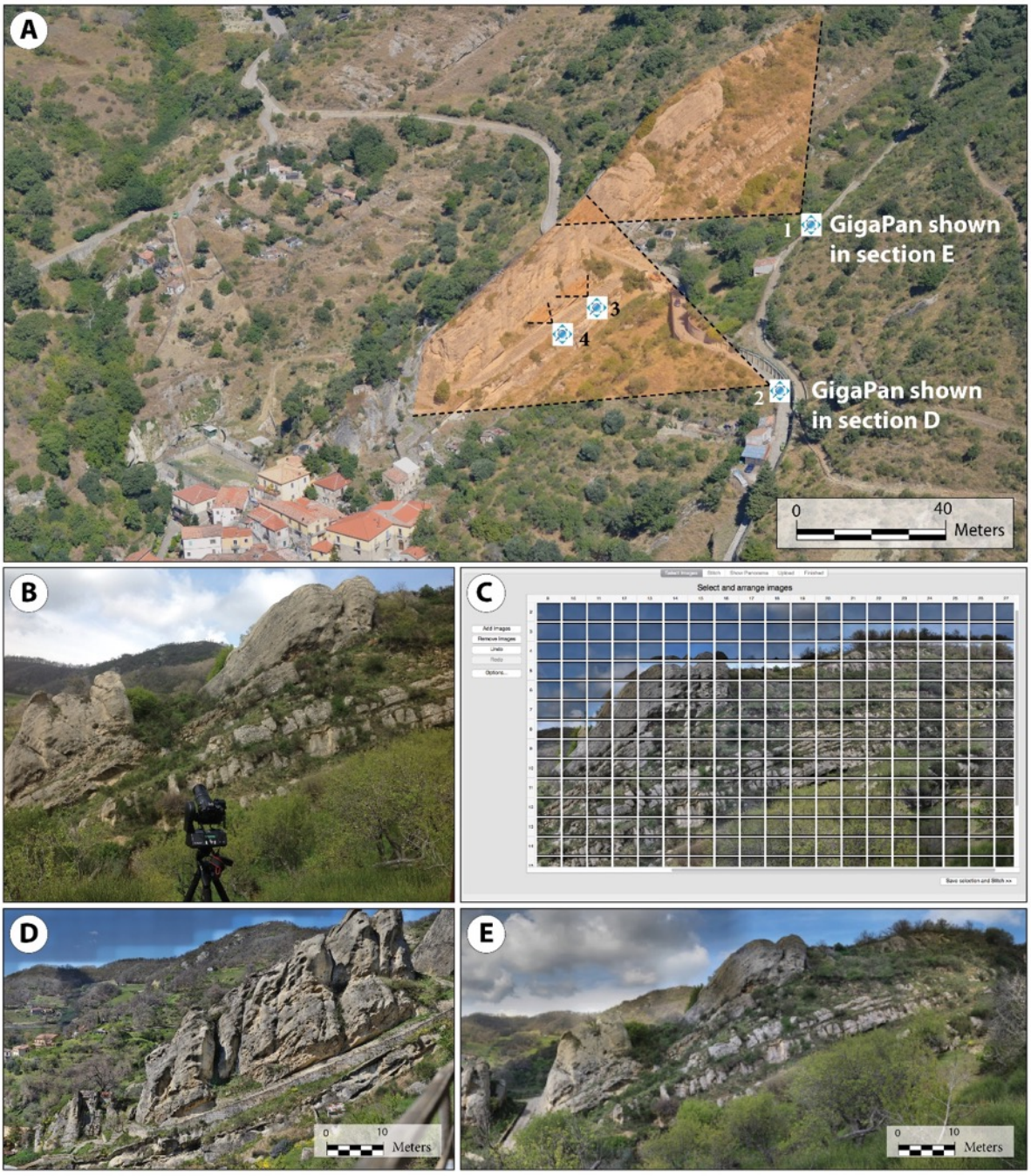

Figure 3.2. GigaPan® imagery methods. A) Location of 4 GigaPan® images used at medium range for the analysis of the stratigraphic section (1 and 2) and at close range for selected intervals (3 and 4). B) Tripod mounted GigaPan recording the outcrop. B) Photo stitching procedure using GigaPan® Stitch software. D and E) Resulting GigaPan® images of the Santa Maria Section.

grouped in two major sedimentary facies associations, have been distinguished in the Santa Maria section (Figs. 3.5, 3.6). Their detailed description, lateral and vertical distribution, and process-based interpretation are provided in Table 1.

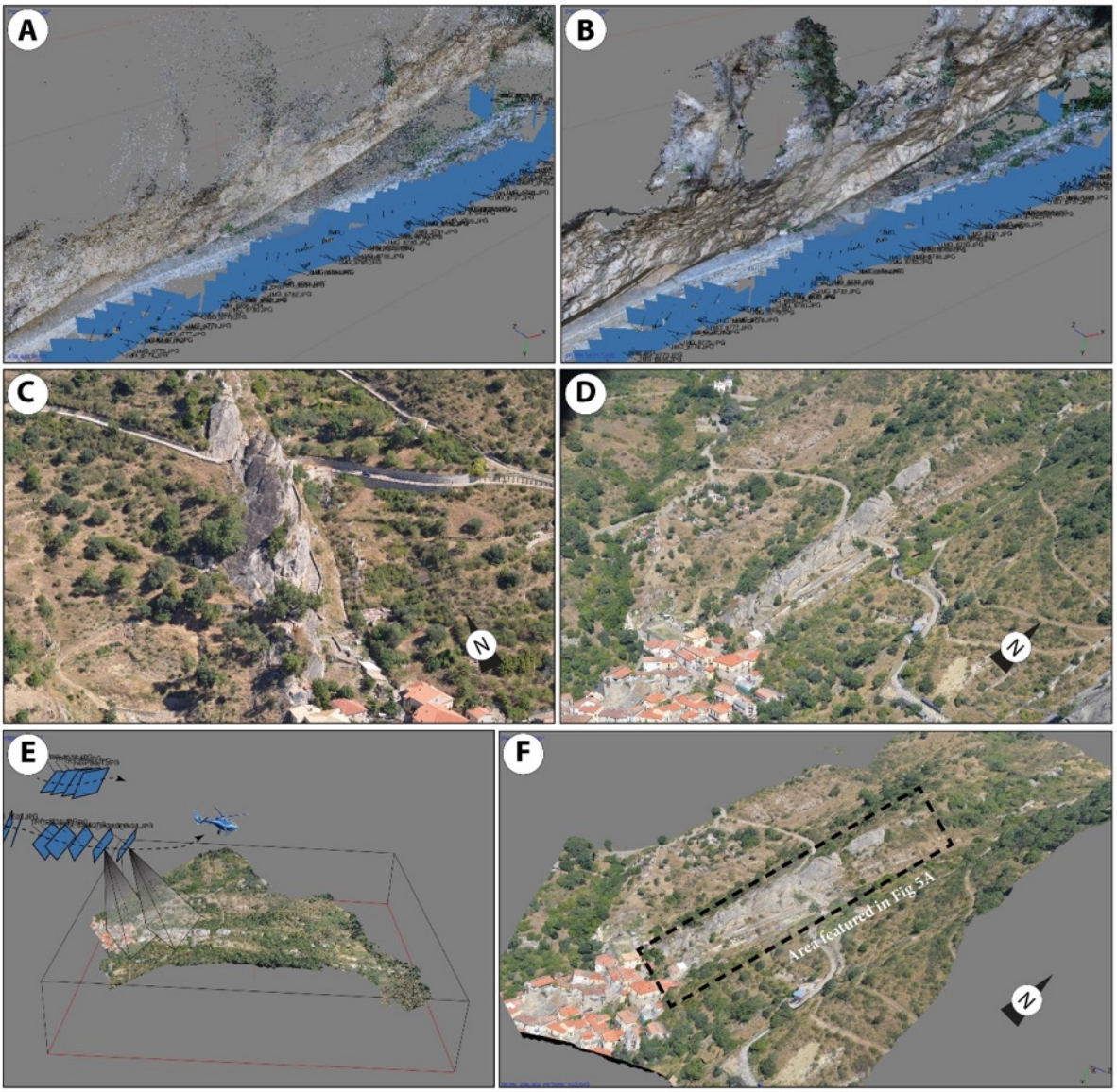

Figure 3.3. Photogrammetry procedures for the construction of photorealistic 3D models from ground based and aerial photo sets, using Agisoft PhotoScan®. A) Un-oriented ground-based photos collected at 1- 2 meters from the outcrop processed into a point cloud. B) Same photo set from A, processed as a solid object. C, D) Input aerial images for creation of aerial based 3D model. E) Aligned aerial photos and rendered dense point cloud showing the helicopter flight path and location of input photos. F) Fully rendered 3D model showing location of inset area in figure 3.5A.

4.1.1. Facies Association A

Description: Facies association A has been observed in the lower portion of the studied section (Figs. 3.5, 3.6). It is composed of three main facies: a medium to thick bedded sandstone (facies A1), heterolithic packages of interbedded mudstone and thin-bedded fine grained sandstones (facies A2), and isolated zones of highly convoluted and contorted sandstone beds (facies A3). Facies A1 (Fig. 3.7A, B) is found at the base of the section with beds stacked forming 1-3 m thick bed-sets with sharp upper and lower contacts. Paleocurrent indicators from sole structures exposed along basal A1 surfaces, such as flute casts and grooves, display a range of variability between SW and SE (Fig. 3.6). Observations from aerial panoramic photos reveal that

Figure 3.4. The high-resolution GigaPan® technique. A) Full outcrop GigaPan. B) Selected section of the image A seen under medium zoom. B) Selected section of image A under full zoom showing a 1.5-meter Jacob staff for scale.

A1 sandstone beds gradually thin toward NNE over several hundred meters, displaying an apparent lenticular geometry. Sandstone packages of facies A1 are punctuated by thin, laterally continuous packages of facies A2 (Fig. 3.7C), displaying a constant thickness throughout the entire exposure. Facies A3 is found as isolated wedge-shaped intervals of intrastratal deformation (Fig. 3.7D), which are laterally equivalent to facies A2. Several ductile and brittle deformation features are observed, including

chaotic and disintegrated strata containing folds, de-watering structures and minor displacements of dismembered bedding along basal thrust planes. Deformation zones are bound below and above by stratified sand beds of facies A1, with underlying beds showing

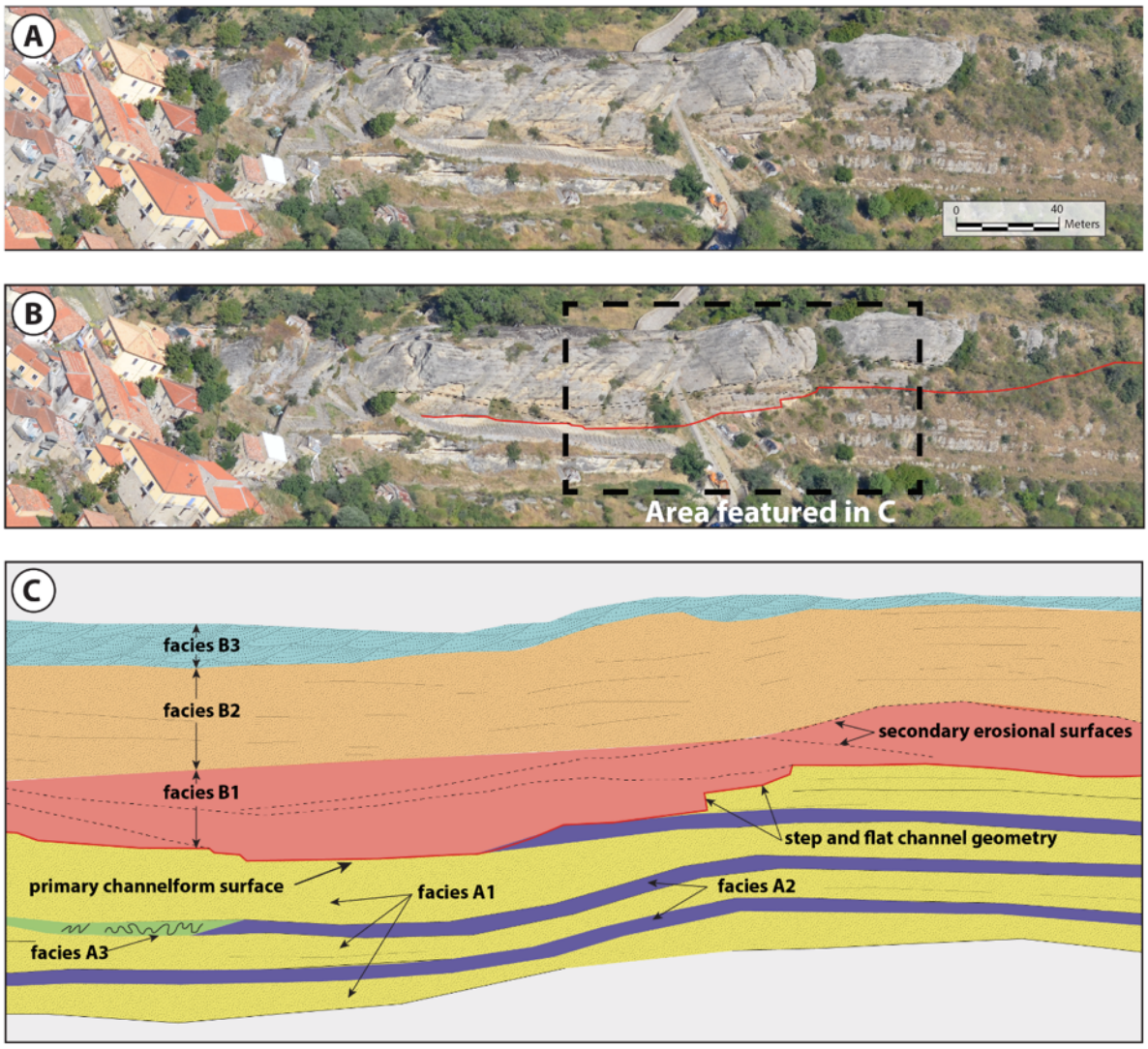

Figure 3.5. The Santa Maria section. A) Aerial image of section exposed along a staircase above the town of Castelmezzano rotated approximately 45 degrees to correct bedding to horizontal. B) Annotated outcrop section. C) Close-up illustration of the section, showing facies distribution.

gently sheared bedforms. Upper bounding surfaces of deformation zones are found as sharp contacts with overlying beds of undisturbed bedding.

Interpretation: Based on sedimentary structures, bedding geometry and paleoflow dispersion, sand rich packages of facies A1 are interpreted as individual lobes stacked vertically to form a lobe complex (Prélat et al., 2009). The wide range of paleoflow dispersion documented from sole structures indicates deposition in a loosely confined environment. These lobes are intercalated with the heterolithic packages of facies A2, interpreted as interlobe deposits regarded as part of distal lobe fringes (Prélat and Hodgson, 2013). Intrastratal deformation zones described in facies A3 and found in this section as well as several other nearby sections within the GFF, are interpreted as slump intervals. These slumps are possibly triggered in association with margin failures of the contemporaneous feeder channel, located up dip of the depositional lobes. Locally, thrust bound sandstone beds with mildly deformed laminae beneath occurring within the slump zones, show evidence of composite deformation across the lower boundary of the slump interval (Butler and McCaffrey, 2010). These deformed deposits are restricted to the heterolithic facies A2 and triggered along basal detachment planes in mud-rich mechanically "weak" layers. The presence of these deformational features limited to specific lithofacies indicates the direct influence of depositional architecture on the location and size of slope failure and intrastratal deformation (Auchter et al., 2016).

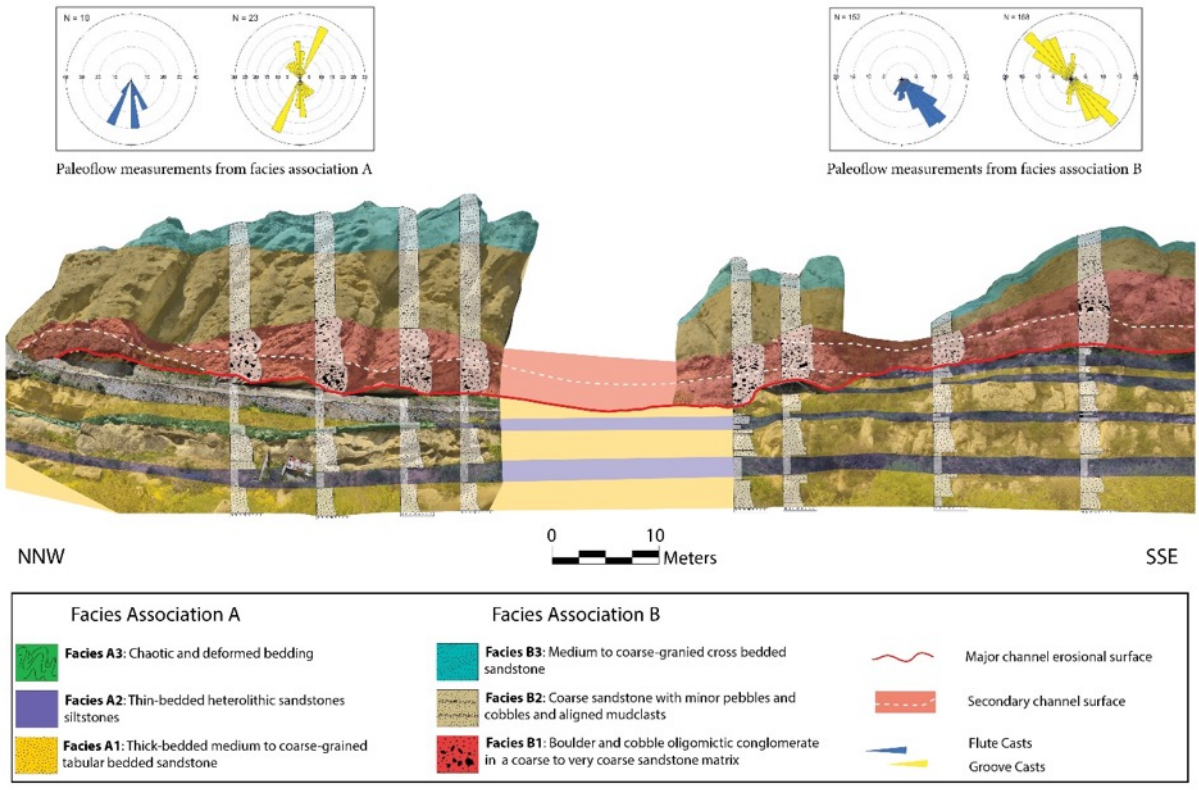

Figure 3.6. Annotated composite GigaPan image showing measured stratigraphic sections, facies, and paleoflow data

4.1.2. Facies Association B

Description: Facies association B (Fig. 3.8) has been documented in the upper portion of the Santa Maria section, directly overlying the deposits of facies association A. Facies association B reaches a maximum thickness of 17.5 m and is composed of three primary facies: a basal chaotic

Table 1
Lithofacies and Facies Associations

*Interpretations and architectural elements after Bouma 1962, Lowe 1982

Lithofacies	Lithology	Grain size and sorting	Basal Surfaces	Sedimentary structures	Thickness	Paleoflow	Interpretations*	Patterns of occurence
Facies Association A								
Thick Bedded Sandstone (A1)	Sandstone	Medium to coarse grained	Sharp basal contact	Massive, normal grading and plane parallel laminations. Locally crossebedded.	20- 50 cm	SW-SE	Ta -Tb Bouma intervals deposited by high density turbidity currents in depositional lobes.	Occurs as alternating packages of Facies A1 and Facies A2 which are overlain and truncated by an upper irregular erosional surface. Facies A3 can be found within A1 beds passing laterally from chaotic beds gradually transitioning into regularlly bedded A1 inctervals.
Mud Rich Heterolithic (A2)	Dark grey mudstone and siltstone	Mudstone and fine grained sands	Gradational	Massive and minor plane parallel laminations.	0.5 - 1 m	NA	Deposited on lobe fringe environments, passes laterally into thicker and coarser deposits.	
Chaotic Bedded Heterolithic (A3)	Sandstone and mudstone	Medium to coarse grained sandstone	Sharp base marked by detachment surface	Convuluted and chaotic bedding with folds, minor thrusts and dewatering structures.	~1 m	NA	Mass wasting resulting in detachment and dislocation of slumps towards a downdip location causing internal deformation of strata in both britle and ductile senses.	
Facies Association B								
Coarse Grained Conglomerate (B1)	Oligomictic conglomerate and sandstone	Very coarse, poorly sorted conglomerate in coarse sand matrix	Sharp and irregular erosional with underlying strata	Normal vertical grading with loading structures	3-5 m	S/SE	Lowe Division R3. Channel lag sediments deposited during periods of sediment bypass.	Occurs as a 20 - 30 meter package marked by a sharply erosional lower bounding surface with a terraced geometry stepping upwards from a proximal portion which truncates underlying stratigraphy. Lower units found as Facies B1 passing gradationally upwards into Facies B2 marked by the loss of large agnular clasts and transition into massive sands with mud rip up clasts. Facies B2 passes upwards gradationally into overlying Facies B3 marked by the loss of mud rip up clasts and transition into strongly dune cross-bedded sands.
Amalgamated Sandstone (B2)	Sandstone	Medium to coarse grained sand	Sharp surface indicated by aligned mud rip-up clasts	Massive with subtle normal grading and aligned mud rip up clasts	~1 m	NA	Deposition from rapidly collapsing high density turbidity currents during filling phase of channel evolution.	
Crossbedded Sandstone (B3)	Sandstone	Medium to coarse grained sand with sparse pebbles	Gradational with underlying strata	Dune-scale cross bedding	1-3 m	SW	Sediment reworking by overpassing turbidity currents.	

Table 1. Facies and Facies Associations

polymictic conglomerate in a coarse-grained sandstone matrix (facies B1), passing gradually upwards into massive amalgamated sandstones (facies B2), and large-scale cross-laminated sandstones in the upper-most portion (facies B3). The first two facies are laterally confined within

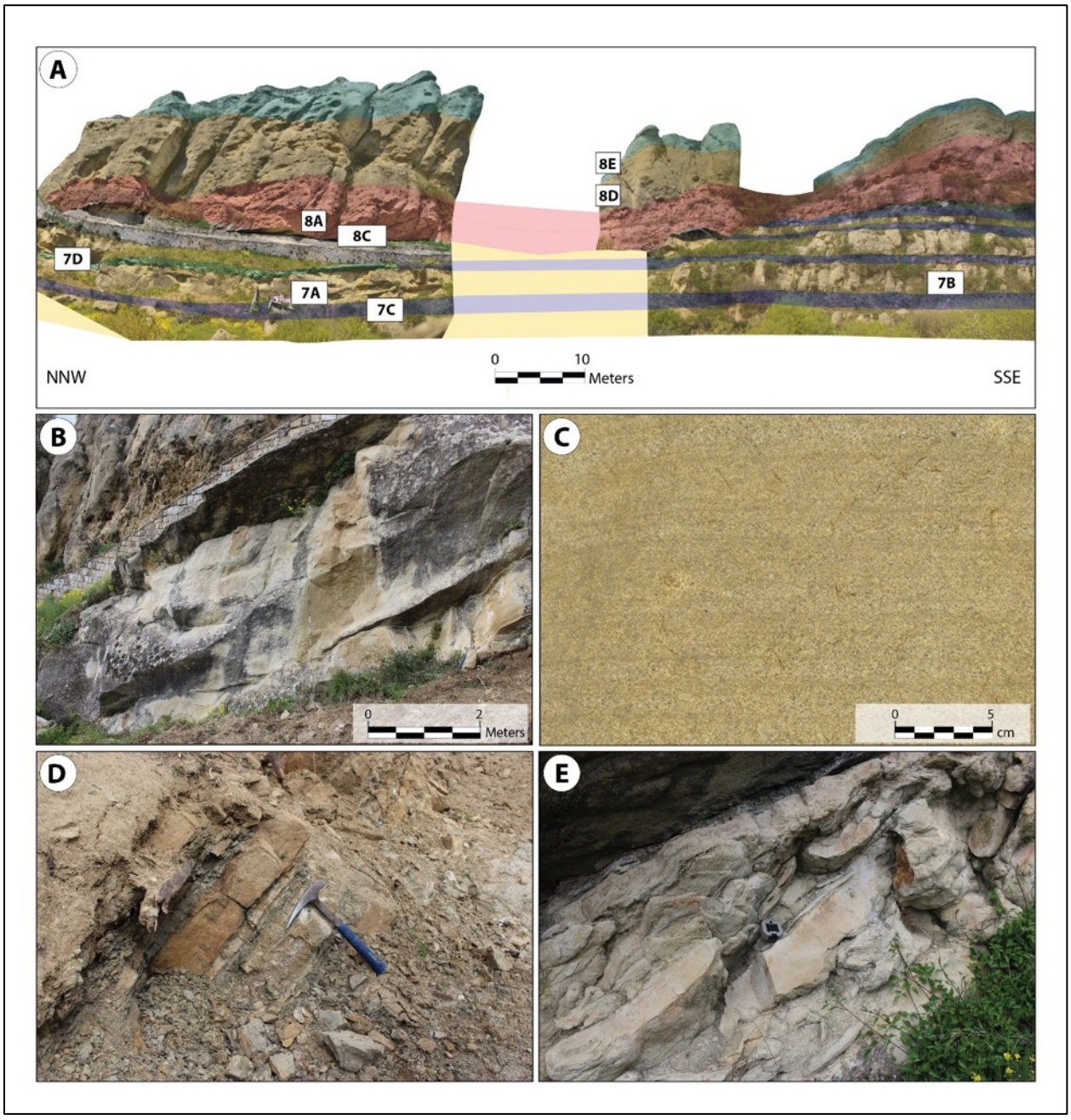

Figure 3.7. Outcrop photographs of Facies Association A. A) Thick bedded sandstones of facies A1. B) Close-up view of the plane parallel laminated sandstone beds of facies A1. C) Heterolithic packages of interbedded fine-grained sandstones and mudstones (facies A2); 0.3-m-long hammer for scale. D) Contorted sandstone bed of facies A3, showing dewatering structures and minor brittle faulting (7.8 x 7.1 cm compass for scale).

an irregularly-shaped, concave-upward erosional surface deeply incised into the underlying deposits of facies association A. This surface can be traced for approximately 1.2 km along the outcrop (Fig. 3.5B). It has a pronounced meter-scale “step and flat” geometry (Figs. 3.5C, 3.6) with the “flat” segments in most cases eroding along parallel surfaces to the underlying bedding and the “step” portions rising abruptly vertically across sandstone beds before arching back along the bedding, forming the next step. Step-up surfaces are found to stratigraphically correspond with

vertical grain-size jumps and secondary erosional surfaces in the coarse-grained conglomerate of facies B1. Basal conglomerates of facies B1 rest directly above the erosional surface and show subtle normal grading with several fining-upward sequences and minor erosional surfaces. The coarsest B1 material is found within the deepest and central portion of the erosional surface and

is composed of large rounded and angular extra-basinal clasts up to 80 cm mixed with rip-up mud clasts (Fig. 3.8A). The abundance of extra-basinal clasts decreases with lateral distance from the central part of the section gradually being replaced by mud rip-up clasts before eventually disappearing altogether (Fig. 3.8B). Paleocurrent indicators from sole marks measured along the base of facies B1 (Fig. 3.8C), show a NW-SE trend with a limited range of dispersion. Amalgamated sandstones of facies B2 (Fig. 3.8D) show normal grading, with bedding indicated by horizons of irregularly-shaped mud clasts that amalgamate and bifurcate over short distances. In the thicker central portion of the section, amalgamated sandstones (facies B2) directly overlie basal conglomerates (of facies B1), whereas in lateral positions they are found draping the erosional surface. Cross-laminated sandstones of facies B3 (Fig. 3.8E) show an abrupt transition from underlying amalgamated sands with thickness varying from 1 to 3 m. Facies B3 occurs as a “capstone” interval, which is distributed across the entire exposure and present in all measured sections. The cross stratification displays a highly variable pattern of paleocurrent directions, diverging up to 75° towards SW from the paleoflow documented from the sole structures.

Interpretation: Based on vertical and lateral facies stacking arrangements, facies association B is interpreted as the infill of a single channel-form. The stepped-terrace geometry and multiple internal erosion surfaces have been recognized by other authors in similar slope channel systems (e.g. Eschard et al., 2003; Navarro et al., 2007; Hubbard et al., 2014) and indicate the composite nature of the basal surface. The basal conglomeratic interval (facies B1) is associated with erosional phases and substantial sediment bypass. The relative abundance of extra-formational

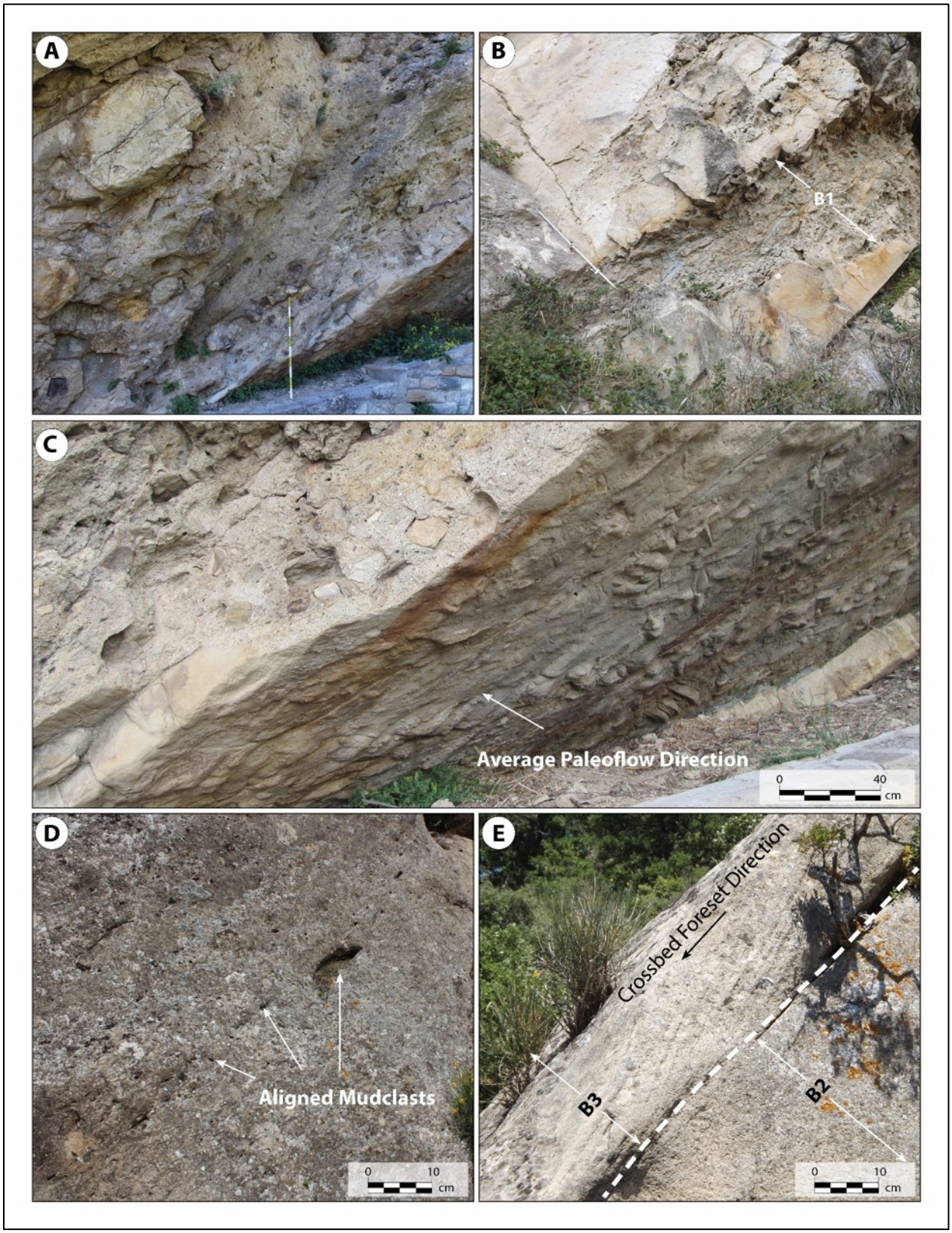

Figure 3.8. Outcrop photographs of Facies Association B. A) Mixed extra basinal and mud-clast rich conglomeratic deposits of facies B1, characterizing the channel axis (1 m logging staff for scale). B) Mud clast rich conglomerates of facies B1 in the channel off-axis (2 m Jacob's staff for scale). C) Exposed basal erosional surface, showing flute casts, grooves and average paleoflow direction. D) Massive structureless sandstones of facies B2, with thin mud clasts horizons marking amalgamation surfaces. E) Cross-laminated sandstones of facies B3, overlying amalgamated sandstones of facies B2.

conglomeratic clasts in the deepest and central portion of the erosional surface indicates the channel axis, where flow velocity was highest (McHargue et al., 2011; Stevenson et al., 2015). Conversely, their absence in lateral portions of the section, with a concurrent increase of mud-rich conglomerates, indicates channel off-axis (Fig. 3.9A). Because the gravelly facies B1 may represent only a small fraction of the total sediment load in large, turbulent sediment gravity flows, the preservation of thick, amalgamated gravelly packages implies that much greater amounts of sand and mud have completely bypassed the study area during its deposition. As such, this type of basal coarse-grained material has been recognized as a typical bypass facies (e.g. Alpak et al, 2013; Di Celma et al., 2013; Stevenson et al., 2015) draping the basal erosion surface. Amalgamated sandstones of facies B2 are interpreted as the product of rapid suspension deposition by sand-rich turbidity currents during the backfilling phase of the channel-form. The large-scale cross-laminated sandstones of facies B3 are interpreted as indicating the loss of channel confinement. Divergent paleoflow between basal sole structures (~ 140°) and upper cross stratification (up to ~ 220°) is consistent with lateral flow expansion as channel confinement progressively decreases. Similar facies patterns have been described by Schwarz and Arnott (2007) in the Isaac Formation of the Windermere Supergroup of Canada in channel fills capped by dune-cross-stratified sandstones. The occurrence of amalgamated coarse-grained sandstones capped by cross-laminated sandstones has been recognized in many other channel-fill deposits of the GFF, constituting a recurring motif in the process of channel infilling at the basin scale.

4.2 Channel Dimensions and Hierarchy

The Santa Maria exposure is oriented in a N-S direction, highly oblique to the primary channel paleoflow direction inferred from the measurements of the basal structures. For this reason, the aspect ratio (width: thickness) of the Santa Maria channel has been calculated for a reconstructed strike-oriented cross sections by projecting the apparent dimensions onto a surface normal to the average paleocurrent direction. Using this method, the actual width of the channel is calculated at about 180 m. Comparable dimensions for channel-fill deposits are reported in literature for other deep-water systems (e.g. McHargue et al., 2011; McHauley and Hubbard, 2013; Figueiredo et al., 2013; Stright, et al. 2014). By using the scheme proposed by Pemberton et al. (2016) the dimensions of the Santa Maria channel (180 m wide and 17.5 m thick) are consistent with a low-aspect-ratio channel. According to the hierarchical scheme of Campion et al. (2005), this channel is defined as a single channel element.

5. Discussion

5.1. Evolution of Santa Maria channel-lobe depositional system

The deposits exposed along the Santa Maria section record the complete lifespan of a channel-lobe system, with deposition passing from frontal lobe growth, through channel incision, to confined backfilling and eventual spillover (Figs. 3.9A, 3.9B). The analyzed channel-lobe system, with the channel erosionally overlying frontal lobes, displays a characteristic stacking pattern that has been recently documented in ancient and modern settings (Morris et al., 2014; Hodgson et al., 2016).

5.1.1 Deposition of frontal lobes

The sand-rich tabular strata underlying the Santa Maria channel indicate the deposition of frontal lobes (Fig. 3.9B) in unconfined settings down-dip of the feeder channel, by numerous individual high-energy sediment gravity flows (Prélat et al., 2009). The laterally-continuous heterolithic interlobes and the wide range of paleoflow dispersion show that depositional lobe emplacement was migrating positions as lobes avulsed seeking accommodation space (Prelat and Hodgson, 2013).

5.1.2 Initiation of channel form and erosional surface

The incisional relationship between channel and lobe deposits indicates that the Santa Maria channel initiated with excavation of the seafloor by highly-energetic sedimentary gravity flows as the channel advanced over the lobe (Fig. 3.9B; Fildani et al., 2013). This process is recognized as result of slope channel lengthening occurring in tandem with the simultaneous deposition of new frontal lobes down dip (Morris et al., 2014). During this period, the channel functioned as conduit for sediment transfer with a majority of sediment flowing to a down dip depocenter (Hubbard et al., 2014). This phase of the channel initiation has been recognized as a period of maximum bypass-lag deposition (Eschard et al, 2003; McHargue et al., 2011; Stevenson et al., 2015). The protracted passage of high-energy turbidity flows caused the repeated erosion of the substrate that sculpted the irregular basal channel-form, characterized by a “step-and-flat” geometry, mantled by coarse-grained lag material. Stratigraphic correlations between “flat” segments in the channel base geometry and significant grain size jumps and secondary erosional surfaces with in the lag deposits confirm these multiple incisional phases, with gravity flows eroding and reworking the lag deposits during each successive event.

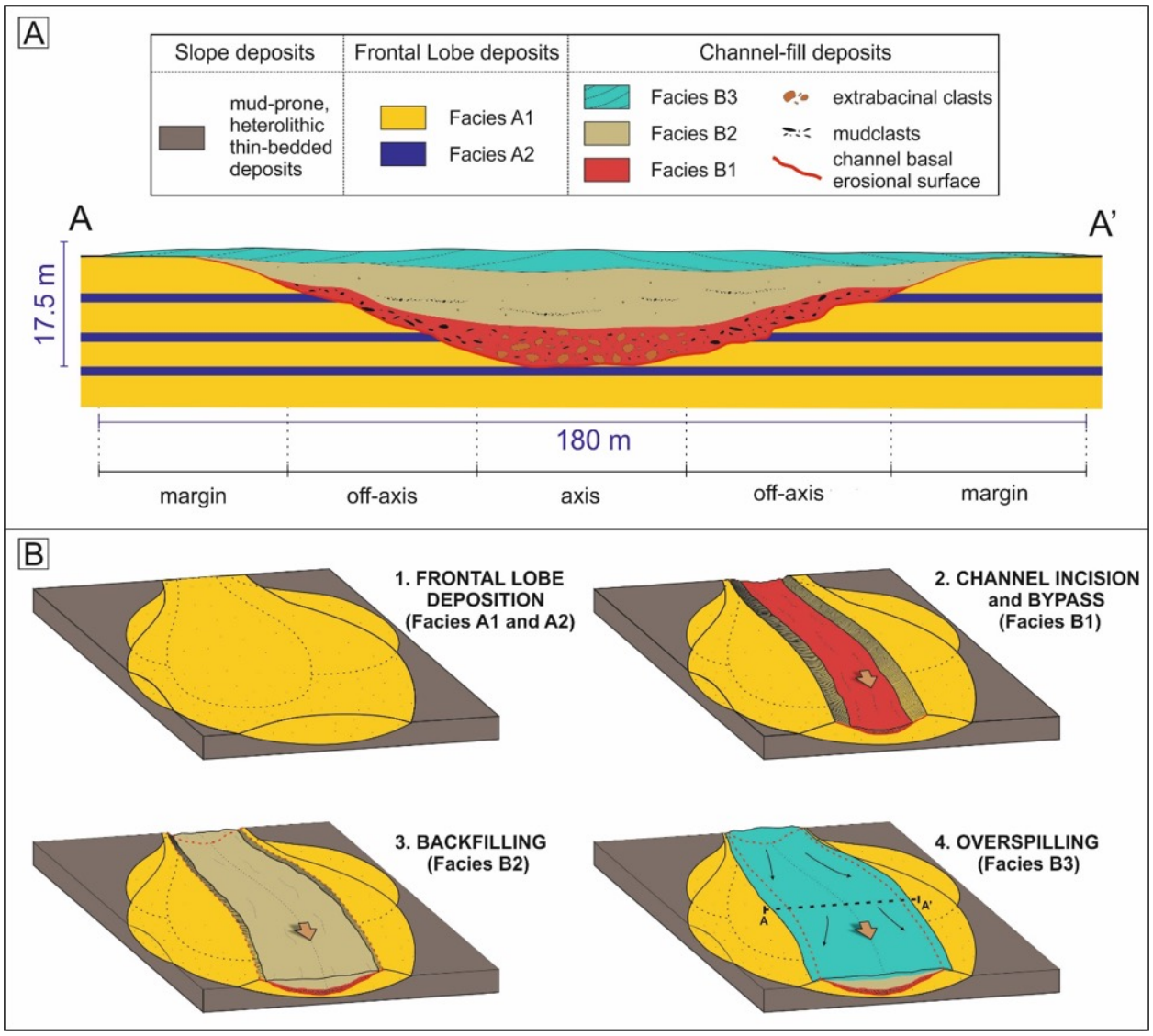

Figure 3.9. A) Schematic cross-section of the Santa Maria Channel, showing the different portions of the channel (axis / off-axis / margin) and related facies distribution. Abundant mixed extra formational conglomerates and intrabasinal mud clasts characterize the channel axis (see Fig. 8A). The amount of extra formational elements considerably decreases in the channel off-axis, where facies B1 is almost entirely constituted of mud clasts (see Fig. 3.8B). The channel margin is marked by the absence of lag deposits, with predominant cross-laminated sandstones (facies B3) and amalgamated structureless sandstones (facies B2), directly overlying the basal erosional surface. B) Block diagrams describing the evolutionary model for the Santa Maria channel-lobe system (see text for a detailed discussion). The background sedimentation is represented by mud-prone heterolithic thin bedded deposits that characterize the upper part of the Gorgoglione Flysch succession.

5.1.3 Backfilling of the Santa Maria Channel

After the complex incisional phase that sculpted the irregular channel form, the Santa Maria channel was almost completely filled by sandy sediments, during a period referred to as backfilling (Gardner and Borer, 2000; Fig. 3.9). This phase is indicated by the presence of the massive amalgamated sandstones of facies B2. These sandstones suggest deposition in a confined channel under waning flow conditions favoring rapid fallout of sediment with minor incision into the substrate. The frequency of aligned mud clast intervals marking multiple amalgamation surfaces, suggests that the filling of the channel was achieved through many successive events.

5.1.4 Loss of confinement

The presence of laterally-persistent cross-laminated sandstone of facies B3 capping the channel-fill sequence suggests a transition from confined to poorly-confined conditions as the channel became filled with partially-over spilling turbidity currents (Fig. 3.9B).

6. Conclusions

Integration of digital outcrop data with traditional stratigraphic field techniques, has significantly improved the reconstruction of the Santa Maria section, increasing the spatial resolution of the geological data and allowing the investigation of inaccessible portions of the outcrops. The use of single GigaPan images allows inspection of the exposure at variable scale, from centimeter scale bedforms up to outcrop-scale stratigraphic architectures. Through the use of 3D outcrop models, the interpretation of the depositional architectures and bedding geometries has been carried out with greater certainty. This study shows how facies characterization and high-resolution stratigraphic correlation can greatly benefit by the use of these emerging digital data collection techniques. The detailed characterization of sedimentary facies distribution and the enhanced analysis of architectural elements at the Santa Maria section allowed the interpretation of the stratigraphic evolution of a submarine channel-lobe system. Facies associations and the discrepancy between paleoflow dispersion patterns indicate two primary depositional settings and a range of flow types, from confined flows occurring in the slope channel to unconfined flows producing frontal lobes downdip of the feeder channel. Multiple phases of the Santa Maria channel evolution have been documented, from channel incision and sediment bypass, to protracted backfilling from high-density turbidity flows recording a progressive loss of confinement. The combined methodology proposed in this paper provides solutions to the challenges involved with outcrop characterization by creating observation points from perspectives and distances that are not physically possible in the field. Furthermore, these digital outcrop reconstructions allow researchers to return from the field with a precise and detailed record of the study area, which can be used to support the verification of additional interpretations during the analysis of data. While this case-study focuses on the applications of this approach as a tool for enhanced sedimentary facies analysis, the methodologies

discussed here can be useful in a broad range of geoscience research applications (e.g., for the creation of high-resolution DTM's), particularly where the sole use of traditional field data collection tools is not sufficient to provide a complete perspective of the broad geological context.

Acknowledgements

This work was funded by University of Camerino and Turbidites Research Group industry sponsors: Anadarko, BG-Group, BP, Conoco Phillips, Dana Petroleum, Eni, Nexen, OMV, Petronas, Shell, Statoil and Woodside. We also acknowledge the support of the GEODE group (Google Earth for Onsite and Distance Education) for assistance with the GigaPan and 3D photogrammetry equipment and procedures. The authors thank the reviewers for helping to strengthen this manuscript.

References

Alpak, F.O., Barton, M.D., Naruk, S.J., 2013. The impact of fine-scale turbidite channel architecture on deep-water reservoir performance. AAPG Bulletin, 97, 251–284.

Auchter, N.C., Romans, B.W., Hubbard, S.M. 2016. Influence of deposit architecture on intrastratal deformation, slope deposits of the Tres Pasos Formation, Chile. Sedimentary Geology, 341, 13-26.

Bain, H.A., Hubbard, S.M., 2016. Stratigraphic evolution of a long-lived submarine channel system in the Late Cretaceous Nanaimo Group, British Columbia, Canada. Sedimentary Geology, 337, 113-132.

Boiano, U., 1997, Anatomy of a siliciclastic turbidite basin: The Gorgoglione Flysch, Upper Miocene, southern Italy: physical stratigraphy, sedimentology and sequence-stratigraphic framework. Sedimentary Geology, v. 107, p. 231–262.

Bouma, A.H., 1962. Sedimentology of Some Flysch Deposits; A Graphic Approach to Facies Interpretation. Elsevier, Amsterdam, 168 pp.

Brunt, R.L., McCaffrey, W.D., 2007. Heterogeneity of fill within an incised channel: The Oligocene Gres du Champsaur, SE France. Marine and Petroleum Geology, 24, 529-539.

Butler, R.W.H., McCaffrey, W.D. 2010. Structural evolution and sediment entrainment in mass-transport complexes: outcrop studies from Italy. Journal of the Geological Society, 167, 617-631.

Camacho, H., Busby, C.J., Kneller, B., 2002. A new depositional model for the classical turbidite locality at San Clemente State Beach, California. AAPG Bulletin, 86, 1543–1560

Casciano, C.I., Di Celma, C., Patacci, M., Longhitano, S.G., McCaffrey, W.D., 2017. Hierarchy and facies distribution in turbiditic sandstone channel-fills: the Gorgoglione Flysch Formation (Miocene of Basilicata, Southern Italy). In: Deep-water Depositional Systems: Advances and Applications Conference, 25-27 January, The Geological Society, London, UK.

Ciaranfi, N., 1972. Il Flysch di Gorgoglione. Boll. Serv. Geol. d'It., 92, 101-114.

Critelli, S., & Loiacono, F. (1988). Provenienza e dispersione dei sedimenti nel flysch di Gorgoglione (Langhiano–Tortoniano, Appennino Lucano): Implicazioni sull'evoluzione delle mode detritiche arenacee nell'orogene sudappenninico. Memorie della Società Geologica Italiana, 41, 809-826.

Deptuck, M.E., Sylvester, Z., Pirmez, C., O'Byrne, C., 2007. Migration–aggradation history and 3-D seismic geomorphology of submarine channels in the Pleistocene Benin-major Canyon, western Niger Delta slope: Marine and Petroleum Geology, 24, 406–433.

Di Celma, C., Brunt, R.L., Hodgson, D.M., Flint, S.S. Kavanagh, J.P., 2011. Spatial and temporal evolution of a Permian submarine slope channel-levee system, Karoo Basin, South Africa. Journal of Sedimentary Research, 81, 579-599.

Di Celma, C., Cantalamessa, G., Didaskalou, P., 2013. Stratigraphic organization and predictability of mixed coarse-grained and fine-grained successions in an upper slope Pleistocene turbidite system of the Peri-Adriatic basin. Sedimentology, 60, 763–799.

Doglioni, C., 1991. A proposal for the kinematic modelling of W-dipping subductions-possible applications to the Tyrrhenian-Apennines system. Terra Nova, 3, 423-434.

Eschard, R., Albouy, E., Deschamps, R., Euzen, T., Ayub, A. (2003). Downstream evolution of turbiditic channel complexes in the Pab Range outcrops (Maastrichtian, Pakistan). Marine and Petroleum Geology, 20, 691-710.

Figueiredo, J.J.P., Hodgson, D.M., Flint, S.S., Kavanagh, J.P., 2013. Architecture of a channel complex formed and filled during long-term degradation and entrenchment on the upper submarine slope, Unit F, Fort Brown Fm., SW Karoo Basin, South Africa: Marine and Petroleum Geology, 41, 104–116.

Fildani, A., Hubbard, S.M., Covault, J.A., Maier, K.L., Romans, B.W., Traer, M., Rowland, J.C., 2013. Erosion at inception of deep-sea channels: Marine and Petroleum Geology, 41, 48–61.

Gardner, M.H., Borer, J.M., 2000. Submarine channel architecture along a slope to basin profile, Brushy Canyon Formation, West Texas. In: Bouma, A.H., Stone, C.G. (Eds.), Fine-Grained Turbidite

Systems. Memoir 72-American Association of Petroleum Geologists and Special Publication 68-SEPM, pp. 195e214.
Giannandrea, P., Loiacono, F., Maiorano, P., Lirer, F., Puglisi, D., 2016. Geological map of the eastern sector of the Gorgoglione Basin (southern Italy). Italian Journal of Geosciences, 135, 120-141.
Hubbard, S.M., Covault, J.A., Fildani, A., Romans, B.W., 2014. Sediment transfer and deposition in slope channels: Deciphering the record of enigmatic deep-sea processes from outcrop: Geological Society of America Bulletin, 126, 857–871.
Hodgson, D.M., Kane, I.A., Flint, S.S., Brunt, R.L., and Ortiz-Karpf, A., 2016, Time-Transgressive Confinement On the Slope and the Progradation of Basin-Floor Fans: Implications For the Sequence Stratigraphy of Deep-Water Deposits: Journal of Sedimentary Research, v. 86, p. 73–86, doi: 10.2110/jsr.2016.3.
Kane, I.A., Dykstra, M.L., Kneller, B.C., Tremblay, S., McCaffrey, W.D., 2009. Architecture of a coarse-grained channel levée system: the Rosario Formation, Baja California, Mexico. Sedimentology, 56, 2207-2234.
Loiacono, F., 1974. Osservazioni sulla direzione delle paleocorrenti nel Flysch di Gorgoglione (Lucania). Bollettino della Società Geologica Italiana, 93, 1127-1155.
Lowe, D.R., 1982. Sediment gravity flows: depositional models with special reference to the deposits of high-density turbidity currents. Journal of Sedimentary Petrology, 52, 279–297.
Macauley, R.V., Hubbard, S.M., 2013. Slope channel sedimentary processes and stratigraphic stacking, Cretaceous Tres Pasos Formation slope system, Chilean Patagonia. Marine and Petroleum Geology, v. 41, p. 146–162.
Mayall, M., Jones, E., Casey, M., 2006. Turbidite channel reservoirs—Key elements in facies prediction and effective development: Marine and Petroleum Geology, 23, 821–841.
Mayall, M., Stewart, I., 2000. The architecture of turbidite slope channels. In Deep-Water Reservoirs of the World: SEPM, Gulf Coast Section, 20th Annual Research Conference (Vol. 578, p. 586).
McCaffrey, K.J.W., Jones, R.R., Holdsworth, R.E., Wilson, R.W., Clegg, P., Imber, J., Holliman, N., Trinks, I., 2005. Unlocking the spatial dimension: digital technologies and the future of geoscience fieldwork: Journal of the Geological Society, 162, 927–938.
McHargue, T., Pyrcz, M.J., Sullivan, M.D., Clark, J., Fildani, A., Romans, B., Covault, J., Levy, M., Posamentier, H., Drinkwater, N., 2011. Architecture of turbidite channel systems on the continental slope: Patterns and predictions: Marine and Petroleum Geology, 28, 728-743.
Morris, E.A., Hodgson, D.M., Flint, S.S., Brunt, R.L., Butterworth, P.J., Verhaeghe, J., 2014. Sedimentology, stratigraphic architecture, and depositional context of submarine frontal-lobe complexes. Journal of Sedimentary Research, 84, 763–780.
Mutti, E., Normark, W.R., 1987. Comparing Examples of Modern and Ancient Turbidite Systems: Problems and Concepts. In Leggett, J.K., and Zuffa, G.G., eds., Marine Clastic Sedimentology: Springer, The Netherlands, p. 1–38.
Navarro, L., Khan, Z., Arnott, R. W. C., 2007. Depositional architecture and evolution of a deep-marine channel-levee complex: Isaac Formation (Windermere Supergroup), Southern Canadian Cordillera. In: T. H. Nilsen, R. D. Shew, G. S. Steffens, and J. R. J. Studlick, eds., Atlas of deep-water outcrops: AAPG Studies in Geology 56, CD-ROM, 22 p.
Nieminski, N.M., and GRAHAM, S.A., 2017, Modeling Stratigraphic Architecture Using Small Unmanned Aerial Vehicles and Photogrammetry: Examples From the Miocene East Coast Basin, New Zealand: Journal of Sedimentary Research, v. 87, p. 126–132, doi: 10.2110/jsr.2017.5.
Patacca, E., Scandone, P., 1989. Post-Tortonian mountain building in the Apennines. The role of the passive sinking of a relic lithospheric slab. In: Boriani, A., Bonafede, M., Piccardo, G.B., Vai, G.B. (Eds.), The Lithosphere in Italy: Atti Convegno Lincei, 80, pp. 157–176.
Patacca, E., Sartori, R., Scandone, P., 1990. Tyrrhenian basin and apenninic arcs: kinematic relations since late Tortonian times. Memorie della Societ`a Geologica Italiana 45, 425–451.
Patacca, E.,Scandone, P., 2007. Geology of the Southern Apennines. Bollettino della Società Geologica Italiana, 7, 75–119.

Pemberton, E.A.L., Hubbard, S.M., Fildani, A., Romans, B., Stright, L., 2016. The stratigraphic expression of decreasing confinement along a deep-water sediment routing system: Outcrop example from southern Chile: Geosphere, 12, 114–134.

Pescatore, T.S., 1978. Evoluzione tettonica del Bacino Irpino (Italia Meridionale) durante il Miocene. Boll. Soc. Geol. Ital., 97, 783–805.

Pescatore, T.S. and Senatore, M., 1986. A comparison between a present-day (Taranto Gulf) and a Miocene (Irpinian Basin) foredeep of the Southern Apennines (Italy). In: Foreland Basins (Eds P.A. Allen and P. Homewood). Spec. Publ. Int. Assoc. Sediment., 8, 169–182.

Pescatore, T., 1992. La sedimentazione miocenica nell'Appennino campano-lucano. Mem. Soc. Geol. It., 41, 37-46.

Pickering, K.T., Hodgson, D.M., Platzman, E., Clark, J.D. and Stephens, C., 2001. A new type of bedform produced by backfilling processes in a submarine channel, Late Miocene, Tabernas-Sorbas Basin, SE Spain. Journal of Sedimentary Research, 71, 692-704.

Posamentier, H.W., Erskine, R.D., Mitchum, R.M., Jr, 1991. Models for Submarine-Fan Deposition within a Sequence-Stratigraphic Framework, in Seismic Facies and Sedimentary Processes of Submarine Fans and Turbidite Systems, New York, NY, Springer New York, Frontiers in Sedimentary Geology, 127–136.

Posamentier, H.W., Kolla, V., 2003. Seismic geomorphology and stratigraphy of depositional elements in deep-water settings: Journal of Sedimentary Research, 73, 367–388.

Prélat, A., Hodgson, D.M., 2013. The full range of turbidite bed thickness patterns in submarine lobes: controls and implications: Journal of the Geological Society, London, 170, 209–214.

Prélat, A., Hodgson, D.M., Flint, S.S., 2009. Evolution, architecture and hierarchy of distributary deep-water deposits: a high-resolution outcrop investigation from the Permian Karoo Basin, South Africa. Sedimentology, 56, 2132–2154.

Pyles, D.R., Jennette, D.C., Tomasso, M., Beaubouef, R.T. and Rossen, C., 2010. Concepts learned from a 3D outcrop of a sinuous slope channel complex: beacon channel complex, Brushy Canyon Formation, West Texas, U.S.A. Journal of Sedimentary Research, 80, 67-96.

Schwarz, E., Arnott, R.W.C., 2007. Anatomy and evolution of a slope channel-levee complex set (Neoproterozoic Isaac Formation, Windermere Supergroup, southern Canadian Cordillera): implications for reservoir characterization. Journal of Sedimentary Research, 77, 89–109.

Selli, R., 1962. Il Paleogene nel quadro della geologia dell'Italia meridionale. Memorie della Società Geologica Italiana, 3 (7).

Stevenson, C.J., Jackson, C.A. L., Hodgson, D.M., Hubbard, S.M., Eggenhuisen, J.T., 2015. Deep-water sediment bypass. Journal of Sedimentary Research, 85, 1058-1081.

Stright, L., Stewart, J., Campion, K., Graham, S., 2014. Geologic and seismic modeling of a coarse-grained deep-water channel reservoir analog (Black's Beach, La Jolla, California). AAPG Bulletin, 98, 4, 695– 728.

Talling, P.J., Masson, D.G., Sumner, E.J., Malgesini, G., 2012. Subaqueous sediment density flows: Depositional processes and deposit types. Sedimentology, 59, 1937–2003.

Thurmond, J., Loseth, T., Rivenaes, J., Martinsen, O., Xu, X., Aiken, C., 2006. Using outcrop data in the 21st Century–New methods and applications, with example from the Ainsa Turbidite System, Ainsa, Spain. Deep-Water Outcrops of the World Atlas, Tulsa, OK, American Association of Petroleum Geologists Special Publication CD-ROM.

Vezzani, L., Festa, A., Ghisetti, F. C., 2010. Geology and tectonic evolution of the Central-Southern Apennines, Italy. Geological Society of America Special Papers, 469, 1-58.

Wynn, R.B., Talling, P.J., Amy, L., 2005. Imaging bed geometry and architecture of massive sandstones in the Fontanelice Channels, Italian Apennines, using new digiscoping techniques. Sedimentary Geology, 179, 153-162.

Chapter

4

Detailed outcrop characterization of high-frequency sequence boundaries in the Plio Peri-Adriatic shallow marine succession revealed through UAV cliff-side digital outcrop mapping

From Messinian to Pleistocene: tectonic evolution and stratigraphic architecture of the Central Adriatic Foredeep (Abruzzo and Marche, Central Italy)

M. Ghielmi[1], G. Serafini[1], A. Artoni[2], C. Di Celma[3], A. Pitts[3]

[1]Eni Upstream & Technical Services, San Donato Milanese, Milano - Italy
[2]Department of Chemistry, Life Sciences and Environmental Sustainability - Università di Parma, Parma - Italy
[3]Scuola di Scienze e Tecnologie - Università di Camerino, Camerino - Italy

Preface:

This work was featured as one of several stops presented during the 2019 International Association of Sedimentologists meeting in Rome. This chapter is a presented as a manuscript which is planned for submission in fall of 2020

Detailed outcrop characterization of high-frequency sequence boundaries in the Plio Peri-Adriatic shallow marine succession revealed through UAV cliff side digital outcrop mapping

In Preparation for journal submission in fall 2020

Abstract

Sequence stratigraphy principles applied to shallow marine clastic successions represent a powerful tool for understanding the signals of base level change recorded by marine sedimentary systems. However, when dealing with tall cliff exposures, the subtle details such as stratal termination geometry, grain size jumps, and bed-scale sedimentary structures that characterize sequence boundaries are often just beyond the reach field geologists. However, taking advantage of the range of highly accessible Unmanned Aerial Vehicles (UAV) for conducting aerial surveys and using Structure from Motion (SfM) photogrammetry to construct Virtual Outcrop Model (VOM) can bridge the gap to enable the detailed inspection of previously inaccessible outcrop sections.

We present an integrated study focused on the middle Pliocene (Piacenzian) shallow-marine succession superbly exposed on the cliffs below the town of Montefalcone Appennino (southern Marche). This work involves facies analysis and sequence stratigraphy revealed by combining stratigraphic field methods and the use of Unmanned Aerial Vehicle (UAV) cliff-side scanning using Structure from Motion (SfM) photogrammetry to create high-resolution Virtual Outcrop Models. These VOMs are constructed by the collection of close range (<10 meters) cliff-side photo sets used to build immersive outcrop reconstructions which enable the close inspection of bed scale details which characterize the largest elements visible on the outcrop. These VOMs are used as a resource that is paired with other data sets such as measured logs and other field data.

The studied section is about 100 m thick and comprises a dominantly aggradational stack of shoreface deposits truncated by a series of laterally extensive wave-cut ravinement surfaces interpreted to have formed during transgressive erosion. These surfaces form the boundaries of stratal units regarded as high-frequency sequences controlled by minor relative sea-level changes. The internal architecture of individual sequences is characterized by the presence of three main facies associations, which are differentiated by grain size and by physical and biogenic sedimentary structures.

Introduction

High resolution 3D geologic data in the form of point clouds or surface reconstructions, have become a key tool for describing and measuring outcrop and rock features for a wide range of geoscience applications (McCaffrey et al., 2005; Bemis et al., 2014; Tavani et al., 2014). This type of data was traditional collected using expensive and highly technical laser-scanning equipment usually in the form of Aerially acquired or ground based Light detection and Ranging (LIDAR). However, recent advancements in the quality, performance, and accessibility of consumer-grade Unmanned Aerial Vehicles (UAVs) with onboard cameras matched with computer software for rendering georeferenced 3D virtual outcrop models (VOM) offer accessible solutions for geoscience research. In the last 5 years, Structure from Motion as a topographic survey technique, has been demonstrated in several cases including the study of stratigraphic architecture in deep water systems (Pitts et al., 2017; Nieminski et al., 2017, Nesbit et al., 2018), structural analysis of regional features (Tavani et al., 2014), and characterization of fracture surface roughness (Corradetti et al., 2017; Zambrano et al., 2019). In the case of sedimentology and stratigraphic studies UAV based SfM outcrop surveys provide two clear benefits; the ability to reach inaccessibly high portions of cliff-side outcrops, and the flexibility to obtain perspectives from viewpoints both at close ranges to observe bed-scale features and medium ranges to characterize the broad scale features. These two advantages of the UAV-based studies provide a means to obtain outcrop data sets in a more efficient and practically way than a field geologist could produce either from the ground of hanging from a rope at the exposure face.

This approach of combining UAV photo collection and sophisticated computer software for rendering 3D VOMs to characterize stratigraphic and sedimentological features provides a

more cost effective, more reliable, and flexible platform for collecting data sets that were traditional obtained by laser scanning (Bilmes et al., 2019). Although laser scanning still remains a very effective means for collecting the same data, UAV SfM procedures do practically the same job however for a fraction of the price. This not only bridges the gap for academic or early career scientist who have limited research funds, it also in a sense democratizes 3D data collection, by allowing greater access to this type of technology.

Near shore systems, like the units exposed at Montefalcone Appennino are highly sensitive to base level changes and their distribution of facies and bounding stratal surfaces enable powerful inferences of base level changes and the respective response of sedimentary systems. These types of interpretations have large implications for reconstructions of past sea-level fluctuations and also give predictive powers for exploration in petroleum geology. However, in many cases, the keys to these types of broad interpretations rely on sub decameter outcrop features which are only observed from very close ranges. Often, when dealing with large and expansive cliff-side exposures, bed-scale architecture is difficult to reach and/or track across the outcrop.

The goal of this work is to use UAV based SfM photogrammetry to enhance facies recognition and correlation of key stratal surfaces across several hundred meters in order to present a more complete depositional history of this interval of the Periadriatic basin fill.

Geologic Setting

The Plio-Pleistocene Central Periadriatic Basin (CPB), also regarded as the Pescara Basin (Ghielmi et al., 2013) is one depocenter which is part of the larger Periadriatic basin extending from the Po plain in the north until the Gulf or Taranto to the south. This sedimentary succession records syn- and post stages of the Apennine orogenic event (Artoni, 2013). The deposits of the CPB sit eastward of the fold and trust belt of the Apennine chain and unconformably on top of the Miocene foredeep deposits of the Laga Basin (Bigi et al., 2009; Centamore et al., 1991; Milli et al., 2007) (Fig. 4.1). The sedimentary succession of the CPB is comprised of mostly marine and some terrigenous deposits ranging from, shallow marine (Cantalamessa et al., 1986; Ori et al., 1991) to shelf-slope mudstones and conglomerates (

Cantalamessa, 2009; Di Celma, 2011; Di Celma and Cantalamessa, 2012; Di Celma et al., 2010, 2013, 2014) and fluvial deposits (Di Celma et al., 2015).

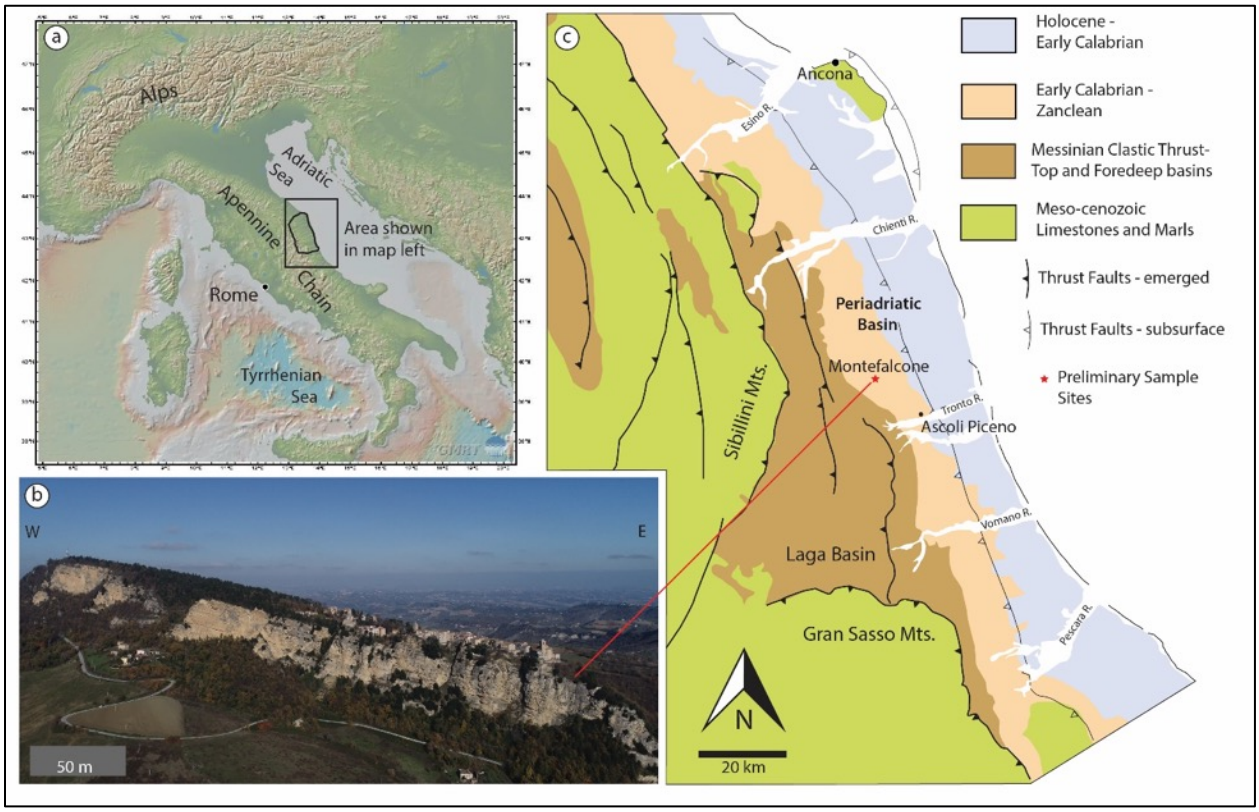

Figure 4.1. Regional geologic setting area. a) Map of Italy showing the study area in context with the Apennine Chain. B) Aerial view of Montefalcone Apennino. C) Geologic sketch map of the region surrounding the study area – structures simplified from Artoni (1993,2007,2013).

The Marche-Abruzzo sector of the central Apennine chain-foredeep system evolved within the general context of the Cenozoic convergence of the African and Eurasia, Corsica-Sardinia and Adria-Apulian plates (Doglioni, 1991; Patacca and Scandone, 2007; Vezzani et al 2010). From the Oligocene into the Miocene, the central Apennine region was broadly affected by NE-directed compression that produced a series of thrust sheets composed of detached blocks of Jurassic-Cretaceous pelagic and basinal limestones that formed along the passive Tethys margin (Vezzani et al., 2010 and references therein). Lithospheric loading resulting from tectonic accretion of these major thrust domains created a series of eastward-migrating thrust-top and foredeep basins, which host thick packages of clastic sediments. The best known of these basins are the Chattian-Aquitanian Macigno turbidite complex (Ghibaudo, 1980; Ricci-Lucchi 1990, Dunkl et al. 2001), the late Langhian-Tortonian Marnoso-arenacea

Formation (MAF) (Bouma, 1962; Ricci-Lucchi & Valmori, 1980; Talling et al., 2006; Tinterri & Tagliaferri, 2015; Tagliaferri & Tinterri, 2016) and the Tortonian-Messinian Laga Formation (Centamore et al., 1978; Ricci-Lucchi, 1986; Bigi et al., 1999; Stalder et al., 2018). Among these three systems, the MAF and LB are considered to be among the classic turbidite localities of the world because key depositional models and facies schemes that provide the fundamentals of modern deep water sedimentology were first described there by Ricci Lucchi (1969; 1975; 1978; 1981, Mutti and Ricci Lucchi, 1972). The continued eastward progression of thrust fronts towards the foreland, involved progressively younger and easternmost deposits and gradually shifted to the east (Ori et al., 1985; Ricci Lucchi, 1986; Artoni, 2007) youngest of these clastic basins is the Periadriatic Basin which record the terminal step in the eastward migration across the orogen.

Study area

The study area is focused on the cliff-side exposure directly under the town of Montefalcone Appennino in the southern Marche region approximately 20 km NW of Ascoli Piceno (Fig 4.1). The deposits of this exposure form an eastward dipping wedge-like body of predominantly sandstone. This unit can be traced for approximately 10 km in the topography as a N-S trending promontory.

This study focuses on the basal portion of the Central Periadriatic Basin (CPB). This portion of the basin is oriented N-S and occupies an approximately 30 km-wide zone between the eastern flank of the Apennine Chain until the Adriatic coast of the Marche and Abruzzi regions.

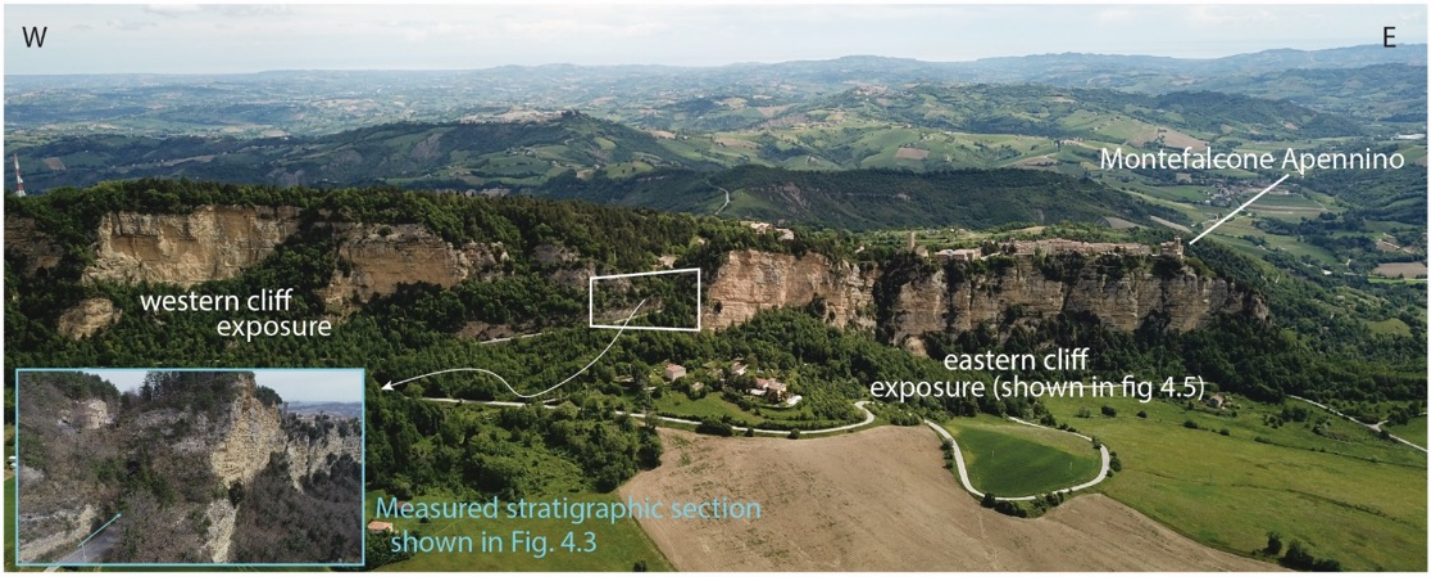

Figure 4.2. Aerial overview of the cliff-side exposures beneath the village of Montefalcone.

Methods

The basis of this study consists of a combination of traditional and digital field methods integrated into a comprehensive data set. Physically gained field data include a complete measured stratigraphic reference along a road which cuts the entire section and presents the only location where it is possible to physically measure the stratigraphy (Fig. 4.2). The measured section is complimented by high resolution outcrop scanning using UAV-based Structure from Motion (SfM) photogrammetry. The outcrop scanning was performed with the DJI Phantom 4 Pro quadcopter with an onboard 20 MP camera and GPS sensor.

Outcrop scanning and data analysis followed an integrated procedure (Fig. 4.3) and involve 6 steps further explained in the following paragraphs.

1. Medium-range Outcrop scanning:

The first aerial survey consisted of collecting 167 aerial photos covering the entire section at a medium range. Here medium range is defined as approximately 10-15 meters from the outcrop. The photos were captured in a general un-calibrated manner however focused on obtaining photos with upwards of 50% inter-photo overlap (Fig 4.3).

2. Medium-range VOM processing and analysis:

Following the field data acquisition, the photos were processed using Agisoft PhotoScan following the procedure outlined by previous authors (Pitts et al.,2017; Nesbit 2018) to create a photo-realistic 3D VOM of the entire outcrop. Using a combination of the 3D model and the input photos, a broad stratigraphic framework was established with the identification of key stratigraphic surfaces to be investigated on a 2nd outcrop survey.

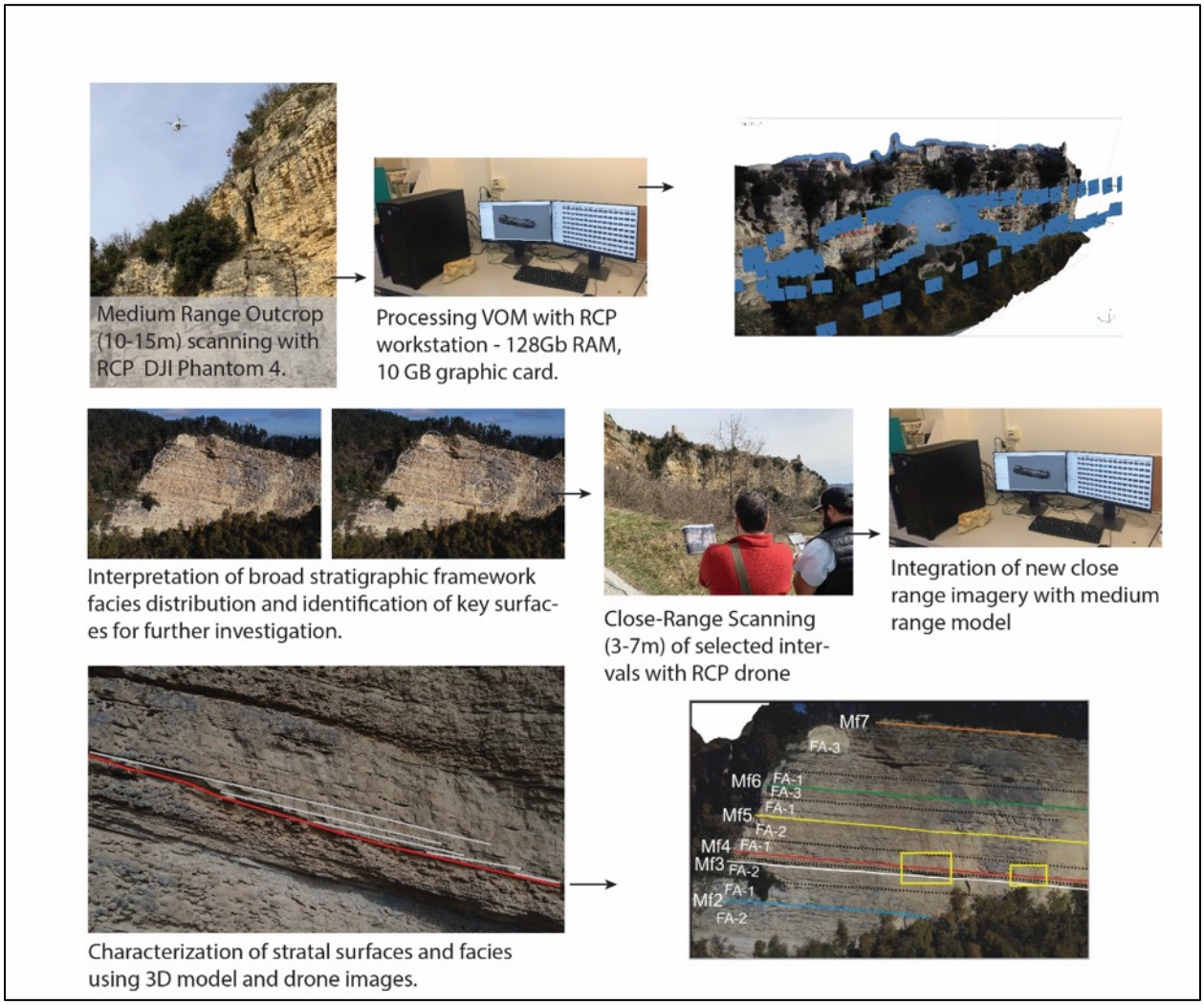

Figure 4.3. UAV cliffside scanning workflow

3. Close-range Outcrop scanning:

Using the preliminary findings of the medium range VOM in a printed outcrop schematic, a second aerial survey was performed with aerial photos acquired from a close-range, here

defined as 3-5 meters. The photo acquisition proceeded in a manner to trace selected stratal surfaces along the outcrop to clarify the stratal terminations and facies distributions found in close vicinity to those surfaces. During this step, an additional ~250 photos were gathered.

4. Medium-range VOM processing and analysis:

Following the second field campaign, the new close-range photo set was integrated into the previously constructed VOM to create a larger more immersive digital outcrop model. This VOM was used to fully characterize the facies distribution and laterally persistent stratal surfaces.

5. Computer-aided Geological Interpretation:

Analysis of VOM data was done inside Agisoft PhotoScan using the 3D poly line tool functionality. This basic yet powerful feature inside PhotoScan allows the careful tracing of stratigraphic surfaces which are projected both inside the 3D VOM environment and also onto the original input photos. In this way, interpretations were made by working between the 3D model to recognize bedding geometries and outcrop scale features, and then using the input photos to refine the larger interpretations according the smallest details visible in the photos.

Results:

Based on careful analysis of UAV imagery cross-checked with the measured stratigraphic section, the overall Montefalcone succession is about 100 meters thick and comprises a cyclical stack of wave- and storm-dominated mixed silici-bioclastic shoreface deposits truncated by a series of laterally extensive wave-cut ravinement surfaces interpreted to have formed during transgressive erosion (Fig 4.4, 4.5). These 7 surfaces form the boundaries of stratal units regarded as high-frequency sequences controlled by minor relative sea-level changes. The internal architecture of individual sequences is characterized by presence of three main facies associations, which are differentiated by grain size, bedding thickness and geometry, sedimentary structures, and general intensity of bioturbation. In the following

paragraphs, the details of these facies associations and strata surfaces are presented with respect to their position along the expansive exposure.

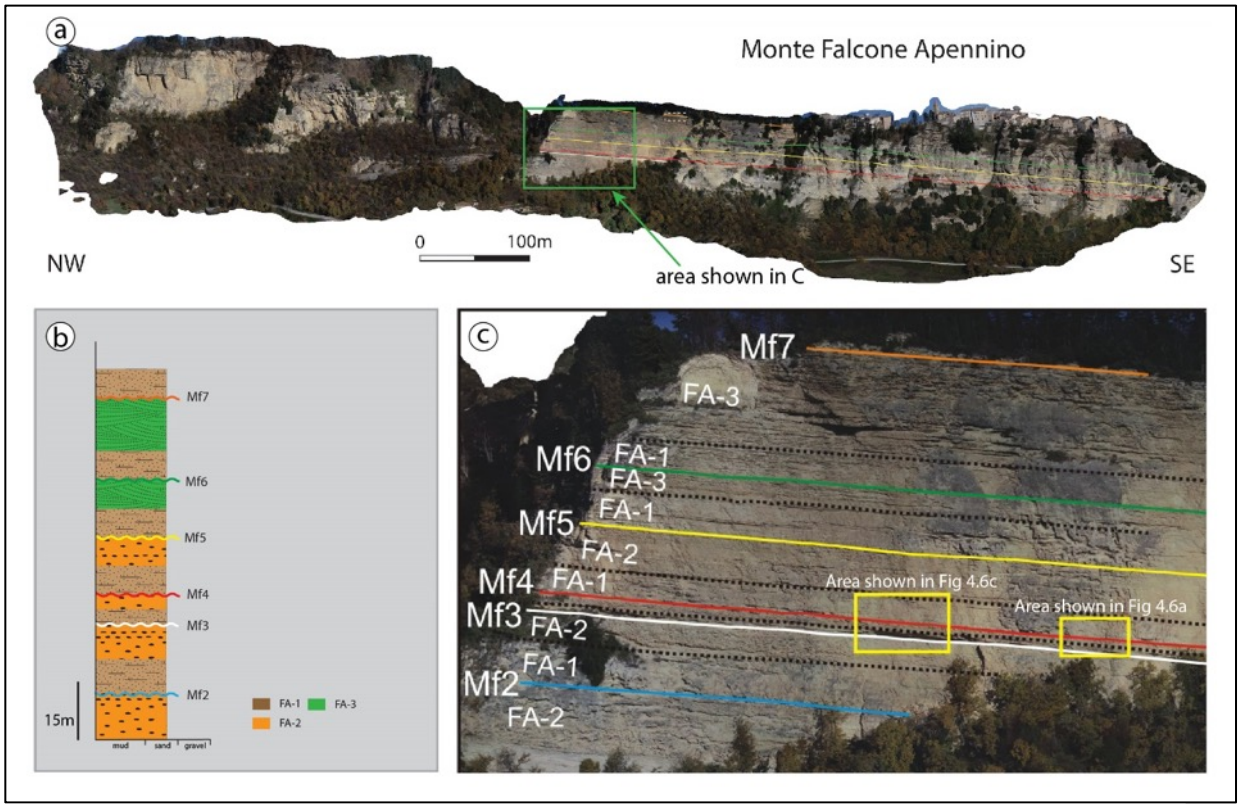

Figure 4.4. Montefalcone stratigraphic scheme. A) Photo orthomosaic showing the entire exposure of the Montefalcone cliff. B) Generalized stratigraphic section. C) Facies schematic showing vertical distribution of facies and key stratigraphic surfaces.

Facies Analysis

Facies Association 1 (FA-1)

Description: This unit is comprised of 3-5-meter-thick packages of primarily amalgamated thin to medium bedded, fine to medium-grained sandstones exhibiting predominantly plane-parallel laminated with some swaley cross-stratification (Fig. 4.6). Facies Association A1 is always present at the base of each sequence where it shows a subtle 5-10-degree strata onlap terminations onto the marine transgressive surfaces of erosion. At the base, FA-1 packages are commonly found with 10-15 cm thick intervals of pebble conglomerate intervals with extra-basinal clasts which mantle the lower surfaces. Conglomerates are also found throughout FA-1 intervals as isolated laterally discontinuous lenses ranging from 1-25 cm in thickness. FA-1 shows low intensity bioturbation, primarily limited to horizontal *Ophiomorpha*.

Interpretation: Based on the grain size and sedimentary structures and relatively low intensity of bioturbation, these facies indicates deposition in the middle shore face. Based on their grain size, composition, and relationship to the underlying erosional surfaces, the conglomerate intervals at the base of the FA-1 are interpreted as forming during phases of sediment bypass during transgressive phases (Zecchin et al., 2017)

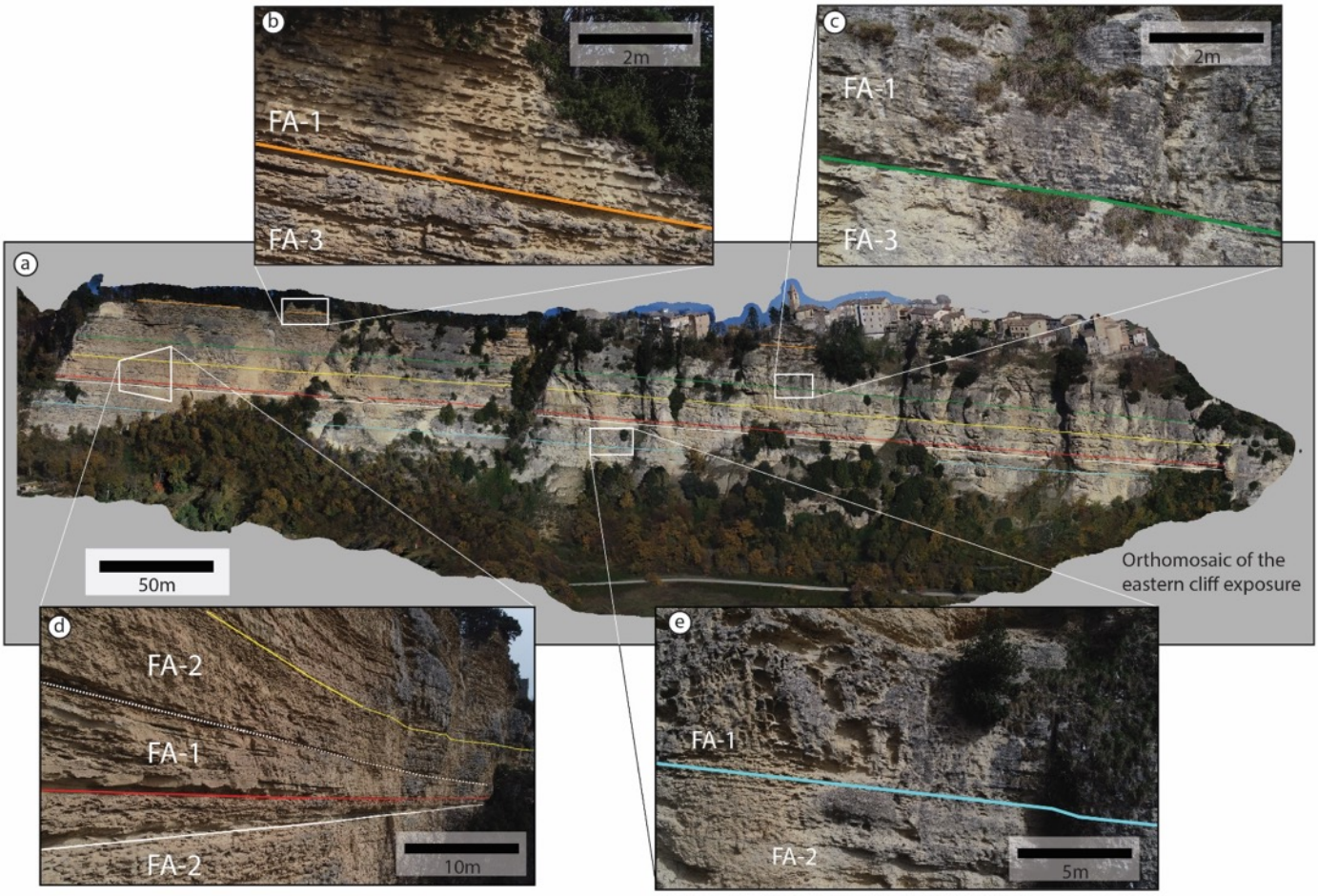

Figure 4.5. Facies Associations and outcrops details interpretted from aerial imager and Digital outcrop model. A) Orthomosaic of the the eastern portion of the exposed section. B) Details of stratal surface Mf7 showing FA-1 overlying FA-3 along a marine ravinament surface showing a low angle onlap stratal termination. C) Details of surface Mf6 with FA-1 overlying FA-3 along a MRS showing long-angle onlap strata terminations. D) Oblique photo taken parallel to the cliff fae showint stratal surface Mf3, Mf4,and Mf5. E) Details of stratal surface Mf2.

Facies Association 2 (FA-2)

Description: This Facies Association is comprised of 2-10-meter-thick packages of thoroughly bioturbated fine to coarse grained sandstones with pebbles and broken shell material (Fig 4.7). Pebbles and shell material are variably dispersed throughout the section without any

apparent sorting or organization. Furthermore, bioturbation is so intense, that the preexisting sedimentary fabric is practically undistinguishable. Lower intervals of FA-2 are round in gradational contact with FA-1. This unit can be individuated primarily based on the general level of bioturbation.

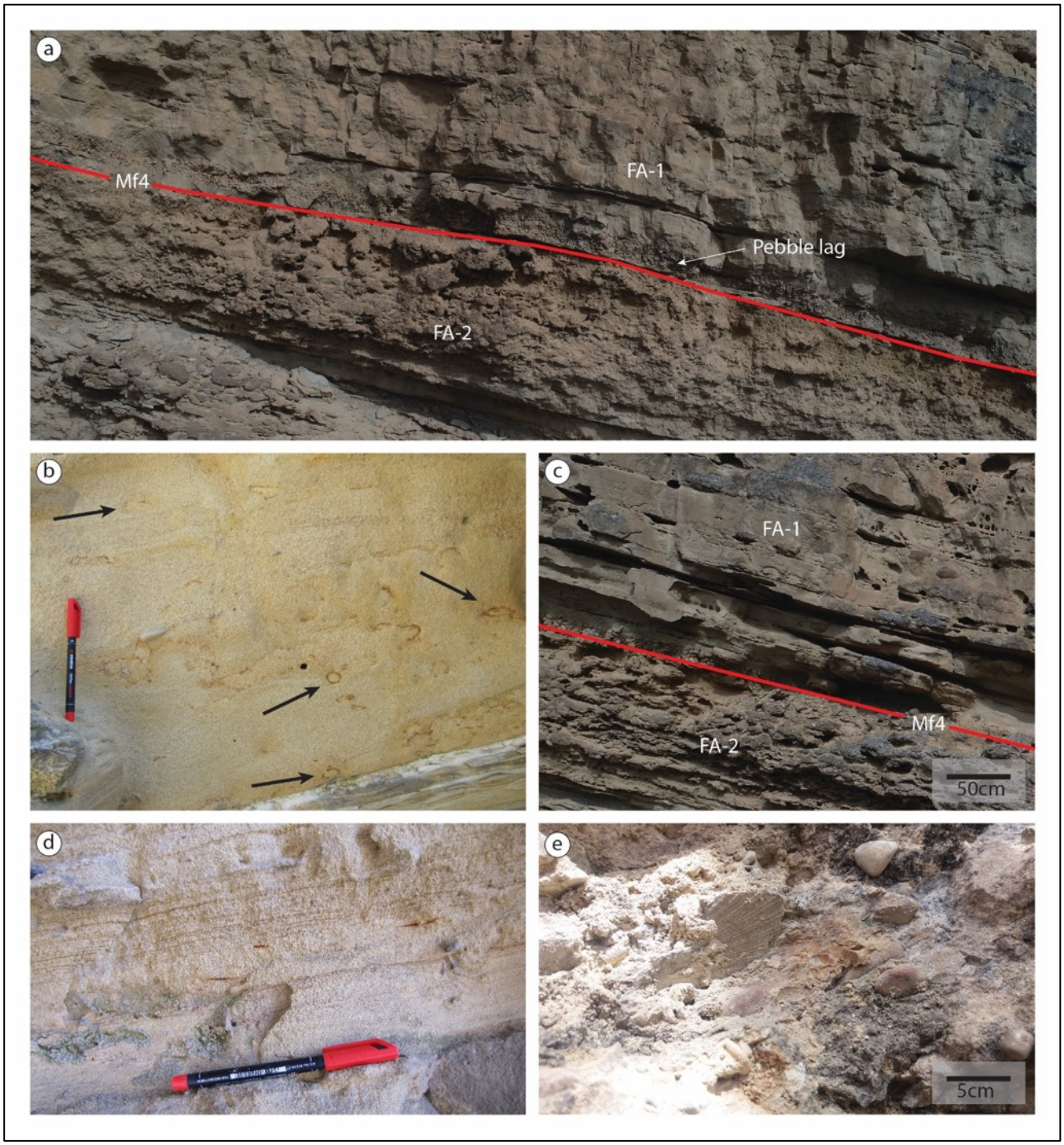

Figure 4.6. Facies FA-1 Details. A) Ophiomorpha burrows in fine-medium sandstones. B) FA-1 plane parallel bedded sandstones overlying Mf4 surface showing a low angle onlap strata termination and pockets of pebble-cobble conglomerates mantled over the MRS surface. C) Plane parallel laminated sandstone details. D) Pectin fossil in pebbly sandstone.

Interpretation: Based on the amount of sediment reworking, intermixing of grain population, the excessive amount of bioturbation and lack of clear sedimentary structures this unit is interpreted as deposits in the lower shoreface setting.

Facies Association 3 (FA-3)

Description: This Facies Association is comprised of 2-4-meter-thick packages of fine-grained hummocky-bedded sandstones with thin, laterally discontinuous stringers and isolated clusters of small pebbles (Fig. 4.8). FA-3 is found in the stratigraphically higher portions of the exposure in the upper 3 sequences where it overlies FA-1 with a gradational contact.

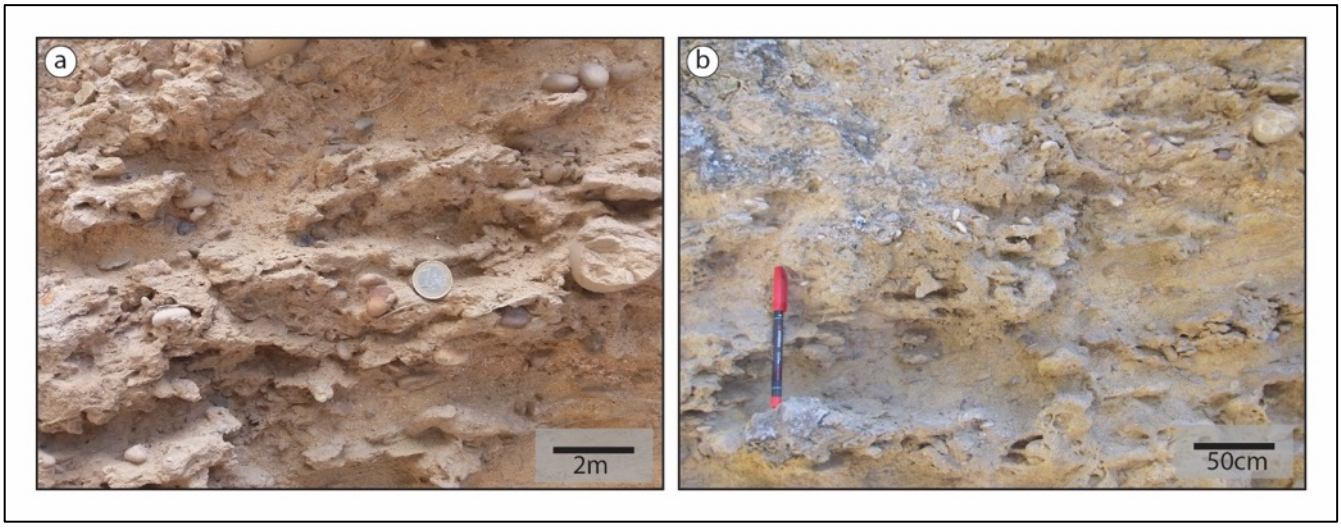

Figure 4.7. FA-2 details. A) Completely reworked deposits in which grain populations have been mixed. B) Bioturbated sandstone, showing faint relict bedding.

Interpretation: Based on the abundance of HCS, this unit suggest deposition in the lower shoreface – off shore transition environment. Here the sediments were affected oscillatory action of storm-wave processes that organized the sediment into HCS in a shallow marine environment just below fair-weather wave base.

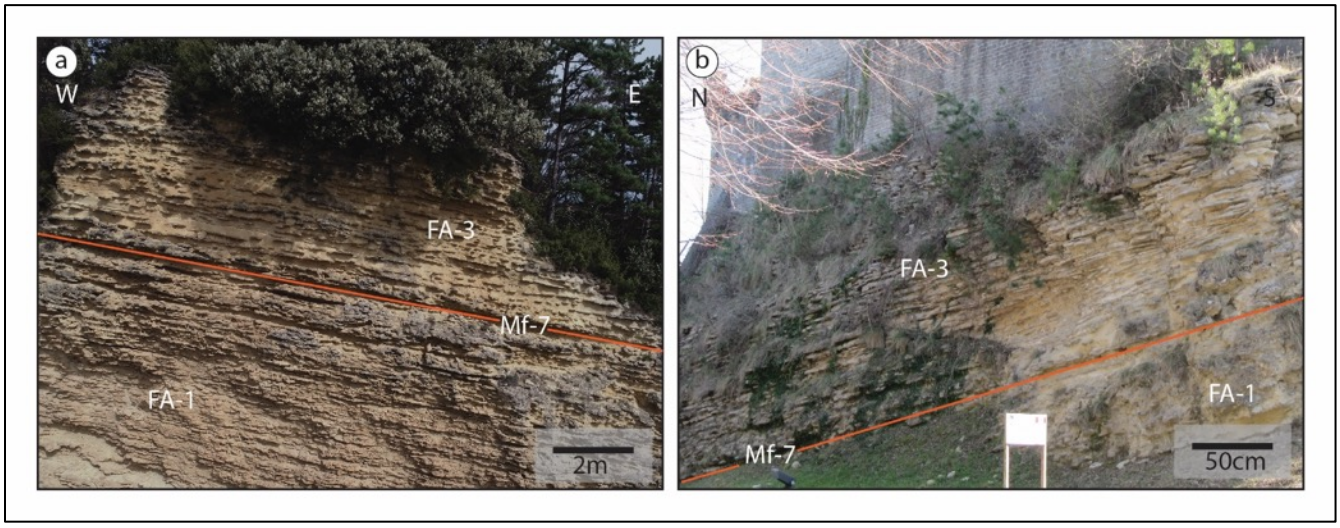

Figure 4.8. FA-3 Details. A) W-E oriented view of FA-3 onlapping onto surface Mf7. B) N-S oriented view of FA-3 onlapping onto surface Mf7

Discussion

High Frequency Sequence Boundaries:

This study interprets the presence of 7 laterally continuous sequence boundaries representing marine transgressive surfaces of erosion. Each of these surfaces are driven by a raise in sea level by several meters and an accompanying landward shift in the shoreline.

Role of sedimentation and accommodation space:

This succession records an overall aggradational stack of shallow marine deposits. These units are interpreted as being deposited in the water depths up to ~25 meters. The overall thickness of the Montefalcone unit indicates that the overall deposition of this unit must have been influenced by subsidence occurring at a rate equal to or slightly out-pacing sedimentation rate. Superimposed onto this overall are unconformity bound sequences recording high-frequency sea-level changes.

The present study identifies 7 wave-ravinement surfaces which bound high frequency sequences which document depositional environment changes and a landward migration of the coastline driven by relative sea-level rise. These surfaces indicate periods of wave-driven erosion during shoreline transgression. This is further supported by the presence of

transgressive conglomerate lag deposits and shell concentrations at the base of FA-1 directly overlying wave-ravinement surfaces.

Conclusions

1) The lower Pliocene Montefalcone succession exhibits, meter-scale to decameter-scale shallow marine cyclicity linked to high-frequency sequences linked to shoreline transgressive shifts linked to relative sea-level change.

2) In the case of the Montefalcone succession, the extremely limited access to the outcrop and the general poor quality of the outcrop along the roadcut and only possible location for a reference section offer an incomplete picture of the exposure. Even in the rare cases of fresh exposures, the perspectives often do not permit the optimum view angle and position at which to observe subtle yet extremely important sedimentological and stratigraphic details which lead to better characterization of the outcrop. The interpretations here in this work, such as onlap strata terminations were discovered only through the use of UAV outcrop scanning which was then calibrated with the measured-reference section.

3) While there are many benefits to the use of this approach, the UAV-SfM generated VOM model still contains some limitations. The first is that it is still difficult to create virtual outcrop models that contains the absolute 1:1 equivalent resolution as the input photos. This implies that the VOM is best used in conjunction with the outcrop-referenced input photos that can help to improve the interpretations.

References:

Artoni, A. (2007) Growth rates and two-mode accretion in the outer orogenic wedge-foreland basin system of central Apennine (Italy). *Boll. Soc. Geol. It*., 126, 531-556.

Artoni, A. (2013) The Pliocene-Pleistocene stratigraphic and tectonic evolution of the Central sector of the western Periadriatic Basin of Italy. *Marine and Petroleum Geology*, 42, 82-106.

Artoni, A. & Casero, P. (1997). Sequential balancing of growth structures, the late Tertiary example from the Central Apennine. *Bull. Soc. Geol. France*, 168, 35-49.

Bemis, S. P. *et al.* Ground-based and UAV-Based photogrammetry: A multi-scale, high-resolution mapping tool for structural geology and paleoseismology. *J. Struct. Geol.* **69**, 163–178 (2014).

Bigi, S., Calamita, F., Cello, G., Centamore, E., Deiana, G., Paltrinieri, W., Pierantoni, P,. & Ridolfi, M. (1999). Tectonics and sedimentation within a Messinian foredeep in the central Apennines, Italy. *Jour. Petrol. Geol.*, *22*(1), 5–18. doi.org/10.1111/j.1747-5457.1999.tb00456.x

Cantalamessa, G., Centamore, E., Colalongo, M.L., Micarelli, A., Nanni, T., Pasini, G., Potetti, M. and Ricci Lucchi, F., (1986) Il Plio-Pleistocene delle Marche. In: La Geologia delle Marche (Eds E. Centamore and G. Deiana). Studi Geologici Camerti, Special Volume, 61-81.

Cantalamessa, G., Di Celma, C., Potetti, M., Lori, P., Didaskalou, P., Albianelli, A., Napoleone, G., 2009. Climatic control on deposition of upper Pliocene deepwater gravity-driven strata in the Apennines foredeep (central Italy): correlations to the marine oxygen sea isotope record. In: In: Kneller, B., Martinsen, O.J., McCaffrey, B. (Eds.), External Controls on Deep Water Depositional Systems: Climate, Sea-Level, and Sediment Flux, vol. 92. SEPM Spec. Publ., pp. 247–259. https://doi.org/10.2110/sepmsp.092.247

Centamore, E. (1986). Carta Geologica delle Marche alla scala 1:250.000. In: *La Geologia delle Marche* (eds. E. Centamore & G. Deiana), *Studi Geol. Camererti*, Camerino, 1 map.

Corradetti, A., McCaffrey, K., De Paola, N., & Tavani, S. (2017). Evaluating roughness scaling properties of natural active fault surfaces by means of multi-view photogrammetry. *Tectonophysics*, *717*, 599–606. https://doi.org/10.1016/j.tecto.2017.08.023

Di Celma, C., Cantalamessa, G., Didaskalou, P., Lori, P., 2010. Sedimentology, architecture, and sequence stratigraphy of coarse-grained, submarine canyon fills from the Pleistocene (Gelasian-Calabrian) of the Peri-Adriatic basin, central Italy. Mar. Pet. Geol. 27, 1340–1365. https://doi.org/10.1016/j.marpetgeo.2010.05.011.

Di Celma, C., 2011. Sedimentology, architecture, and depositional evolution of a coarse-grained submarine canyon fill from the Gelasian (early Pleistocene) of the Peri- Adriatic basin, Offida, central Italy. Sediment. Geol. 238, 233–253. https://doi.org/10.1016/j.sedgeo.2011.05.003.

Di Celma, C., Cantalamessa, G., 2012. Off-shelf sedimentary record of recurring global sea-level changes during the Plio-Pleistocene: evidence from the cyclic fills of ex- humed slope systems in central Italy. J. Geol. Soc. 169, 643–646. https://doi.org/10.1144/jgs2012-041.

Di Celma, C., Cantalamessa, G., Didaskalou, P., 2013. Stratigraphic organization and predictability of mixed coarse-grained and fine-grained successions in an upper slope Pleistocene turbidite system of the Peri-Adriatic basin. Sedimentology 60, 763–799. https://doi.org/10.1111/j.1365-3091.2012.01359.x.

Di Celma, C., Teloni, R., Rustichelli, A., 2014. Large-scale stratigraphic architecture and sequence analysis of an early Pleistocene submarine canyon fill, Monte Ascensione succession (Peri-Adriatic central Italy). Int. J. Earth Sci. 103, 843–875. https://doi.org/10.1007/s00531-013-0984-3.w

Di Celma, C., Pieruccini, P., Farabollini, P., 2015. Major controls on architecture, sequence stratigraphy and paleosols of middle Pleistocene continental sediments (“Qc Unit”), eastern central Italy. Quat. Res. 83, 565–581. https://doi.org/10.1016/j.yqres.2015.01.006.

Dunkl, I., Di Giulio, A., & Kuhlemann, J. (2001). Combination of single-grain fission-track chronology and morphological analysis of detrital zircon crystals in provenance studies: sources of the Macigno Formation (Apennines, Italy). *Jour. Sed. Research, 71*(4), 516-525. doi.org/10.1306/102900710516

Ghibaudo, G. (1980). Deep-sea fan deposits in the Macigno Formation (middle-upper Oligocene) of the Gordana Valley, northern Apennines, Italy. *Jour. Sed. Research*, *50*(3), 723-741. doi.org/10.1306/212F7ACC-2B24-11D7-8648000102C1865D

Ghielmi, M., Minervini, M., Nini, C., Rogledi, S., & Rossi, M. (2013). Late Miocene-Middle Pleistocene sequences in the Po Plain - Northern Adriatic Sea (Italy): The stratigraphic record of modification phases affecting a complex foreland basin. *Marine and Petroleum Geology*, *42*, 50–81. https://doi.org/10.1016/j.marpetgeo.2012.11.007

McCaffrey, K., Jones, R., Holdsworth, R., Wilson, R., Clegg, P., Imber, J., … Trinks, I. (2005). Unlocking the spatial dimension: digital technologies and the future of geoscience fieldwork. *Journal of the Geological Society*, *162*(6), 927–938. https://doi.org/10.1144/0016-764905-017

Nieminski, N. M. & Graham, S. A. Modeling Stratigraphic Architecture Using Small Unmanned Aerial Vehicles and Photogrammetry: Examples From the Miocene East Coast Basin, New Zealand. *J. Sediment. Res.* **87**, 126–132 (2017).

Nesbit, P. R., Durkin, P. R., Hugenholtz, C. H., Hubbard, S. M. & Kucharczyk, M. 3-D stratigraphic mapping using a digital outcrop model derived from UAV images and structure-from-motion photogrammetry. *Geosphere* **14**, 2469–2486 (2018).

Ori, G. G. & Friend, P. F. Sedimentary basins formed and carried piggyback on active thrust sheets. *Geology* **12**, 475–478 (1984).

Ori, G.G., Serafini, G., Visentin, C., Ricci Lucchi, F., Casnedi, R., Colalongo, M.L. and Mosna, S. (1991) The Pliocene-Pleistocene Adriatic Foredeep (Marche and Abruzzo, Italy): an integrated approach to surface and subsurface geology. In: Adriatic Foredeep Field Trip, 3rd EAPG Conference., Florence May 26-30, pp. 85.

Pitts, A. D., Casciano, C. I., Patacci, M., Longhitano, S. G., Di Celma, C., & McCaffrey, W. D. (2017). Integrating traditional field methods with emerging digital techniques for enhanced outcrop analysis of deep water channel-fill deposits. *Marine and Petroleum Geology*, *87*, 2–13. https://doi.org/10.1016/j.marpetgeo.2017.05.001

Ricci Lucchi, F. (1969). Composizione e morfometria di unconglomerato risedimentato nel flysch miocenico rom-agnolo (Fontanelice, Bologna): *Giornale di Geologia*, 36, 1–47.

Ricci Lucchi, F. (1975). Miocene paleogeography and basin analysis in the Periadriatic Apennines (ed. C.H. Squyres), *Geology of Italy*. Tripoli, Petroleum Exploration Society of Lybia, 2, 129–236.

Ricci Lucchi, F. (1981) The Marnoso-arenacea turbidites, Romagna and Umbria Apennines. In: Excursion Guidebook, with Contribution on Sedimentology of some Italian Basins (Ed. F. Ricci Lucchi), pp. 229–303.\2nd IAS Eur. Meeting, Bologna

Ricci Lucchi, F. (1986) The Oligocene to Recent foreland basins of the northern Apennines. In*: Foreland Basins* (eds. P.A. Allen and P. Homewood), Blackwell, Freiburg. 105-140.

Ricci Lucchi, F. (1990). Turbidites in foreland and on-thrust basins of the northern Apennines. *Palaeogeography, Palaeoclimatology, Palaeoecology*, *77*(1), 51-66. doi.org/10.1016/0031-0182(90)90098-R

Ricci Lucchi, F. & Valmori, E. (1980) Basin-wide turbidites in Miocene, over-supplied deep sea plain: a geometrical analysis. *Sedimentology*, 27, 241-270. doi.org/10.1111/j.1365-3091.1980.tb01177.x

Stalder, N. F., Fellin, M. G., Caracciolo, L., Guillong, M., Winkler, W., Milli, S., Moscatelli, M., & Critelli, S. (2018). Dispersal pathways in the early Messinian Adriatic foreland and provenance of the Laga Formation (Central Apennines, Italy). *Sed. Geol.*, *375*, 289-308. https://doi.org/10.1016/j.sedgeo.2017.09.016

Talling, P. J., Amy, L. A., Wynn, R. B., Blackbourn, G., & Gibson, O. (2007). Evolution of turbidity currents deduced from extensive thin turbidites: Marnoso Arenacea Formation

(Miocene), Italian Apennines. *Jour. Sed. Research,* 77(3), 172–196. https://doi.org/10.2110/jsr.2007.018

Tavani, S., Granado, P., Corradetti, A., Girundo, M., Iannace, A., Arbués, P., … Mazzoli, S. (2014). Building a virtual outcrop, extracting geological information from it, and sharing the results in Google Earth via OpenPlot and Photoscan: An example from the Khaviz Anticline (Iran). *Computers and Geosciences*, *63*, 44–53. https://doi.org/10.1016/j.cageo.2013.10.013

Tinterri, R. & Tagliaferri, A. (2015). The syntectonic evolution of foredeep turbidites related to basin segmentation: facies response to the increase in tectonic confinement (Marnoso-arenacea Formation, Miocene, Northern Apennines, Italy). *Marine Petrol. Geol.*, 67, 81-110. doi.org/10.1016/j.marpetgeo.2015.04.006

Vezzani, L., Festa, A., & Ghisetti, F. C. (2010). Geology and Tectonic Evolution of the Central-Southern Apennines, Italy. (January), 1–58. https://doi.org/10.1130/2010.2469

Chapter

5

Sedimentological and stratigraphic signature of the Plio-Pleistocene tectonic events in the Southern Apennines, Italy: the Calvello-Anzi Basin case study

Marine and Petroleum Geology
Volume 116, June 2020, 104198

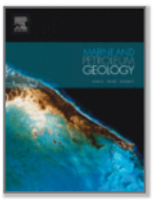

Research paper

Sedimentological and stratigraphic signature of the Plio-Pleistocene tectonic events in the Southern Apennines, Italy: The Calvello-Anzi Basin case study

Alan D. Pitts [a], Danica Jablonska [a], Valentino Di Donato [b], Stefano Mazzoli [a], Vincenzo Spina [c], Claudio Di Celma [a], Emanuele Tondi [a]

[a] University of Camerino, School of Science and Technology Geology Division, Italy
[b] University of Naples Federico II, Department of Earth Science, Italy
[c] Total E&P, Pau, France

Preface:

This chapter presents a published study in its pre-journal format. This work comprises an integrated approach combining geologic mapping, aerial and ground based SfM, and structural analysis to better define the evolution of one of several Plio-Pleistocene syntectonic basins of the southern sector of the Apennines. These basins and their clastic infill record key events in the late-stages of tectonic development of the Southern Apennine chain.

The Sedimentological and stratigraphic signature of the Plio-Pleistocene tectonic events in the Southern Apennines, Italy: the Calvello-Anzi Basin case study

Pitts, Alan[1]., Jablonska. Danica[1]., Di Donato, Valentino[2]., Mazzoli, Stefano[1]., Spina, Vincenzo[3]., Di Celma, Claudio[1]., Tondi, Emanuele[1]

1) University of Camerino, School of Science and Technology Geology Division
2) University of Naples Federico II, Department of Earth Science
3) Total E&P, Pau, France

Introduction

The integrated analysis of sedimentary and stratigraphic evolution of syn-tectonic basins represents a powerful tool to assess timing and style of driving tectonic forces by the response recorded in sedimentary systems (Butler et al., 2019). Syn-tectonic basins that develop directly above an active orogen (in the *wedge-top depozone sensu* De Celles and Giles 1996) are dynamic entities that maintain a detailed record of the geodynamic settings in which they evolve. In orogenic systems with polyphase tectonic histories, basin analysis reporting structural data alone often reveal an incomplete or convoluted narrative due to a high degree of overprinting. To build a more comprehensive picture, it is necessary to consult the sedimentary record to correlate the tectonic signals documented by the facies distributions and architecture of the basin fill stratigraphy. In these cases, syntectonic basin infills can provide a precise record of the tectonic signals; in particular, those containing shallow-, deep -marine and alluvial successions are extremely sensitive to tectonic pulses (Lickorish & Butler, 1996).

The Plio-Pleistocene thrust-top basins of the Southern Apennines occupy a crucial position in the overall chain structure by providing a specific sequence of strata to calibrate the timing and kinematics of the migration of the deformation occurring in this region. Additionally, this series of basins is important for defining the timing and style of deformation occurring at the orogenic front as it migrated across the chain structure. These basins developed on top of the Apennine allochthonous wedge after its emplacement onto the western portion of foreland carbonate platform (Apulian Platform) and with deposition occurring contemporaneously with the Apennine orogenic events, straddling the transition between the two major tectonic

phases affecting the Southern Apennine chain. The Plio-Quaternary Calvello-Anzi Basin (CAB) in the Southern Apennines, Italy, is one small member of a series of similarly-aged thrust-top basins positioned along the axial portion of the chain following a NW-SE lineament (Pieri et al. 1994). The orientation of the CAB appears to be roughly E-W, which along with the orientation of several of the neighboring Plio-Pleistocene basin, is oblique to the predominant NW-SE trending regional structural fabric.

The structural arrangement of the Southern Apennine chain and the kinematics of its tectonic history have been the focus of a large scientific literature over the past 2-3 decades. The whole architecture of the Apennine chain was described as forming a duplex structure (e.g. Patacca et al. 1990; Doglioni et al. 1994; Cello & Mazzoli 1998), until new, high-quality seismic data pointed out an inversion structure characterized by the reverse fault-slip reactivation of inherited normal faults (Shiner et al. 2004; Butler et al., 2004). The resulting buried Apulian Platform Belt (APIB; Mazzoli et al. 2012) is characterized by thick-skinned (or crustal ramp-dominated; Butler & Mazzoli, 2006) shortening involving the basement of the Apulian Platform (Improta & Corciulo, 2006; Steckler *et al.*, 2008). The orogenic edifice is overlain by two generations of piggyback basins (*sensu* Ori & Friend, 1984), or “satellite basins” (Ricci-Lucchi, 1986), genetically linked to the foreland -directed (i.e. towards East) migration of the deformation (Vitale & Ciarcia, 2013) : the oldest basins are Miocene in age and the youngest are Plio-Pleistocene. Integrated subsurface geophysical data from the oil industry acquired since the 1960s have led to the discovery of vast hydrocarbon reservoirs hosted within the buried Apulian carbonate strata related to large antiformal structures (Casero et al., 1991, 2004; Mazzoli et al. 2001, 2008, 2014; Candela et al. 2015). Despite these advances, sizeable gaps remain in seismic data covering this area and are completely lacking below the CAB. In these zones the subsurface structural interpretations are still poorly defined.

While there is a general agreement about the thrust-controlled development of the CAB during the early Pliocene, the role of Quaternary tectonics affecting the basin are rather ambiguous. Several authors have invoked opposing tectonic models to explain the basin’s position and relative orientation concerning the dominant regional structural fabric and the precise role of Pleistocene tectonics driving the basin fill history (Turco et al., 1990; Hyppolyte

et al. 1994; Amore et al. 1998, Bonini & Sani, 2000; Ascione et al., 2012; Mazzoli et al., 2012).

The goal of this work is to study the sedimentary facies of the syntectonic successions and intervening tectonic structures of the CAB, in order to characterize their spatio-temporal distribution, basin dynamics, and stress regime which during the Plio-Quaternary tectonic evolution of the Southern Apennine chain. Main aims of the work are to fill some of the knowledge gaps in the regional structural framework to provide crucial links from surficial outcrops to deeper structural motifs for reservoir individualization.

Regional Geologic Setting and Study Area

The Southern Apennines are a part of the Tertiary Alpine orogen which formed with in the general framework of the gradual collision between Africa and Europe (Shiner et al., 2004). NW-SE trending arc-shaped collisional orogenic belt consisting of mainly NE-verging thrusts developed since the Paleogene on an eastward-retreating, W-dipping subduction zone (Patacca et al. 1990; Doglioni et al. 1994; Cello & Mazzoli 1998, Patacca and Scandone, 1989; Malinverno and Ryan, 1986; Mostardini and Merlini, 1988; van Hinsbergen et al, 2014). In the southern sector, the Apennine chain is an orogenic wedge assembled as a thrust belt consisting of two structural levels. At the upper level are highly deformed rootless nappes of allochthonous units, or “thrust sheets” representing sediments deposited along the Neo-Tethys margin (e.g. Cello & Mazzoli,1998 Mazzoli and Helman, 1994; Stampfli and Borel, 2004; Handy et al., 2010) (Fig. 1). The allochthonous units are composed of deep marine units consisting of the Sicilide complex, in this area represented by the Argille Varicolori, and Liguride units, and carbonate deposits of the Apennine platform. Together these domains and areinterpreted as the record of an accretionary wedge related to the subduction of Neotethys oceanic crust during the Late Cretaceous-Paleogene (Vitale et al. 2011; Ciarcia et al. 2012). The lower structural level is characterized by highly allochthonous Mesozoic-Paleogene platform carbonates (Apennine Platform) and pelagic basin (Lagonegro) units tectonically overlying a buried, deep-seated (Apulian) carbonate inversion belt (Butler et al., 2004; Mazzoli et al., 2008; 2014). The detachment between the lower buried Apulian carbonates and the upper allochthon is marked by a mélange zone measuring several hundred meters to more than one km in thickness (Butler et al., 2004) (Fig 1b). In general, the southern portion

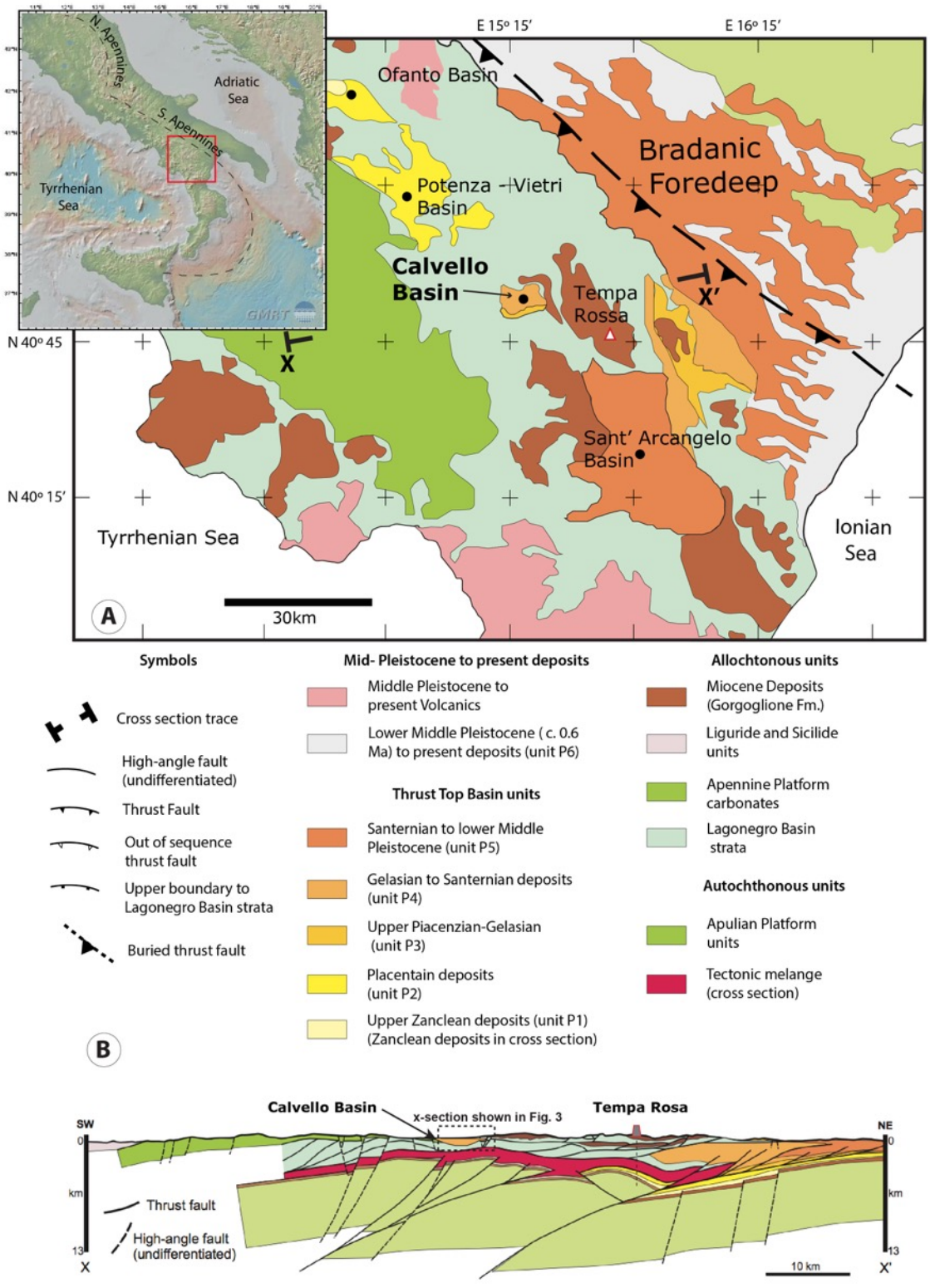

Figure 5.1 Geologic setting of the Southern Apennines showing the large-scale geologic overview of the Southern Apennines and generalized regional cross section. Modified from Ascione et al., 2012.

of the chain exhibits a polyphase tectonic history beginning during the Middle Miocene (Cello & Mazzoli, 1998) with a period of northeast-directed shortening, followed by a younger period of strike-slip- and extensional-dominated tectonics, characterized by the activation of NW-SE and NE-SW striking faults superimposed onto the previous shortening-related structures (Cello & Mazzoli, 1998; Butler et al. 2005). The switch from thin-skinned (or detachment dominated) to thick-skinned (or crustal-ramp dominated) thrusting, which occurred as the thick lithosphere of the Apulian Platform was involved in the deformation (Mazzoli et al., 2008), was in fact followed by a decay of crustal shortening during the Middle Pleistocene (e.g. Patacca and Scandone, 2001). Since then, NE-SW oriented horizontal extension became dominant over the entire orogen (e.g., Hippolyte et al., 1994). Extensional faults, mainly NW-SE trending, postdating and dissecting the thrust belt (e.g. Butler et al., 2004) are also responsible for the active tectonics and seismogenesis in the southern Apennines (e.g. Cello et al., 1982, 2000; Westaway, 1992; Chiarabba et al., 2005; Pondrelli et al., 2006; Maggi et al., 2009; Frepoli et al., 2011; Macchiavelli et al., 2012; Ascione et al., 2013; DISS Working Group, 2015).

Unconformably overlying the whole orogenic belt Upper Miocene and Plio-Quaternary siliciclastic successions have been recognized. These clastic packages bury the older and deeper structures of the thrust system (Ascione et al., 2012; Mazzoli et al., 2012). The earlier thrust top basin units are represented by the deep water turbidite succession, the Gorgoglione Flysch Formation (Boiano et al 1997; Pitts et al. 2017; Casciano et. al, 2018). Among the latter group, are several Plio-Quaternary wedge top sedimentary basins positioned on the frontal portion of the Apennine Allochthon. with a roughly E-W orientation, which is peculiarly transverse to the regional NW-SW-trending regional structural fabric of the southern Apennines.

These basins, including the Ofanto, Potenza, and Sant' Arcangelo basins have all been formerly interpreted as thrust top or piggyback basins (Hippolyte et al., 1994a; Pieri et al.,1994; Vezzani, 1967) (Fig. 1). The positions of these basins collectively follow a general linear trend along the NW-SE strike of the chain structure and their sedimentary infills become progressively younger towards the SE (Ascione et al., 2012). Their stratigraphic

arrangements follow a general pattern of deltaic and coastal gravels and sandstones, which pass upwards to shoreface deposits then to open-shelf clays (Ascione et al., 2012; Pepe & Gallicchio 2013). The stratigraphic architecture of these basins shows evidence of Neogene syn-sedimentary deformation and helps to better constrain the latest Quaternary tectonic stages of the Southern Apennines. (Cello et al., 2003; Tondi et al., 2005; Spina et al., 2008, 2011; Mazzoli et al., 2012).

Methods

Exposures of the CAB succession were documented using traditional geologic field mapping methods aided by the use of an Unmanned Aerial Vehicle (UAV) to fly aerial reconnaissance surveys to scout for previously unknown or otherwise inaccessible locations.

Field methods involved re-mapping at the 1:10,000 scale taking advantage of newly available 5-meter resolution DEM imagery provided by the Basilicata Region (https://rsdi.regione.basilicata.it/) Field surveys were used to identify appropriate exposures which warranted detailed outcrop studies focused on stratigraphic architecture and key structural features. Additionally, a suite of 5 samples were collected from three transects covering selected mudstone intervals for stratigraphic age-dating to calibrate field interpretations and to place lithologic units within the proper biostratigraphic framework. It is worth noting that, although the 2009 IUGS ratification places Pliocene-Pleistocene boundary at the base of the Gelasian (Gibbard et al., 2010), this work, in order to maintain consistency with previous authors, informally maintains the previous boundary at the top of the Gelasian.

The use of the UAV involved conducting aerial surveys at altitudes of 80-90 meters to broaden the field survey and to complement the field mapping (Fig 2a). Where appropriate, we also employed aerial Structure from Motion (SfM) photogrammetry methods to assess specific outcrops in 3D (Fig 2c). This work involved collecting large numbers of overlapping photos covering key outcrops to construct 3D, digital, virtual outcrop models (VOMs; Tavani et al. 2014; Corradetti et al. 2018) using Agisoft Photoscan Pro software, following the procedure outlined by Pitts et al. (2017) and Nesbit et al. (2018) (Fig. 2). Digital geologic interpretations and data extraction were made using the Virtual Reality Geologic Studio

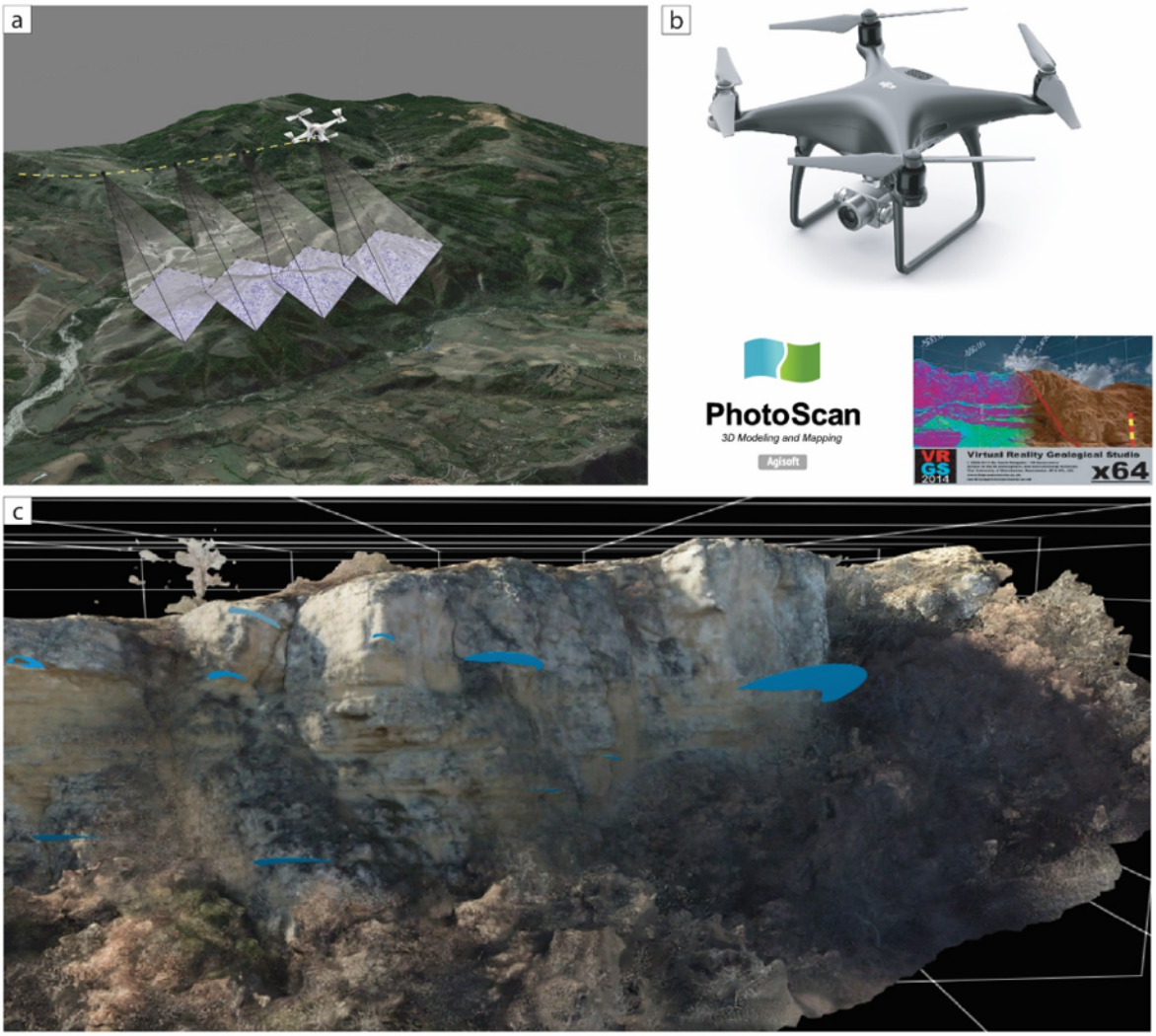

Figure 5.2. Methods involving the use of the Unmanned Aerial Vehicle survey and Digital Outcrop Model analysis. A) example of UAV flight pattern recording overlapping photosets. B) The DJI Phantom 4 quadcopter and the two software packages, Agisoft PhotoScan Virtual Reality Geologic Studio, used to process and analyze digital outcrop data. C) Example of one digital outcrop model created using Agisoft PhotoScan showing the VRGS software geologic analysis tool pack to measure strike and dip of cliff side exposures, blue disks represent the planar measurement tool.

software (VRGS). Using this tool, structural orientations of bedding were taken using a 3-point user-driven plane fit feature to measure inaccessible portions of outcrops. These data were then incorporated into the geologic map with other physically acquired data.

Basin Stratigraphy

The CAB succession is approximately 1000 meters thick and contains the record of three unconformity-bound sedimentary cycles which were deposited over a heavily deformed substrate and syndepositionally deformed. These units are recognized as the early middle

Pliocene Ponte Camastra Unit, the late Pliocene to early Pleistocene Fumara del Terra Unit, and the Pleistocene Monte Figarola Conglomerate (Bonini & Sani, 2000). In the following paragraphs, the results of our survey are presented in the form of a geologic map (Fig 3) and lithological descriptions and interpretations.

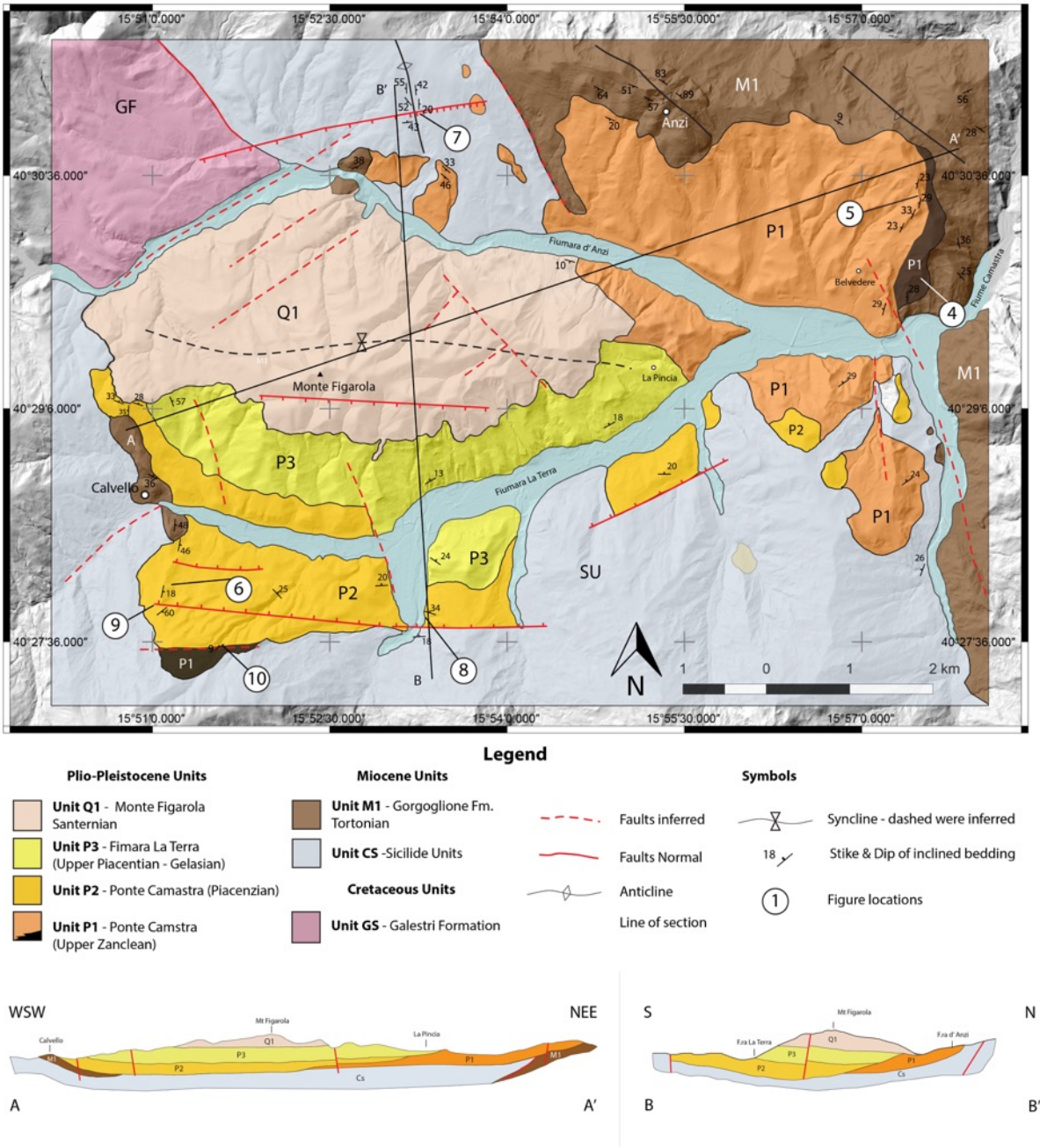

Figure 5.3. Compiled schematic geologic map of the Calvello Basin and underlying pre-Pliocene units. Mapping refined from di Donato (1995) and cross section modified after Bonini et al 2010.

The CAB Units range from the Zanclean stage of the early middle Pliocene to the upper middle Pleistocene (Ascione et al., 2012) (Fig.4). These units rest unconformably on top of the highly deformed “pre-Pliocene units” consisting of the Gorgoglione Formation, a 1500-meter thick succession of coarse-grained deepwater turbidites with both channelized and basin fan floor facies (Boiano et al 1997; Pitts et al. 2017; Casciano et. al, 2018) or the Upper Cretaceous-lower Miocene Varicolored Clays (“Argille Varicolori” of the Italian authors), a unit containing green to red and gray highly tectonized mudstones (Ogniben et al., 1969; Pescatore et al., 1988; Mattioni et al., 2006). The underlying pre-Pliocene Sicilide Units have been heavily deformed into predominately N-S, NW-SE, and NNW-SSE tight fold structures which are primarily seen outside the north and northeast sector of the CAB margin.

The CAB stratigraphic units were initially divided in various manners by previous authors first according to lithofacies designation (Amato & Cinque 1992), biostratigraphic dating (Di Donato, 1995), by the lithostratigraphic mappable units (Bonini & Sani, 2000), and according to sedimentary cycles (Ascione et al., 2012). Common among all these conventions is the recognition of three distinct unconformity-bound, packages of shallow marine to alluvial deposits. In this study, we adopt the stratigraphic scheme used by Bonini & Sani (2000) placed within reference to the sedimentary cycles described by Ascione et al. (2012). The following descriptions of stratigraphic units focus on sedimentary character, facies features, main architectural elements, and are followed by interpretations of depositional setting. This work pays attention to the stratigraphic units exposed at the basal and marginal zones of the basin which exhibit crucial syntectonic stratigraphic relationships holding the keys to interpreting the basin evolution.

Ponte Camastra Unit (P1 Cycle – Zanclean)

The Ponte Camastra Unit correlates to the P1 sedimentary cycle of Ascione et al. (2012) and is the oldest unit in the basin fill succession. This unit is exposed on the northeast basin margin and consists of two principal members; a lower predominantly coarse-grained interval, known as the Belvedere Conglomerate, and an upper unit of mixed silici-bioclastic arenites with intervals of siltstones and clays (Fig. 5).

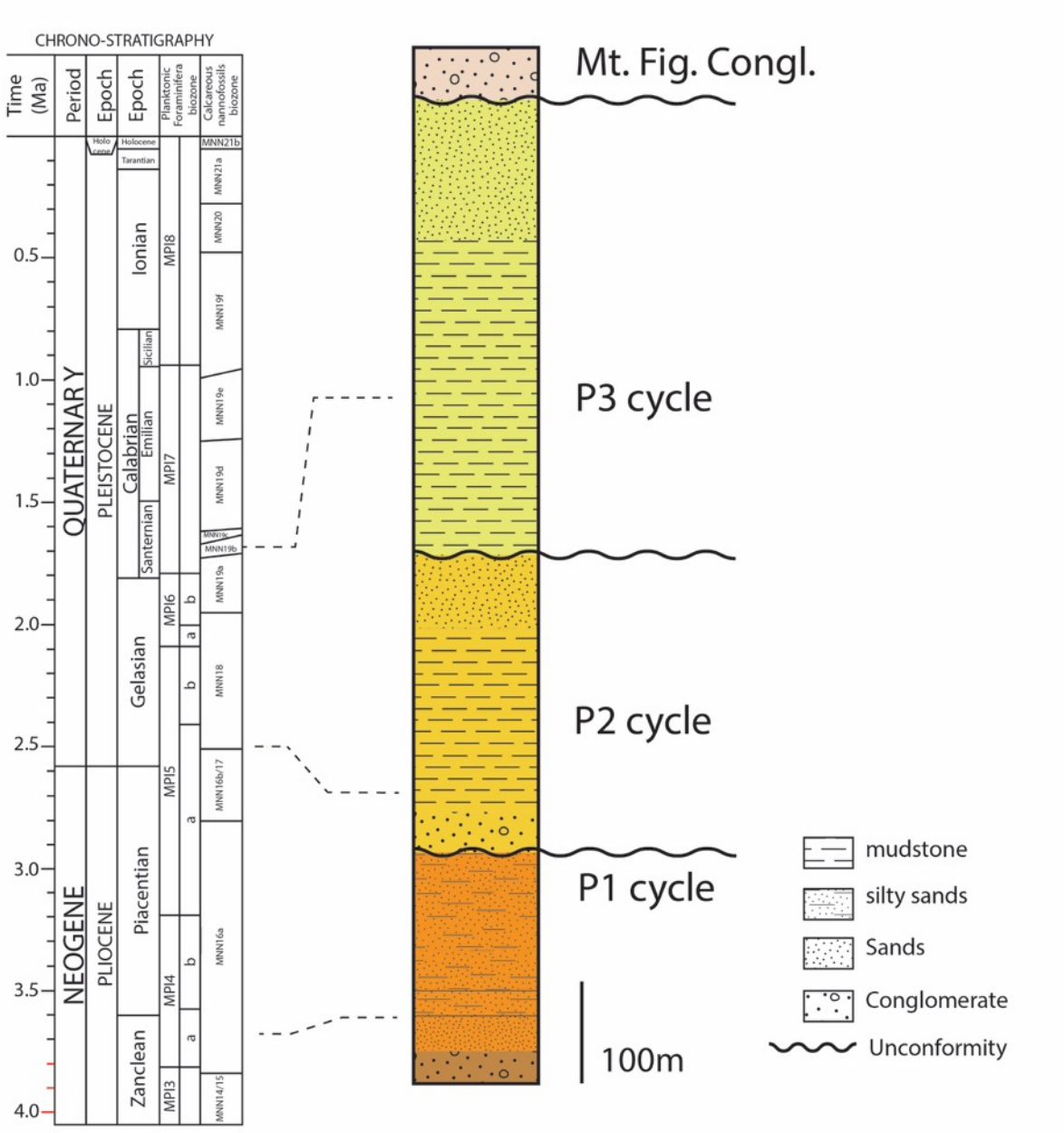

Figure 5.4. Calvello Basin generalized stratigraphic column and biostratigraphic framework. Column modified from Bonini and Sani 2001. Biostratigraphic framework compiled from Di Donato (1995) and Ascione et al. (2012)

P1 Belvedere Conglomerate Description:

At the base of the Ponte Camastra unit is the Belvedere Conglomerate member which is mainly found forming the steep slopes on the western walls of the Camastra River valley on the NE basin margin (Fig 3 & 5). Other exposures are found in just one location at the SW margin along one roadcut (Fig. 3). Resting unconformably over the folded middle Miocene

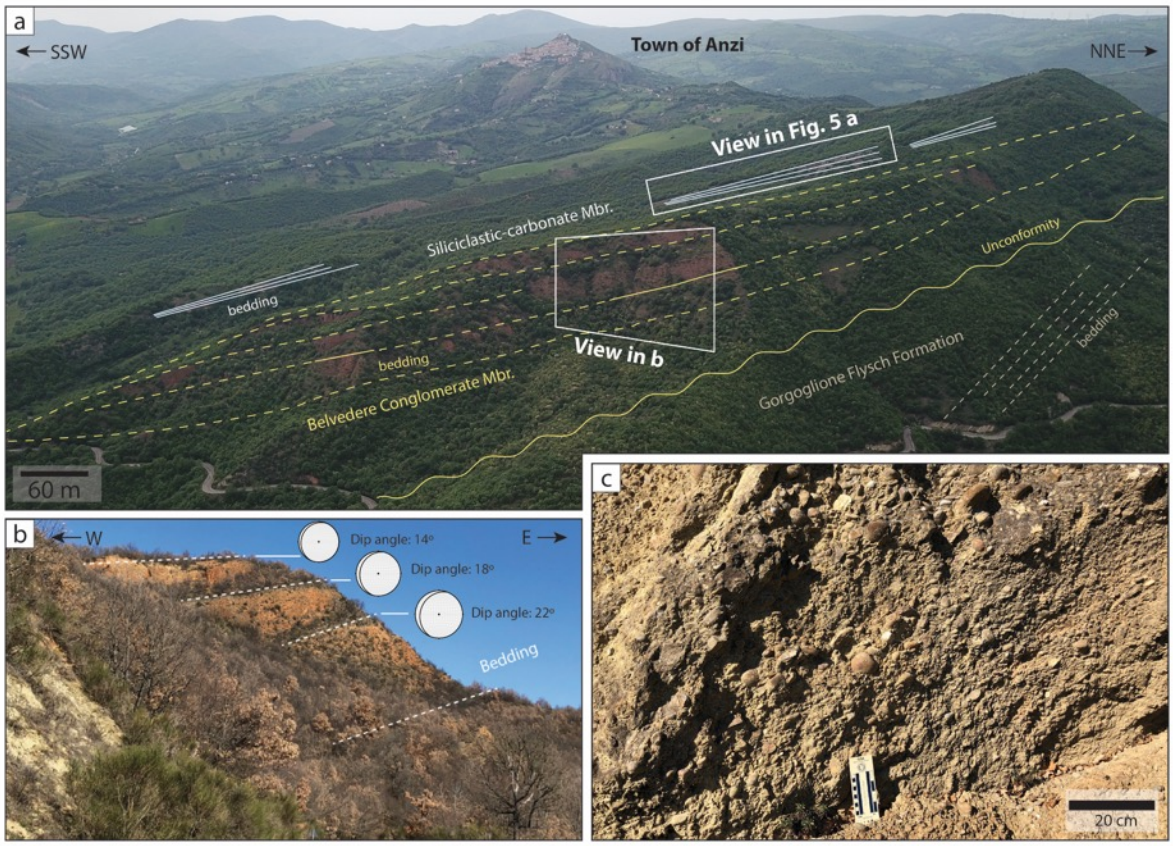

Figure 5.5. *Belvedere area on the northeastern basin margin of the showing the basal Calvello units of the Ponte Camastra Unit. A) Aerial photo showing the lenticular bedding packages of the Belvedere Conglomerate member resting unconformably over the Gorgoglione Flysh Formation. B) Northeast facing view of the Belvedere Conglomerte and the progressive unconformity shown by the gradual upward decreasing of bedding attitude. C) Outcrop view of the Belvedere Conglomerate member. Card for scale shows centimeter increments of the left side.*

Gorgoglione Flysch Formation, the Belvedere is primarily a brick-red to red-brown chaotically sorted conglomerate with minor intervals of decimeter thick sand beds and sandstone and siltstones with interbedded pebble conglomerates (Fig. 5, b & c). Compositionally, this unit is made of well-rounded clasts of marly grey and greenish limestones, arkosic arenites, grey calcarenites, cherty limestones, and crystalline clasts ranging from 1 - 50 cm in diameter set in a dark red silty to medium-grained, moderately well-sorted sandstone matrix. The internal organization is quite chaotic and shows a lack of well-developed individual beds or other primary sedimentary structures. However, the large-scale architecture shows a lenticular body of conglomerate with a total thickness approximately 70 meters. The larger body can be individuated into smaller bedset packages which are recognized by distinct changes in the slope caused by bench-forming surfaces. Each bedset package measures approximately 15-20 m and gradually thin-out laterally. Outcrop data extracted remotely using the SfM-

produced digital outcrop model permitted the measurement of broad-scale stratal geometry and structural attitude of the large bedset surfaces, confirming the presupposed notion that these bedset packages dip SSW with bedding attitude in the lower bed sets dipping 24 degrees and shallowing upwards reaching an angle of 15 degrees. On the SW basin margin, the Belvedere Conglomerate unit is exposed along a road-cut which shows the coarse-grained conglomerates filling a channelform two meters thick and 20-30 m wide with an erosional base overlying medium bedded packages of siltstone and mudstones with horizons of aligned pebbles.

P1 Belvedere Conglomerate Interpretation

The composition, sedimentary character, and overall stratal geometry, and relationship to channelized deposits suggest that the Belvedere Conglomerate was deposited by an alluvial fan system. These interpretations are following those of Bonini & Sani (2000) and correspond to reported fluvial-alluvial fan deposits during the early Pliocene throughout the thrust-top basins (Casciello et al., 2013; Ascione et al., 2012). The variety and range of textural maturity of clasts indicate that the provenance source area for this conglomerate covered a wide area to include both locally sourced limestones as well as long-traveled crystalline clasts, sourced from the Calabrian Arc (Critelli and Le Pera, 1994). The general lack of significant internal bedform structures and overall crudely organized sedimentary fabric suggests that these were the result of alluvial-fed debris flows (Nemec & Steel, 1984).

Three-dimensional virtual outcrop models created for the Belvedere Conglomerate outcrops in this portion of the study area revealed the presence of a series of intraformational progressive unconformities expressed by the gradual upward decrease in the structural attitude of bed-set packages. An apparent progressive unconformity was noted by previous authors (Bonini & Sani, 2000). However, using the VRGS plane-fit structural analysis tool inside the VOM confirmed the upward decrease in dip attitude from 24 degrees to 15 degrees from the base to the top of the unit (Fig 3 b). This phenomenon is attributed to the emergence of a positive tectonic structure, such as a thrust of a flower structure, striking roughly N-S to NNW-SSE, which deformed the eastern basin margin gradually decreasing accommodation space suggesting that the Belvedere Conglomerate underwent significant synsedimentary deformation. This type of tectonic driven unconformity is reported in other settings describing

syntectonic alluvial fan deposits along the Catalonian south Pyrenees (Riba, 1976), the Ebro Basin margin in the Pyrenees Mountains of NE Spain (Anadon et al., 1986; Lawton et al., 1999) And by Butler and Lickorish (2007) in southern Sicily. Furthermore, similar stratigraphic architecture has also been reported locally in Plio-Pleistocene strata of the neighboring Sant' Arcangelo Basin (Benvenuti et al. 2006). The conglomerates found on the SW margin of the CAV are here interpreted as correlative with the Belvedere basal conglomerate however representing a proximal portion of the fluvial/alluvial system. This channelized portion operated as part of the feeder system supplying coarse-grained material to the downstream alluvial fan complex deposited on the northwestern basin margin. The sandstones and siltstones with interbedded pebble conglomerate beds found under the channelform are interpreted as genetical related to the conglomerates which formed as floodplain deposits in the fluvial overbank environment.

P1 Ponte Camastra mixed siliciclastic-carbonate member description

Directly above and interfingering laterally with the Belvedere Conglomerate are the deposits of the Ponte Camastra mixed siliciclastic-carbonate member. This unit is formed by four facies associations: i) clinostratified silici-bioclastic arenites, ii) poorly sorted clast supported conglomerates, iii) plane parallel bedded siltstones and sandstones, and iv) medium bedded clayey siltstones. The overall thickness of this member is ~140 m with the entirety of the Ponte Camastra unit measuring 200 m.

Conglomerates are found near the base of this unit as discontinuous beds with limited lateral continuity of up to 10 m and measuring 3-5 m thick containing well-rounded pebble to cobble-sized clasts set in a fine to medium-grained matrix with erosive base in some cases filling minor channel-forms. Conglomerates grade upwards into silty sandstone beds with some intervals of aligned disaggregated fossil debris and intervals of medium-bedded siltstones and claystones. In the northeastern portion of the basin, minor cliff-forming outcrops of this unit are found in 3 N- to NNE-trending ridges which stand proudly in the topography and are easily identified in the 5 m resolution DEM imagery. UAV aerial imagery from the proper perspective and VOM reconstructions reveal the structure of these ridges as almost entirely formed of large-scale W to SW-dipping cross-beds or clinoform wedge-shaped bodies which pinch out in the S- to SSW-direction (Fig. 6 a). These wedges occur as three distinct packages which

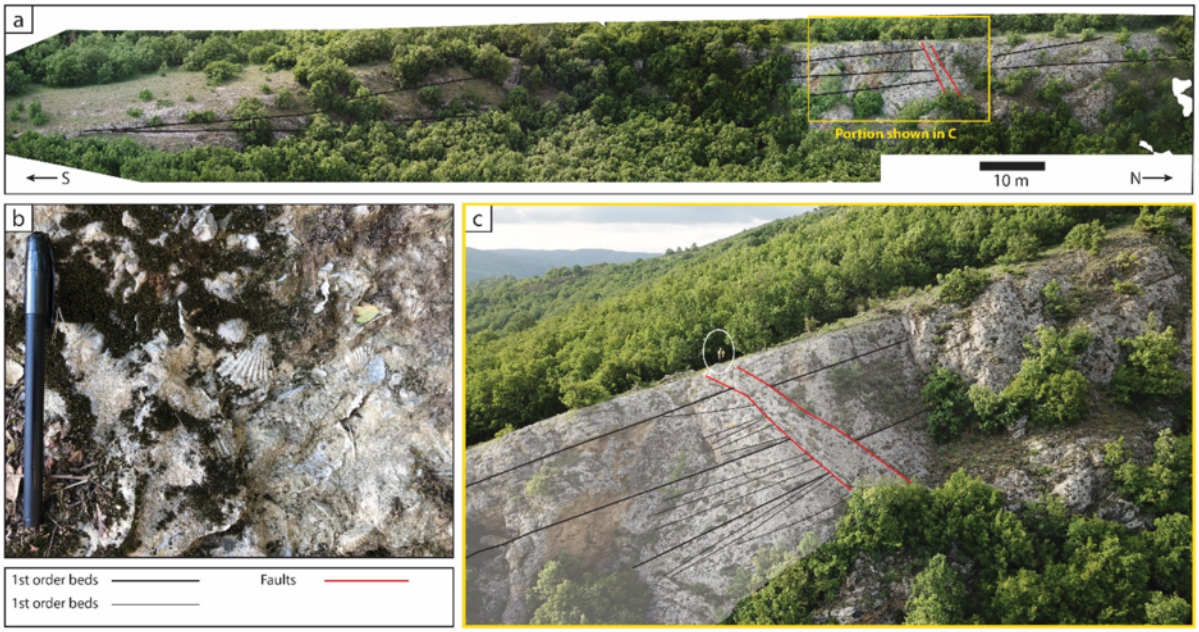

Figure 5.6. P1 Calcarenite Clinoform wedge details. A) Photogrammetry derived orthomosaic photo showing the large scale features of the middle and best exposed clinoform body. B) Outcrop detail showing the presence of a large amount of disarticulated bivalve shells. C) Details of the clinoform wedge internal arrangment showing 2nd order surfaces downlapping onto, and toelapping against 1st order surfaces which gradually wedge out to the south. Person for scale circled

are organized into a north-stepping vertical stack. Compositionally, these wedges contain mixed siliciclastic and carbonate grainstones, with much of the carbonate material contribution consisting of disarticulated bivalve shells, bryozoans, and foraminifera (Fig. 6 b). Each of the three identified wedges is 60-80 meters long and 20-30 m thick.

The internal organization of these wedges shows single bedding divisions ranging from 30-55 cm, which are mostly of bi-directional cross stratified beds (Fig 6 c). These packages show an internal hierarchy of first- and second-order stratal surfaces. In this case, second-order surfaces downlap onto first order surfaces and first-order surfaces pinch gradually towards the SW. These three primary wedges eventually pass upwards across covered intervals into siltstone beds mentioned above. Where exposed, the base of the wedges contains a 2-3-m thick package of thinly-bedded planar-laminated fine sand and siltstones beds organized into 5-10-cm beds. Biostratigraphic data collected for this interval agrees with that of Di Donato (1995) finding the presence of *Globorotalia punticulata*, placing this unit in the in the upper Zanclean (zone MPl4).

P1 Ponte Camastra mixed siliciclastic-carbonate interpretation

Based on the sedimentary character, stratigraphic architecture and stratal geometry, we interpret these beds as representing subaqueous deltas (Patruno & Helland Hansen, 2018) where wave and storm-action were the primary agents of sedimentary transport. Although the transition between the underlying conglomerates and the upper mixed siliciclastic-carbonate deposits is mostly covered, we interpret the base of this unit as a regional drowning unconformity (Godet, 2013; Schlager, 1989)of the underlying alluvial fan complex engulfing the proximal to terrigenous areas associated with the alluvial fan complex, forming a marine embayment. This flooding of basal conglomerates is recorded in nearly all the thrust-top basins during the Early Pliocene (Casciello et al. 2013) indicating a relative sea-level rise (Ciarcia et al. 2003; Palladino 2011). Other examples of eustatic signals recorded by the flooding of basal conglomerate during the early Pliocene are reported by Zecchin et al. (2012; 2013, and 2013b) in the Crotone Basin.

Calcarenite wedge bodies are formed as shoreline-parallel basinward-dipping clinoforms. Wedges of this nature have been described from Plio-Pleistocene systems in Italy as well as submerged coastlines of modern systems around the Mediterranean. Modern examples include those documented by Hernandez-Molina et al. (2000) along the southern coast of Spain described as the Infra-littoral prograding wedge. Ancient examples from the Plio-Pleistocene systems include those described by Massari et al. (2006, 2012) and Butler et al. (1998) and in the Mt Capodarso Formation on Sicily and those described by Pomar & Tropeano (2001) in the Calcarenite di Gravina Formation near Matera. Often, such as in the case of the Mt. Capodarso Formation, these wedges are interpreted as forming along a tectonically controlled high-gradient seafloor. Mixed siliciclastic-carbonate wedges have also very recently been described in syntectonic deposits of a similar age and nearby location by Chiarella et al., (2018) who evoked a “ridge and swale” topography due to contemporaneous thrust activity controlling depositional patterns. We interpret the wedges exposed in the CAB as having formed along similar thrust, thrust of a flower structure-related seafloor ridges that formed as back-thrusts associated to the NE directed thrust structures which characterized the Zanclean tectonic regime of the Southern Apennines during the early compressional phase of the CAB.

P2 Ponte Camastra Unit description

This member is stratigraphically above the P1 deposits with primary exposures at the southeastern margin of the basin where these units are found in contact with the Argile Varicolori units and along the southern banks of the Fiumara La Terra River. This unit contains two principle facies associations, from the base they are: i) mixed silici-bioclastic conglomerates and gravelly calcarenites; ii) fine-medium bedded calcarenites and silty mudstones. At the base is an interval of mixed siliciclastic and gravelly calcarenites (Fig. 7b). This interval is characterized by thin to medium thick beds ranging from 10-15 cm made of medium- to coarse-grained material with a substantial contribution of crushed and disarticulated shell material of bivalve pectens. Some have pebbly bases consisting of well-rounded pebble to granule size clasts while others are entirely made of gravels (Fig. 7 b). These pebbly beds show erosive bases and grade upwards into beds with coarse shell material. The upper interval of this unit is formed by medium to thin bedded bioturbated calcarenites which pass upwards to silty mudstones. These mudstones, which form well-developed badlands, contain several intervals of siltstones marked by sharp-based beds with abundant of fossil debris material. Resampling for biostratigraphic analysis from the mudstone dominate facies confirms the findings by Di Donato (1995) noting the presence of *Bulminia basispinosa*, placing this unit in the Piacenzian-Gelasian (zone MPI5).

P2 Ponte Camastra Unit interpretation

The sedimentary facies present in this units indicate a deepening trend of the basin and record the passage from nearshore to an offshore marine environment. Moving upwards, the P2 unit grades into deeper and finer grained deposits which eventually pass into marine siltstones indicating an offshore transition depositional zone.

The location of the P2 unit on the far western side of the basin from the P1 deposits indicates a westward drift of the active depocenter during the upper middle Pliocene. This change in depositional trend reveals a basin-filling motif which shifted from east to west. Additionally, the P2 deposits have a dissimilar distribution from the underlying P1 deposits, oriented as an E-W elongated ellipsoid. Our tectonic depositional model attributes the migration of the primary depocenter to the SW as indicating a transition from the NE-directed thrust propagation that dominated the P1 depositional regime.

Figure 5.7. P2 Cycle of the Ponte Camastra Unit and Belvedere Conglomerate on the western edge of the Calvello Basin. A) P1 Belvedere Conglomerate member of the Ponte Camastra Unit showing medium bedded fine-grained siltstone beds which are cut by a large channel form surface which is filled with chaotically bedded gravels. B) Lower middle section of the P2 cycle showing medium bedded normally graded gravely beds with bioclastic material and fining and thinning upwards sequences (indicated by triangles). C) Middle lower portion showing thin to medium bedded calcarenite deposits with a 1.5-meter Jacobs staff with 10 cm increments for scale.

P3 Fiumara La Terra Unit description

The Fiumara La Terra Unit is found in outcrop along the northern banks of the Fiumara La Terra river forming the lower slopes of the Monte Figarola to the east of the town of Calvello. This unit consists of fairly monotonous bluish grey to dark grey mudstone reaching a total thickness of approximately 150 meters. Unit P3 is very poorly stratified however in some cases finely laminated mudstone can be distinguished containing minor silty intercalations. Fossil fauna include microfossils, such as foraminifera, and macrofossils, such as gastropods, and in rare cases of 3-cm thick silty intervals and crushed shell debris (Fig 8c). Where discernable, bedding is shown as dipping northwards(Fig 8b). In the upper portions, this unit grades into sandy deposits with some pebbles before giving way to an erosional surface which forms the base of the overlaying Monte Figarola Conglomerate. Exposures of this unit form well-developed badlands (Fig 8a) on the southern flank of Monte Figarola.

Biostratigraphic ages from this study find the presence of microfossils including *Globorotalia infilata* conforming with previous findings by Di Donato (1995) placing this unit in upper Gelasian stage of the Pliocene.

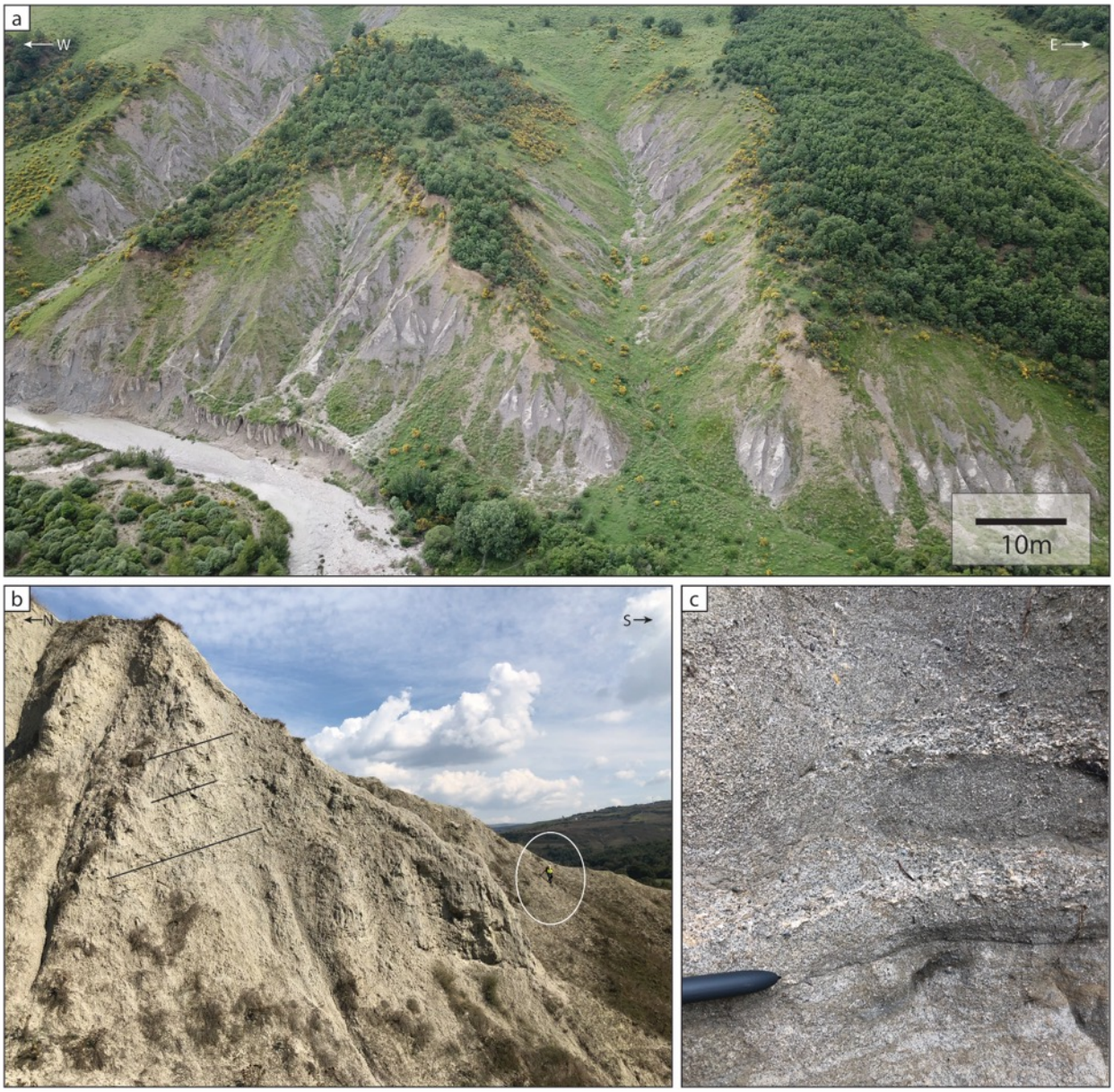

Figure 5.8. *Unit P3. A) Aerial View of unit P3 along the northern bank of the Fiumara la Terra River east of the town of Calvello, showing badland forming mudstone prone unit. B) Faint northward dipping bedding shown in black lines, person for scale. C) Thin beds of macrofossil shell debris indicating bedding planes. Pen for scale 5 mm width.*

P3 Fiumara la Terra Unit Interpretation

The composition, microfossil content and fined-grained nature of this unit reflect deposition in an offshore marine zone in a low-energy environment where hemipelagic clays settled from

suspension. Silty intervals with crushed shell debris indicate storm deposits which mobilized coarser, near shore material deposited deeper in the basin. The onset of this unit represents a flooding event which drowned the underlying regressive deposits at the top of the P2 sedimentary cycle. The distribution of this unit in map indicates both a basinward shift in the main depocenter with the mudstones forming a roughly east-west oriented ellipsoid. The orientation of this unit in map pattern suggest a depocenter that occupied an E-W elongated trough and indicates a transition from the placement of the earlier P1 deposits.

Monte Figarola Conglomerate Description

The Monte Figarola Unit is found along the central portion of the basin forming the peak and upper slopes of the small mountain for which it is named (Fig. 2). This unit is the uppermost member of the CAB fill and is approximately 250 m thick occupying elevations of ~815m to ~1070m. This unit consists of red to brown-red poorly consolidated conglomerate. In the few visible exposures, this conglomerate is made of well-rounded, poorly sorted, and otherwise chaotically organized conglomerates containing clasts ranging in diameter from 1-20 centimeters with rare blocks up to 30 centimeters. Compositionally this unit is made of clasts of grey to dark grey calcarenties, white and grey chert, grey limestones, micaceous sandstones and with a sandy yellow matrix. This unit shows no distinct bedding or internal stratigraphic architecture. Since this unit is so poorly exposed throughout the mapping area, its individuation is based mainly on elevation and the distinction of topographic character from the underlying mudstone prone interval. In few locations where the base of this unit is discernable along the northern slopes of the Fiumara La Terra river, it lies unconformably over Unit P1, P2, and P3 units along a nearly horizontal erosional surface. In this unit is included several small tongues of polygenic reddish-brown conglomerates on the lower slopes of Monte Figarola which are associated with abandoned fluvial terraces. These patches of conglomerates show the same compositional makeup as the larger Monte Figarola Conglomerate, however are found

Monte Figarola Conglomerate Interpretation

Based on the composition, clast size distribution, chaotic organization, and general lack of internal sedimentary structures , this unit is interpreted as an alluvial succession. These deposits are here interpreted as the final filling stage of the CAB. The contact between the Monte Figarola Conglomerates and the underlying units found along a nearly horizontal

regressive surface which represents a depositional unconformity. The Monte Figarola conglomerate has a large vertical thickness with respect to its horizontal extent of just ~14 km^2. Due to this fact this unit suggests the presence of a large amount of accommodation space created during the final filling stage of the CAB evolution which hosting the deposition of this unit. The overall geometry of these deposits in map pattern measure just under 7 km in the E-W direction and ~2.5 km in the N-S direction. The distribution of this unit forms an E-W elongated ellipsoid, outlining a similar shape as the distribution of the underlying P3 units.

Synsedimentary Structural Framework

Along the northern margin of the basin, mapping efforts have recognized an E-W trending fault zone characterized by a main near vertical south to southeast-dipping outcropping fault which dissects the N-S oriented pre-Pliocene fold structures seen in the substrate units (Fig. 9).

This fault zone shows a clear main fault plane with normal to oblique slip kinematic indicators and an associated damage zone 10s of meters wide with several associated minor faults (Fig 9b). Previous workers have documented cases of basin-bounding extensional structures along the northern margins in several other wedge-top basins including the Ariano, Ofanto, and Sant' Arcangelo basins (Mazzoli et al. 2012). The presence of synsedimentary south-southeast-dipping extensional faults as a common feature in several of the Plio-Pleistocene basins suggests a a regional phenomenon.

Defining the southern margin of the CAB are a series of roughly E-W and ESE-WNW trending extensional faults which place the P2 units in tectonic contact with the Argille Varicolori units (Fig. 10). The precise nature of this contact is difficult to measure directly due to poor exposure. However, sandy intervals set in P2 mudstones within 100 m of this contact show clear signs of normal faulting (Fig. 10 a,b,c). Here a zone measuring up to 30-m from the contact is characterized by at least three extensional faults with meter-scale offset. Additionally, this fault zone can be traced along strike westward for ~7km where it intersects rock outcrops of P2 deposits which sit unconformably on the substrate (Fig. 11 & 12). At this western edge of the fault zone, several faults were mapped and measured in an area

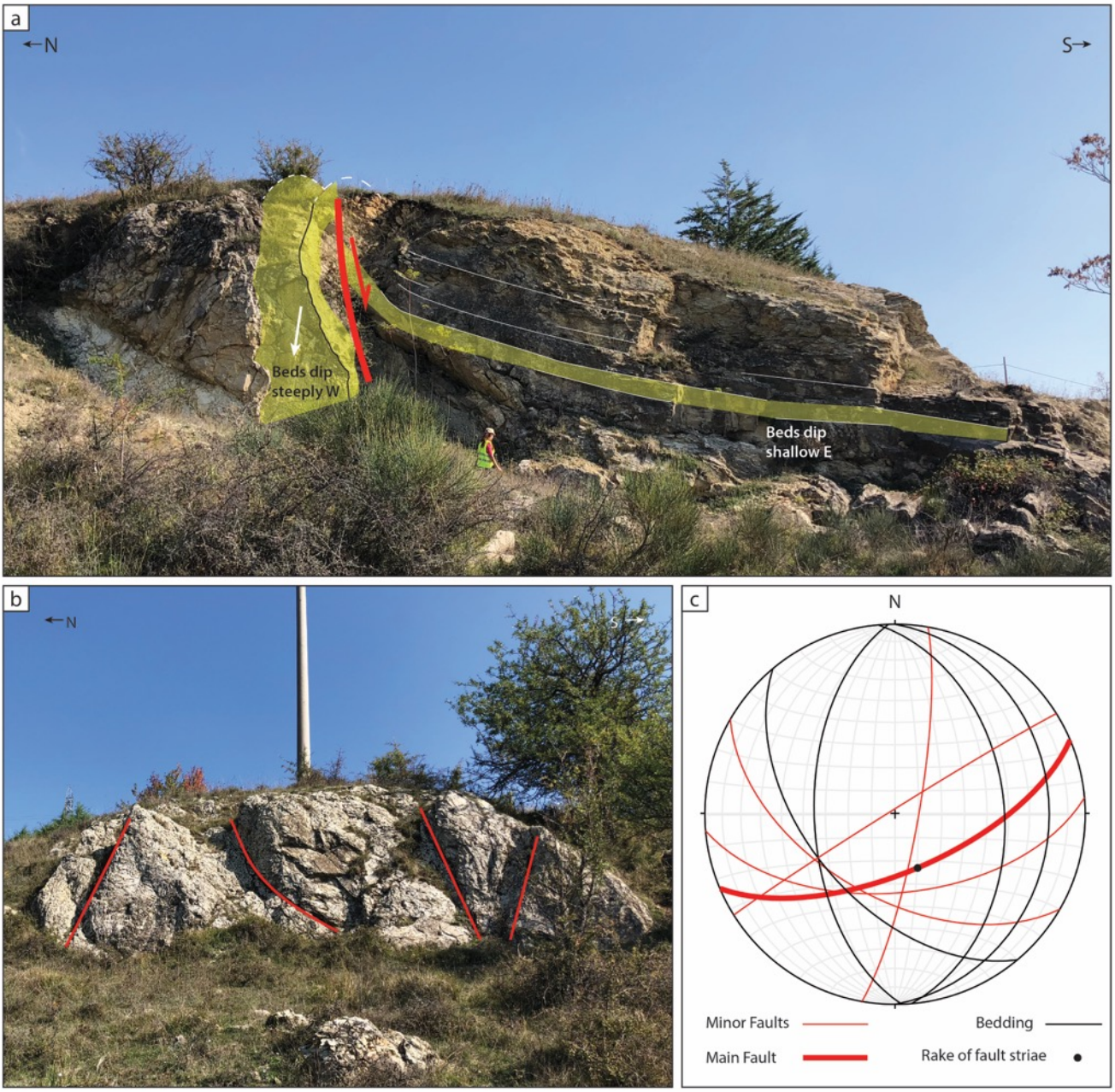

Figure 5.9. Structural details at the northen Calvello Basin margin. A) Outcrop showing normal fault dissecting folded Sicilide units. B) One example of several N to NE dipping faults with normal offset seen along siltstone beds within the mudstone interval of the P2 sedimentary cycle units. C) Stereographic projection of structural data showing the orientation of 6 measured faults wulf lower hemisphere

characterized by a 10-20m zone with six measured faults showing a strong preference towards extensional kinematics with centimeter to decimeter offset (Fig. 11 & 12).

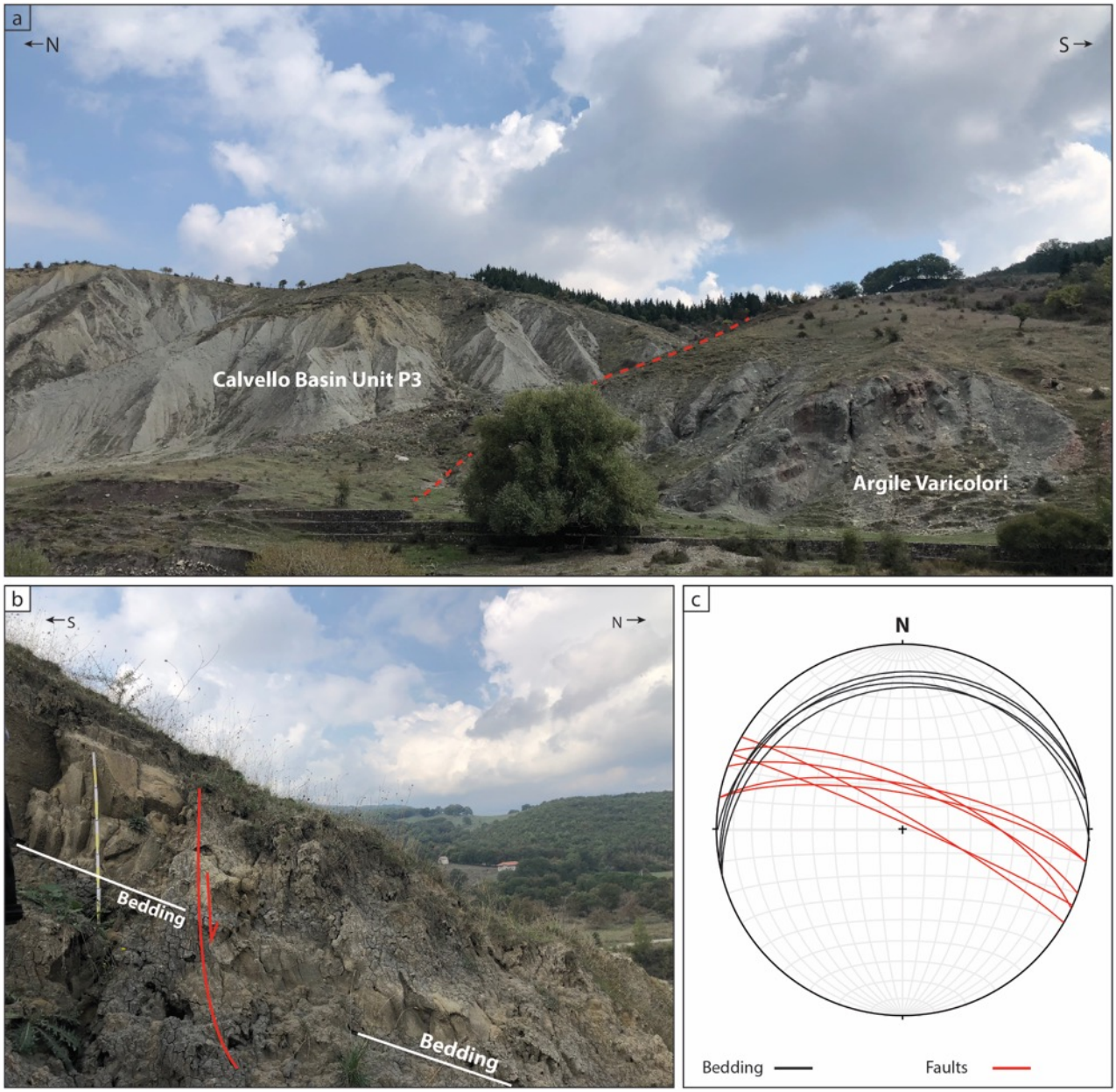

Figure 5.10. *Structural details at the southern Calvello Basin margin. A) Overview of area showing the Pliocene units along a tectonic contact with the Miocene Argille Varicolori. B) One example of several N to NE dipping faults with normal offset seen along siltstone beds within the mudstone interval of the P2 sedimentary cycle units. C) Stereographic projection of structural data showing the orientation of 6 measured faults (in red) compared to bedding (shown in black) wulf lower hemisphere.*

Discussion

In this study, focused on the analysis of the sedimentological characteristics, stratigraphic architecture, and intervening structures of the syntectonic succession, we present a depositional model for the CAB which relates the deposition of shallow marine sediments to the activity of both compressional and extensional structures.

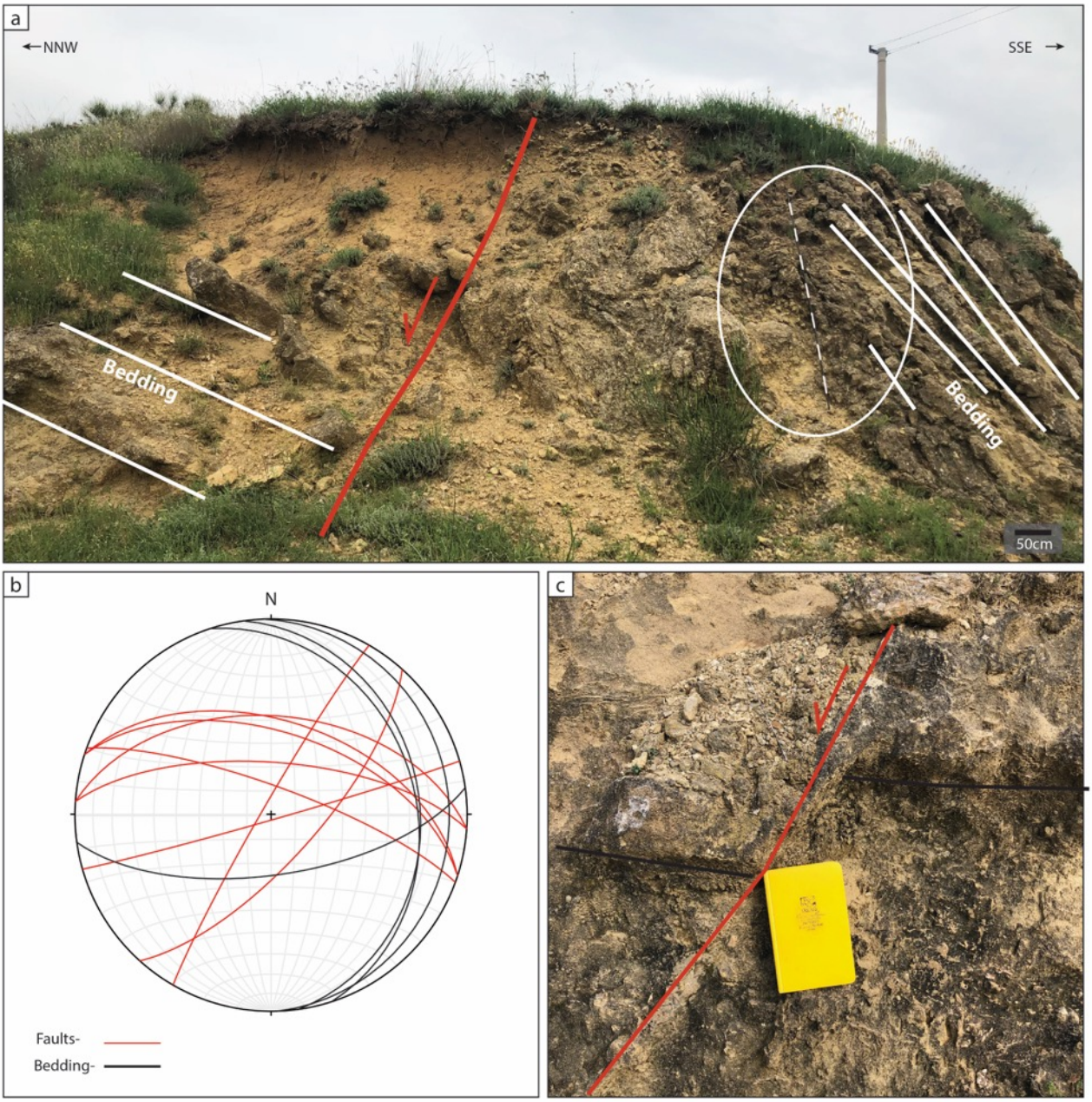

Figure 5.11. Structural details along the southern basin margin. A) large fault which is partially obscured due to poor exposure along master fault plane. B) Structural data of local subsidiary faults and bedding showing opposing dip directions on either side of the interpreted fault. C) Detail view of one of several associated faults showing normal displacement of ~15 cms.

The CAB developed through two main depositional stages which are directly linked to the two established tectonic phases affecting this sector of the Apennine chain. During the first phase, initial development of the CAB as a wedge-top basin began under the general crustal shortening regime that characterized the early middle Pliocene in the Southern Apennine chain. Later, during the second phase, in the late Pliocene to early-middle Pleistocene, the

CAB evolution was controlled by localized along-strike crustal extension. This change in tectonic style in the CAB corresponds to other findings in the Southern Apennine piggyback basins as documented by Hippolyte et al. (1994).

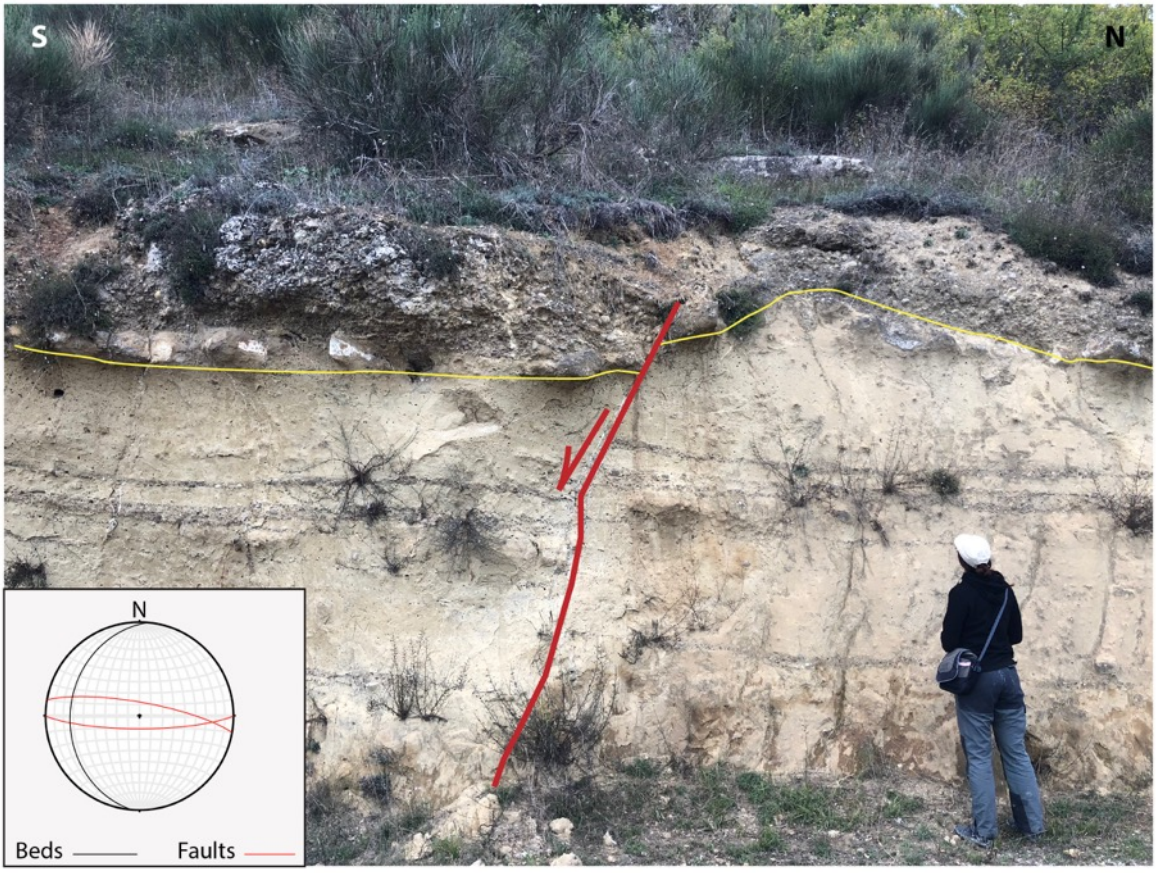

Figure 5.12. *Structural details along the southwest basin margin of a northward dipping normal fault dissecting the channel fill and associated fine grained deposits of unit P1.*

Evidence of Thrust-driven Syn-tectonic Deposition

We present several points of evidence suggesting the basin was affected by NE-SW and NNE-SSW oriented shortenig during the early middle Pliocene. We interpret this as the dominant factor controlling the deposition of the P1 unit. We suggest that the growth of NW-SE-trending thrust structures controlled both the seafloor topography and the style of deposition occurring during the early middle Pliocene. These structures involved a combination of both west- and east-verging thrust structures operating synchronously during the wedge-top phase of the CAB. Evidence of the sedimentary system's response to this thrust activity is marked in the oldest deposits of the CAB, by the intraformational progressive unconformity surfaces in the Belvedere conglomerate member. We interpret this as

documenting the role of tectonic uplift in controlling accommodation space at the depocenter of the alluvial fan system which accumulated at the early basin margin (Fig. 12). The presence of the mixed siliciclastic-carbonate wedges in the calcarenite member of the Ponte Camastra unit, as well as the southwestward migration of the primary depocenter from P1 to P2 units supports the notion of the development of a deep-seated positive tectonic structure.

We interpret the Ponte Camastra clinoform mixed siliciclastic-carbonate wedges as forming along a roughly southwest propagating margin with a dramatic seafloor topography linked to active tectonic uplift of the eastern basin margin. We attribute the formation of these wedges to the growth of a structural relief associated with the primary northeast verging thrust system as for the syntectonic growth wedge of the Belvedere conglomerate.

In this sense, the inferred active positive tectonic structure could potentially be associated with an east-dipping, west-verging back thrust, or a blind thrust anticline. This interpretation is similar to models by previous authors regarding the tectono-stratigraphic development of the Sant' Arcangelo Basin, a slightly younger Plio-Pleistocene wedge-top basin (Calabro et al. 2002, Benvenuti et al. 2006). Previous authors envisioned a similar tectonostratigraphic model, indicating that basin deposition was controlled by the presence of both east- and west-verging thrusts. The westward migration of back-thrusts is favored here as a plausible mechanism controlling the westward drift of the basin depocenter of the P1-P2 sedimentary cycle units.

The third point of evidence is the shape and orientation of the early middle Pliocene P1 deposits in map pattern. This early-stage CAB is elongated in a NW-SE orientation, consistent with the Pliocene shortening tectonic regime suggesting that the P1 deposits formed in a basin distinct from the subsequent depositional basin of the P2 an P3 units. The footprint of this early stage basin has a much different orientation than the current apparent basin orientation which is roughly east-west.

Evidence of Quaternary Basin extension

Field analysis reveals the presence of two roughly E-W striking corridors along the northern and southern margins of the basin which exhibit evidence of normal faulting. The occurrence

of these fault zones indicates the transition during the late Pliocene and early Pleistocene to an extensional/transtensional tectonic regime which dissected the Miocene structural fabric and controlled depositional focus and accommodation space in the CAB during the final phase of basin infill.

On the northern side of the basin, E-W oriented structures do not directly interact with the Plio-Pleistocene units; however, they show a cross-cutting relationship with N-S trending Miocene-Pliocene, tight map-scale folds (Fig 9). The width of the damage zone associated with this fault suggests that it could be a basin scale structure partially responsible for upper Pleistocene depositional changes.

On the southern margin of the basin, we document three occurrences of field evidence indicating post-depositional, N-S oriented basin extension which deforms upper middle Pliocene P2 units along a ~3 km long zone consisting of at least three similarly oriented normal fault segments. The width of this extensional zone measures 2 km and involves a major fault defining the southern basin boundary as well as two lower-order structures deforming upper middle Pliocene deposits.

We look to these structures as potentially controlling the depocenter and map-view footprint of the early Pleistocene units which give the CAB the appearance of an E-W orientation. The orientations of these structures, which are nearly normal to the predominant Pre-Pliocene structural fabric, can explain a large amount of accommodation space created to allow the deposition of the 250 m of the Monte Figarola Conglomerate.

Relationships with regional Apennine structures and preexisting tectonic models

The CAB evolution is placed within the general framework of the Southern Apennine structural setting where there is a well-established strong predominance of NW-SE striking, NE-verging thrusts. According to most interpretations, NE-directed thrusting in the Apennines and coeval SE-ward motion of Calabria resulted from the retreat of the composite Adriatic-Ionian slab (Malinverno & Ryan, 1986; Royden *et al.*, 1987; Patacca et al. 1990; Pierantoni et al., 2019) within the general framework of NW-ward subduction beneath the Calabrian Arc. These processes were accompanied by coeval back-arc extension in the Tyrrhenian Sea

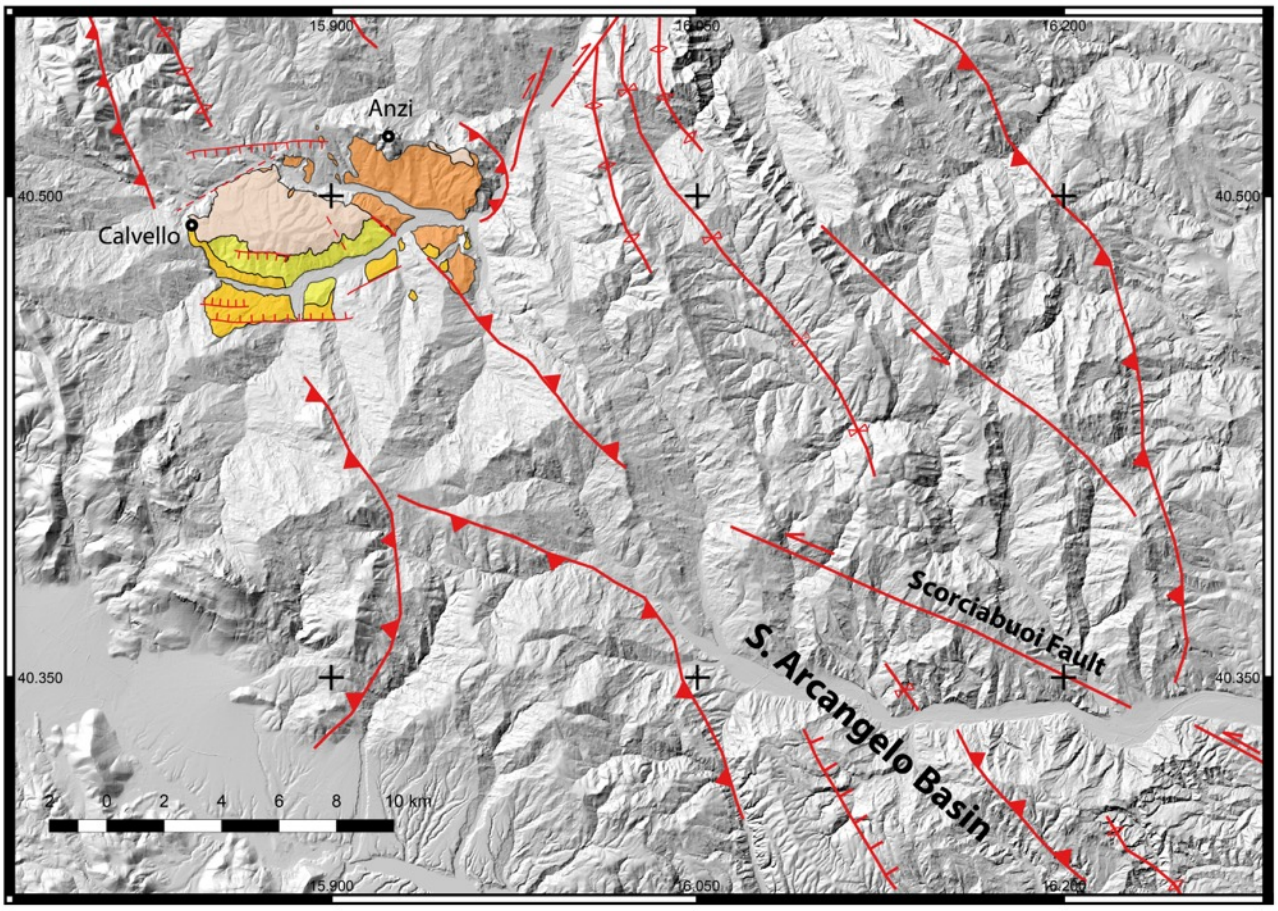

Figure 5.13. Sketch geologic map of the Calvello basin placed within the greater regional structural setting an the hillshade DEM map. Faults and interpretations after (Benvenuti et al. 2006).

(Kastens *et al.*, 1988; Sartori 2003) and by strike-slip motion along NW to WNW striking wrench faults (sinistral in the Southern Apennines and dextral in northern Sicily; Knott & Turco 1991) accommodating the SE-ward motion of Calabria. These strike-slip faults undoubtedly played a major role in the tectonic evolution of southern Italy, resulting in the development of a peculiar, wrench-dominated back-arc region in the southern Tyrrhenian Sea. However, the role of strike-slip tectonics in the formation of the wedge-top basins of the Southern Apennines, including the CAB of this study, is more ambitious (Fig. 13).

Previous authors have invoked three contrasting tectonic models to explain the role of Quaternary tectonics in the southernmost Plio-Pliestocene thrust-top basins of the southern Apennines (Potenza, CAB, Sant Arcangelo Basin); here we consider these three models with respect to our data:

1) The CAB was formed as a releasing bend at the tip of a large NW-SE left lateral fault zone (Catalano et al., 2003).
2) The CAB formed within the framework of a NE-SW, striking, oblique-slip (right lateral and reverse) fault running parallel to the Camastra river (Bonini & Sani 2000).
3) The CAB was affected by extension along the strike of the Apennine chain (Mazzoli et al. 2012), a process that was related to a migrating lithospheric tear in the subducting slab by Ascione et al. (2012).

Considering the first case, recent mapping and structural analysis of the largest NW-SE Scorciabuoi Fault (SF) by Caputo et al. 2008 with respect to our data we find this type of structure incompatible with the CAB for several reasons. Firstly, the surface expression of the SF disappears at the nearly 15 km south of the Calvello Basin and does not appear to physically intersect the CAB units, or the E-W trending basin bounding structures along the southern CAB margin described in this work. Additionally, projecting the trace of the SF along strike until intersection with the CAB would place the basin in a position geometrically incompatible with an extensional release along a left-lateral strike slip fault. Considering these points, we find no evidence linking either the syntectonic stratigraphic architecture or mapped structural features to the evolution of the CAB with the Quaternary development of the SF.

In the second case, while our data do not explicitly rule out the occurrence of the deep-seated transpressional shear zone hypothesized by Bonini & Sani (2000), we cannot draw a clear connection between our mapping of the CAB and the presence of a NE-SW oriented shear zone that is hypothesized at depth but has no geological evidence at the surface.

Our data, revealing late-stage N-S to NW-SE directed extension along the strike of the Apennine chain, are in good agreement with the interpretation proposed by Ascione et al. (2012). These authors related along-strike extension to the SE-ward migration of a lithospheric tear in the subducting slab. This latter process is in fact envisaged to produce a subsidence-uplift wave moving along the strike of the thrust belt (Wortel & Spakman 2000). Such a wave would be accompanied by normal faults striking perpendicular to the chain axis, with associated basins showing an elongated shape roughly normal to the strike of the thrust belt (as indeed is the case for the late-stage CAB depocenter).

However, the results of the present work suggest a more complex tectonic evolution with respect to that envisaged by Mazzoli et al. (2012) for the CAB. This basin appears in fact to have developed in a first stage as a classic piggy-back basin elongated parallel to the strike of the thrust belt. Syn-depositional shortening during this first phase of basin formation was then followed by along-strike extension (possibly associated with slab tear migration at depth), with the development of a different, roughly E-W to ENE-WSW elongated, younger depocenter. It is worth noting that the latter extension is not in contrast with the well-known major strike-slip faulting in the Southern Apennines (e.g. Knott & Turco 1991; Spina et al. 2011). In fact, large left-lateral motions along NW-SE lineaments have been associated with geodynamic processes involving the whole subducting slab, with the development of a lithospheric tear in the downgoing plate (Chiarabba et al., 2008). Further mild shortening of the basin infill, suggested by the analysis of the anisotropy of the magnetic susceptibility from the upper clayey part of the Gelasian–Santernian succession (Mazzoli et al. 2012), did not result in prominent outcrop-scale structural features.

Conclusion

This study presents new data on exposures, and an updated facies analysis that have improved the interpretations of depositional settings and their relationships with the poly-phase tectonic development of the CAB.

Using new perspectives gained through the aid of recently acquired aerial UAV data, we have documented the presence of key syntectonic stratigraphic architecture pointing towards synsedimentary Pliocene shortening. The clinoform wedge deposits documented here are outcrop elements that were until now totally unnoticed, or only hypothesized by previous field surveys and outside the range of recognition from available ground perspectives.

The two-phase tectonic model we propose explains the generation of the synorogenic basin fill as well as the overall characteristics of the basin's position and orientation with respect to the overall Apennine structural trend. The first phase shows syndepositional deformation of the basal CAB units attributed to NE-directed Apennine shortening during the early to middle Pliocene. This interpretation is supported by intraformational unconformities as well as the presence of tectonically- driven near shore clinoform wedges. This interpretation is further

supported by the trace in map pattern of the Pliocene CAB depocenter, which is roughly elongated parallel to the strike of the Apennine chain. The Pliocene stratigraphic units are offset by approximately E-W trending extensional structures and are overlain by sediments whose depositional focus migrated SE and rotated to fill an E-W to ENE-WSW oriented depression. We attribute these features as pointing towards the transition from horizontal shortening to extensional tectonics characterized by stretching along the strike of the Apennine chain. In turn, zipper-like propagation of the slab tear is accompanied by a subsidence/uplift wave and normal faulting associated with stretching along the strike of the mountain chain. These results point out that the development of accommodation space on top of Apennine chain and the formation of basins elongated perpendicular to the strike of the chain is controlled by is controlled bythis latter stretching, rather than extension at releasing bends/stepovers of NW striking wrench faults.

These new data and basin evolution model regarding this rather small thrust top depocenter helps to improve the picture of the Quaternary tectonics affecting this sector of the Apennine chain and the mechanisms controlling the development of the Plio-Quaternary thrust top basins. The insights in this work help to further characterize the importance and relative role of compressional, strike-slip, and extensional tectonics in terms of sedimentary basin development but also in terms of the geodynamic settings which surround it. This work also provides clues into the subsurface structural arrangement in a part of the Apennines that is very poorly defined by subsurface seismic data. This improved view of the local and regional structural framework can help to better define the characteristics of potential oil targets at depth, particularly concerning (e.g.) reservoir compartmentalization by faults of different age, occurrence and orientation of open fracture sets, and structural overprinting (including formation and possible dissection of structural traps). Therefore, these findings may bear important implications for the nearby Tempa Rossa oilfield and further exploration in adjacent zones of the southern Apennines.

Acknowledgments

This research was supported by the Reservoir Characterization Project (http://www.rechproject.com) at the University of Camerino, funded by Total Italia E&P. The Authors would like to thanks Andrea Artoni and two anonymous reviewers for the very thorough review which improved the manuscript greatly.

References

Amato, A., & Cinque, A. (1992). Il Bacino Plio-Pliestocenico di Calvello (Potenza): Evoluzione Geologica e Geomorfologica. Studi Geologici Camerti, 1, 181–189.

Amore, F.O., Basso, C., Ciampo, G., Ciarcia, S., Di Donato, V., Di Nocera, S., et al. 1998. Nuovi dati sul Pliocene tra il fiume Ufita ed il torrente Cervaro (Arianese, Baronia e Daunia meridionale). Bollettino della Società Geologica Italiana, 117: 455–466.

Anadon, P., Cabrera, L., Colombo, F., Marzo, M., & Riba, O. (1986). Syntectonic Intraformational Unconformities in Alluvial Fan Deposits, Eastern Ebro Basin Margins (NE Spain). Foreland Basins, (8), 259–271.

Ascione, A., Ciarcia, S., Di Donato, V., Mazzoli, S., & Vitale, S. (2012). The Pliocene-Quaternary wedge-top basins of southern Italy: An expression of propagating lateral slab tear beneath the Apennines. Basin Research, 24(4), 456–474.

Ascione, A., Mazzoli, S., Petrosino, P., and Valente, E., 2013, A decoupled kinematic model for active normal faults: Insights from the 1980, MS = 6.9 Irpinia earthquake, southern Italy: Geological Society of America Bulletin, v. 125, p. 1239–1259. doi:10.1130/B30814.1.

Benvenuti, M., Bonini, M., Moratti, G., & Sani, F. (2006). Tectonosedimentary evolution of the Plio-Pleistocene Sant'Arcangelo Basin (Southern Apennines, Italy). Geological Society, London, Special Publications, 262(1), 289–322.

Bonini, M., & Sani, F. (2000). Pliocene-Quaternary transpressional evolution of the Anzi-Calvello and Northern S. Arcangelo basins (Basilicata, Southern Apennines, Italy) as a consequence of deep-seated fault reactivation. Marine and Petroleum Geology, 17(8), 909–927

Boiano, U. (1997) Anatomy of a siliciclastic turbidite basin: the Gorgoglione Flysch, Upper Miocene, southern Italy: physical stratigraphy, sedimentology and sequence- stratigraphic framework. Sed. Geol., 107, 231–262.

Butler, Grasso, Gardiner and Sedgeley, 1998. Depositional patterns and their tectonic controls within the Plio-Quaternary carbonate sands and muds of onshore and offshore SE Sicily (Italy). Marine and Petroleum Geology, 14 (7/8): 879-892.

Butler and Lickorish, 1997. Using high-resolution stratigraphy to date fol and thrust activity: examples from the neogene of south-central Sicily. JGS London, 154: 633-643.

Butler, Tavarnelli & Grasso, 2006. Structural inheritance in mountain blets: An Alpine-Apennine perpsective. Journal of Structural Geology, 28 (11): 1893-1908.

Butler et al., 2019. Syn-kinematic sedimentary systems as constraints on the structural response of thrust belts: re-examining the structural style of the Maghrebian thrust belt of Eastern Sicily. Ital. J. Geosci., Vol. 138 (2019), pp. 371-389, 13 Figs. (https://doi.org/10.3301/IJG.2019.11).

Butler R.W.H., Mazzoli S., Corrado S., De Donatis M., Di Bucci D., Gambini R., Naso G., Nicolai C., Scrocca D., Shiner P. and Zucconi V. 2004. Applying thick-skinned tectonic models to the Apennine thrust belt of Italy: Limitations and implications. In: Thrust Tectonics And Petroleum Systems (K. R. McClay, ed.), AAPG Memoir, 82, 647-667.

Critelli, S. and Le Pera, E. 1994. Detrital modes and Provenance of the Miocene sandstones and Modern sands of the Southern Apennines piggy-back basins (Italy). Journal of Sedimentary Petrology.

Casero, P., Roure, F., Endignoux, L., Moretti, I., Muller, C., Sage, L., Vially, R., 1988. Neogene geodynamic evolution of the Southern Apennines, Memorie della Società Geologica Italiana 41, 109-12

Casero, P., Roure, F., & Vially, R. (1991). Tectonic framework and petroleum potential of the southern Apennines. In A. M. Spencer (Ed.), Generation, accumulation, and production of Europe's hydrocarbons (Vol. 1) (pp. 381–387). Special Publication of the European Association of Petroleum Geoscientists.

Casero P. 2004. "Structural setting of petroleum exploration plays in Italy" Special Volume of the Italian Geologic Society for the IGC 32 Florence-2004 Società Geologica Italiana.

Catalano, S., Monaco, C., Tortorici, L., Paltrinieri, W., & Steel, N. (2004). Neogene-Quaternary tectonic evolution of the southern Apennines. *Tectonics*, *23*(2), n/a-n/a. Retrieved from http://doi.wiley.com/10.1029/2003TC001512

Calabro, R. A., L. Feltre, and C. R. Perotti (2002), Structural features of S. Arcangelo piggy-back basin (southern Apennines – Italy) from seismic data and analogue modeling, Boll. Soc. Geol. Ital., vol. spec. 1, 333–341.

Candela S., Mazzoli S., Megna A. and Santini S., 2015. Finite element modelling of stress field perturbations and interseismic crustal deformation in the Val d'Agri region, southern Apennines, Italy. Tectonophysics, 657, 245-259.

Casciano, C. I., Patacci, M., Longhitano, S. G., Tropeano, M., McCaffrey, W. D., & Di Celma, C. (2019). Multi-scale analysis of a migrating submarine channel system in a tectonically-confined basin: The Miocene Gorgoglione Flysch Formation, southern Italy. Sedimentology, 66(1), 205–240.

Casciello, E., Esestime, P., Cesarano, M., Pappone, G., Snidero, M., & Vergés, J. (2013). Lower plate geometry controlling the development of a thrust-top basin: the tectonosedimentary evolution of the Ofanto basin (Southern Apennines). Journal of the Geological Society, 170(1), 147–158.

Caputo, R., Salviulo, L., & Bianca, M. (2008). Late Quaternary activity of the Scorciabuoi Fault (southern Italy) as inferred from morphotectonic investigations and numerical modeling. Tectonics, 27, TC3004.

Cello, G., & Mazzoli, S. (1998). Apennine tectonics in southern Italy: A review. Journal of Geodynamics, 27(2), 191–211.

Cello, G., Guerra, I., Tortorici, L., Turco, E., and Scarpa, R., 1982, Geometry of the neotectonic stress field in southern Italy: Geological and seismological evidence: Journal of Structural Geology, v. 4, p. 385–393, doi:10.1016/0191-8141(82)90030-X.

Cello, G., Gambini, R., Mazzoli, S., Read, A., Tondi, E., and Zucconi, V., 2000, Fault zone characteristics and scaling properties of the Val d'Agri Fault system (southern Apennines, Italy): Journal of Geodynamics, v. 29, p. 293–307, doi:10.1016/S0264-3707(99)00043-5.

Cello, G., Tondi, E., Micarelli, L., & Mattioni, L. (2003). Active tectonics and earthquake sources in the epicentral area of the 1857 Basilicata earthquake (southern Italy). Journal of Geodynamics, 36(1–2), 37–50.

Chiarabba, C., Jovane, L., and Di Stefano, R., 2005, A new view of Italian seismicity using 20 years of instrumental recordings: Tectonophysics, v. 395, p. 251 - 268.

Chiarabba, C., De Gori, P., Speranza, F. 2008. The southern Tyrrhenian subduction zone: Deep geometry, magmatism and Plio-Pleistocene evolution. EPSL 268, 408-423.

Chiarella, D., Longhitano, S. G., & Tropeano, M. (2019). Different stacking patterns along an active fold-and-thrust belt—Acerenza Bay, Southern Apennines (Italy). Geology, 47(2), 139–142.

Ciarcia, S., Di Nocera, S., Matano, F. & Torre, M. 2003. Evoluzione tettono- sedimentaria e paleogeografia dei depocentri «wedge-top» nell'ambito del «foreland basin system» pliocenico dell'Appennino meridionale (settore Irpino–Dauno). Bollettino della Società Geologica Italiana, 122, 117–137.

Ciarcia S., Mazzoli S., Vitale S. and Zattin M. 2012. On the tectonic evolution of the Ligurian accretionary complex in southern Italy. Geological Society of America Bulletin, 123, 463-483.

Corradetti A., Tavani S., Parente M., Iannace A., Vinci F., Pirmez C., Torrieri S. and Mazzoli S., 2017. Distribution and arrest of vertical through-going joints in a seismic-scale carbonate platform exposure (Sorrento peninsula, Italy): insights from integrating field survey. Journal of Structural Geology, 108, 121-136.

DeCelles, P. G., & Giles, K. A. (1996). Foreland basin systems. Basin Research, 8(2), 105–123.

Di Donato, V. 1995. Evoluzione dei Bacini Plio-Pleistocenici Dell'Appennino Meridionale: Biostratigraphia del Depositi Affioranti Nei Dintorni Di Calvello (PZ). PhD Thesis. Universita degli Studi Di Napoli " Federico II" Dipartimento di Scienze Della Terra.

DISS Working Group, 2015, Database of Individual Seismogenic Sources (DISS), Version 3.2.0: A compilation of potential sources for earthquakes larger than M 5.5 in Italy and surrounding areas. http://diss.rm.ingv.it/diss/, © INGV 2015 - Istituto Nazionale di Geofisica e Vulcanologia - All rights reserved, doi:10.6092/INGV.IT-DISS3.2.0.

Doglioni, C. (1994). The Puglia uplift (SE Italy): An anomaly in the foreland of the Apenninic subduction due to bucking of a thick continental lithosphere. Tectonics, 13(5), 1309–1321.

Doglioni, C., Innocente, F., Morellato, C., Procaccianti, D., & Scrocca, D. (2004). On the Tyrrhenian Sea opening. Mem. Descr. Carta Geol. d'It. XLIV, 147-164.

Faccenna, C., T. W. Becker, F. P. Lucente, L. Jolivet, and F. Rossetti (2001), History of subduction and back-arc extension in the central Mediterranean, Geophys. J. Int., 145, 809–820

Ford, M., E. A. Williams, A. Artoni, J. Verge´s, and S. Hardy, 1997, Progressive evolution of a fault-related fold pair from growth strata geometries, Sant Llorenc¸ de Morunys, SE Pyrenees: Journal of Structural Geology, v.19, no. 3–4, p. 413–441

Frepoli, A., Maggi, C., Cimini, G.B., Marchetti, A., and Chiappini, M., 2011, Seismotectonic of Southern Apennines from recent passive seismic experiments: Journal of Geodynamics, v. 51, p. 110–124.

Gibbard, P. L., Head, M. J., Walker, M. J. C. and the Subcommission on Quaternary Stratigraphy. 2010. Formal ratification of the Quaternary System/Period and the Pleistocene Series/Epoch with a base at 2.58 Ma. J. Quaternary Sci., Vol. 25 pp. 96–102. ISSN 0267-8179.

Godet A. 2013 Drowning unconformities: Palaeoenvironmental significance and involvement of global processes. Sedimentary Geology, 293, pp. 45-66

Handy, M., S. M. Schmid, R. Bousquet, E. Kissling, and D. Bernoulli (2010), Reconciling plate-tectonic reconstructions of Alpine Tethys with the geological-geophysical record of spreading and subduction in the Alps, Earth Sci. Rev., 102, 121–158.

Hernández-Molina, F. J., Fernández-Salas, L. M., Lobo, F., Somoza, L., Díaz-del-Río, V., & Dias, J. M. A. (2000). The infralittoral prograding wedge: a new large-scale progradational sedimentary body in shallow marine environments. Geo-Marine Letters, 20(2), 109–117.

Hippolyte, J. C., Angelier, J., Roure, F., & Casero, P. (1994). Piggyback basin development and thrust belt evolution: structural and palaeostress analyses of Plio-Quaternary basins in the Southern Apennines. Journal of Structural Geology, 16(2), 159–173.

Improta, L. & Corciulo, M. (2006) Controlled source nonlinear tomography: A powerful tool to constrain tectonic models of the Southern Apennines orogenic wedge, Italy. Geology, 34, 941-944.

Jolivet, L., and C. Faccenna (2000), Mediterranean extension and the Africa-Eurasia collision, Tectonics, 19, 1095–1106

Kastens, K. A., et al. (1988) ODP Leg 107 in the Tyrrhenian Sea: Insight into passive margin and backarc basin evolution. GSA Bull., 100, 1140–1156.

Knott, S.D., Turco, E. 1991. Late Cenozoic kinematics of the Calabrian Arc, southern Italy. Tectonics 10, 1164-1172.

Lawton T. F., Roca E., Guimerà J. 1999. Kinematic-stratigraphic evolution of a growth syncline and its implications for tectonic development of the proximal foreland basin, southeastern Ebro basin, Catalunya, Spain. GSA Bulletin ; 111 (3): 412–431.

Lentini, F., Carbone, S., Di Stefano, A., & Guarnieri, P. (2002). Stratigraphical and structural constraints in the Lucanian Apennines (Southern Italy): Tools for reconstructing the geological evolution. Journal of Geodynamics, 34(1), 141–158.

Lickorish & Butler, 1996. Fold amplification and parasequence stacking patterns in syntectonic shoreface carbonates. GSA Bulletin; August 1996; v. 108; no. 8; p. 966-977; 10 figures.

Longhitano, S. G. (2008). Sedimentary facies and sequence stratigraphy of coarse-grained Gilbert-type deltas within the Pliocene thrust-top Potenza Basin (Southern Apennines, Italy). Sedimentary Geology, 210(3–4), 87–110.

Longhitano, S. G., Chiarella, D., Di Stefano, A., Messina, C., Sabato, L., & Tropeano, M. (2012). Tidal signatures in Neogene to Quaternary mixed deposits of southern Italy straits and bays. Sedimentary Geology, 279(November), 74–96.

Macchiavelli, C., Mazzoli, S., Megna, A., Saggese, F., Santini, S., and Vitale, S., 2012, Applying the Multiple Inverse Method to the analysis of earthquake focal mechanism data: new insights into the active stress field of Italy and surrounding regions: Tectonophysics, doi:10.1016/j.tecto.2012.09.007.

Maggi, C., Frepoli, A., Cimini, G.B., Console, R., and Chiappini, R., 2009, Recent seismicity and crustal stress field in the Lucanian Apennines and surrounding areas (Southern Italy): Seismotectonic implications: Tectonophysics, v. 463, p. 130–144.

Malinverno, A. & Ryan, W.B.F. (1986) Extension in the Tyrrhenian Sea and shortening in the Apennines as a result of arc migration driven by sinking of the lithosphere. Tectonics, 5, 227–245.

Massari, F., & D'alessandro, A. (2012). Facies Partitioning and Sequence Stratigraphy Of A Mixed Siliciclastic-carbonate Ramp Stack In The Gelasian Of Sicily (S Italy): A Potential Model For Icehouse, Distally-steepened Heterozoan Ramps. Rivista Italiana Di Paleontologia E Stratigrafia (Research In Paleontology And Stratigraphy), 118(3).

Massari, F., & Chiocci, F. (2006). Biocalcarenite and mixed cool-water prograding bodies of the Mediterranean Pliocene and Pleistocene: architecture, depositional setting and forcing factors. Geological Society, London, Special Publications, 255(1), 95–120.

Mattioni L., E. Tondi, P. Shiner, P. Renda, S. Vitale, G. Cello, 2006. The Argille Varicolori unit in Lucania (Italy): a record of tectonic offscraping and gravity sliding in the Mesozoic–Tertiary Lagonegro Basin, southern Apennines, Geological Society, London, Special Publications, 262(1):277.

Mazzoli S., Barkham S., Cello G., Gambini R., Mattioni L., Shiner P. and Tondi E. 2001. Reconstruction of continental margin architecture deformed by the contraction of the Lagonegro Basin, southern Apennines, Italy. Journal of the Geological Society, London, 158, 309-319.

Mazzoli, S., and Helman, M. 1994. Neogene patterns of relative plate motion for Africa–Europe: some implications for recent central Mediterranean tectonics. Geologische Rundschau, 83: 464–468.

Mazzoli, S., D'Errico, M., Aldega, L., Corrado, S., Invernizzi, C., Shiner, P., & Zattin, M. (2008). Tectonic burial and "young" (<10 Ma) exhumation in the southern Apennines fold-and-thrust belt (Italy). Geology, 36(3), 243–246.

Mazzoli, S., Mittiga, F., Ascione, A., Szaniawski, R., & Capalbo, A. (2012). Tectonic evolution of Pliocene–Pleistocene wedge-top basins of the southern Apennines: new constraints from magnetic fabric analysis. Canadian Journal of Earth Sciences, 49(3), 492–509.

Mazzoli S., Ascione A., Buscher J. T., Pignalosa A., Valente E. and Zattin M., 2014. Low-angle normal faulting and focused exhumation associated with late Pliocene change in tectonic style in the southern Apennines (Italy). Tectonics, *33*(9), 1802-1818.

Milia, A., M. M. Torrente, and P. Iannace (2017), Pliocene-Quaternary orogenic systems in Central Mediterranean: The Apulia-Southern Apennines-Tyrrhenian Sea example, Tectonics, 36, doi:10.1002/2017TC004571.

Mostardini, F., Merlini, S., 1988. Appennino centro-meridionale. Sezioni geologiche e proposta di modello strutturale. Memorie della Società Geologica Italiana 35 (1986), 177-202

Nemec, W., & Steel, R. J. (1984). Alluvial and coastal conglomerates: their significant features and some comments on gravelly mass-flow deposits. Canadian Society of Petroleum Geologists Memoir, 10(1984).

Nesbit, P. R., Durkin, P. R., Hugenholtz, C. H., Hubbard, S. M., & Kucharczyk, M. (2018). 3-D stratigraphic mapping using a digital outcrop model derived from UAV images and structure-from-motion photogrammetry, 14(6), 1–18.

Ogniben, L. 1969. Schema introduttivo alla geologiadel confine Calabro–Lucano. Memorie dellaSocieta` Geologica Italiana,8, 453–763.

Patacca, E., Scandone, P., 1989. Post-Tortonian mountain building in the Apennines. The role of the passive sinking of a relic lithospheric slab. In: The Lithosphere in Italy, Boriani, A., Bonafede, M., Piccardo, G.B., Vai, G.B. (Eds.), Atti dei Convegni Lincei 80, 157-176

Patacca, E., and Scandone, P., 2001, Late thrust propagation and sedimentary response in the thrust-belt—foredeep system of the Southern Apennines (Pliocene-Pleistocene), in: Vai, G.B., Martini, I.P. eds., Anatomy of an Orogen: The Apennines and Adjacent Mediterranean Basins. Springer Netherlands, p. 401–440.

Palladino, G. (2011). Tectonic and eustatic controls on Pliocene accommodation space along the front of the southern Apennine thrust-belt (Basilicata, southern Italy).

Patacca, E., Sartori, R., & Scandone, P. (1990). Tyrrhenian basin and Apenninc arcs: kinematic relations since Late Tortonian times. Mem. Soc. Geol. It, 45, 425–451.

Pieri, P., Sabato, L., Loiacono, F., & Marino, M. (1994). Il bacino di piggy- back di Sant'Arcangelo: evoluzione tettonico-sedimentaria. Bollettino Societa` Geologica Italiana, 113, 465–481.

Pomar, L., & Tropeano, M. (2000). The Calcarenite di Gravina Formation in Matera (southern Italy): New insights for coarse-grained, large-scale, cross-bedded bodies encased in offshore deposits. AAPG Bulletin, 85(4), 661–689

Pondrelli, S., Salimbeni, S., Ekström, G., Morelli, A., Gasperini, P., and Vannucci, G., 2006, The Italian CMT dataset from 1977 to the present: Physical Earth Planetary International, v. 159, no. 3–4, p. 286–303.

Pescatore, T. 1988. La sedimentazione miocenica nell'Appennino campano–lucano. Memorie della Societa` Geologica Italiana,**41**, 37–46.

Pepe, M., & Gallicchio, S. (2013). Shallow-marine systems in a wedge-top basin setting: An example from the middle-upper Pliocene deposits of the Southern Apennines mountain front (Basilicata region, South Italy). Italian Journal of Geosciences, 132(2), 304–320.

Pierantoni, P., Penza, G., Macchiavelli, C., Schettino, A., Turco, E. 2020. Kinematics of the Tyrrhenian-Apennine system and implications for the origin of the Campanian magmatism. In Vesuvius, Campi Flegrei, and Campanian Volcanism. Editors De Vivo, Belkin, Rolandi. Elsevier, Pages 33-56. doi.org/10.1016/B978-0-12-816454-9.00003-1.

Pitts, A. D., Casciano, C. I., Patacci, M., Longhitano, S. G., Di Celma, C., & McCaffrey, W. D. (2017). Integrating traditional field methods with emerging digital techniques for enhanced outcrop analysis of deep water channel-fill deposits. Marine and Petroleum Geology, 87.

Riba, O. (1976). Syntectonic unconformities of the Alto Cardener, Spanish Pyrenees: a genetic interpretation. Sedimentary Geology, 15(3), 213–233.

Royden, L., Patacca, E. & Scandone, P. (1987) Segmentation and configuration of subducted lithosphere in Italy: an important control on thrust-belt and foredeep-basin evolution. Geology, 15, 714–717.

Sartori, R. (2003) The Thyrrhenian backarc basin and subduction of the Ionian lithosphere. Episodes, 26, 217–221.

Schlager W. 1989 Drowning unconformities on carbonate platforms. In P.D. Crevello, J.L. Wilson, J.F. Sarg, J.F. Read (Eds.), Controls on Carbonate Platform and Basin Development, SEPM Special Publication, 44, SEPM, Tulsa, Oklahoma, U.S.A. (1989), pp. 15-25

Shiner, P., Beccacini, A., Mazzoli, S., (2004) Thin-skinned versus thick-skinned structural models for Apulian carbonate reservoirs: constraints from the Val d'Agri Fields, S Apennines, Italy, Marine and Petroleum Geology, 21(7), 805-827.Spina, V., Tondi, E., Galli, P., Mazzoli, S., & Cello, G. (2008). Quaternary fault segmentation and interaction in the epicentral area of the 1561 earthquake (Mw = 6.4), Vallo di Diano, southern Apennines, Italy. Tectonophysics, 453(1–4), 233–245.

Spina V., Tondi E., Mazzoli S. 2011. Complex basin development in a wrench-dominated back-arc area: tectonic evolution of the Crati Basin, Calabria, Italy. Journal of Geodynamics, Elsevier, 2011, 51 (2-3), pp.90.

Stampfli G.M., Borel G.D. (2004) The TRANSMED Transects in Space and Time: Constraints on the Paleotectonic Evolution of the Mediterranean Domain. In: Cavazza W., Roure F., Spakman W., Stampfli G.M., Ziegler P.A. (eds) The TRANSMED Atlas. The Mediterranean Region from Crust to Mantle. Springer, Berlin, Heidelberg

Steckler, M.S., Piana Agostinetti, N., Wilson, C.K., Roselli, P., Seeber, L., Amato, A. & Lerner-Lam A. (2008) Crustal structure in the Southern Apennines from teleseismic receiver functions. Geology, 36(2), 155–158.

Suppe, J., F. Sabat, J. A. Munoz, J. Poblet, E. Roca, and J. Verges, 1997, Bed-by-bed growth by kink-band migration: Sant Llorenc de Morunys, Eastern Pyrenees: Journal of Structural Geology, v. 19, p. 443–461

Tavani S., Granado P., Girundo M., Iannace A., Arbues P., Muñoz J.A. and Mazzoli S., 2014. Building a virtual outcrop, extracting geological information from it, and sharing the results in Google Earth via OpenPlot and Photoscan: An example from the Khaviz Anticline (Iran). Computers & Geosciences, 63, 44-53.

Tavani S., Storti F., Lacombe O., Corradetti A., Muñoz J.A. & Mazzoli S., 2015. A review of deformation pattern templates in foreland basin systems and fold-and-thrust belts: Implications for the state of stress in the frontal regions of thrust wedges. Earth-Science Reviews, 141, 82–104.

Tondi, E., Piccardi, L., Cacon, S., Kontny, B., & Cello, G. (2005). Structural and time constraints for dextral shear along the seismogenic Mattinata Fault (Gargano, southern Italy). Journal of Geodynamics, 40(2–3), 134–152.

Turco, E., Maresca, R., & Cappadona, P. (1990). La tettonica plio-pleisto- cenica del confine calabro-lucano: modello cinematico. Memorie Societa` Geologica Italiana, 45, 519–529.

van Hinsbergen, D. J. J., R. L. M. Vissers, and W. Spakman (2014), Origin and consequences of western Mediterranean subduction, rollback, and slab segmentation, Tectonics, 33, 393-419, doi:10.1002/tect.20125.

Vezzani, L., 1967. Il bacino plio-pleistocenico di S. Arcangelo (Lucania). Atti Accademia Gioenia Scienze Naturali Catania, S6, 18, Suppl. Sc. Geol. (pp. 207–227).

Vitale S., Ciarcia S., Mazzoli S. and Zaghloulb M.N. 2011. Tectonic evolution of the 'Liguride' accretionary wedge in the Cilento area, southern Italy: A record of early Apennine geodynamics. Journal of Geodynamics, 51, 25-36.

Vitale, S., & Ciarcia, S. (2013). Tectono-stratigraphic and kinematic evolution of the southern Apennines/ Calabria–Peloritani Terrane system (Italy). Tectonophysics, 583, 164–182.

Westaway, R., 1992, Seismic moment summation for historical earthquakes in Italy: tectonic implications: Journal of Geophysical Research, v. 97, p. 15437– 15464.

Wortel, M.J.R. & Spakman, W. 2000. Subduction and slab detachment in the Mediterranean-Carpathian region. Science, 290, 1910 – 1917.

Zecchin et al., 2012. The Plio-Pleistocene evolution of the Crotone Basin (southern Italy): Interplay between sedimentation, tectonics and eustasy in the frame of Calabrian Arc migration. Earth-Science Reviews 115 (2012) 273-303

Zecchin et al., 2013a. The Messinian succession of the Crotone Basin (southern Italy)I: Stratigraphic architecture reconstructed by seismic and well data. Marine and Petroleum Geology 48 (2013) 455-473

Zecchin et al., 2013b. The Messinian succession of the Crotone Basin (southern Italy) II: Facies architecture and stratal surfaces across the MioceneePliocene boundary. Marine and Petroleum Geology 48 (2013) 474-492.

Chapter

6

Analysis of fracture roughness control on permeability using SfM and fluid flow simulations: Implications for carbonate reservoir characterization

Hindawi
Geofluids
Volume 2019, Article ID 4132386, 19 pages
https://doi.org/10.1155/2019/4132386

Research Article

Analysis of Fracture Roughness Control on Permeability Using SfM and Fluid Flow Simulations: Implications for Carbonate Reservoir Characterization

Miller Zambrano,[1,2,3] **Alan D. Pitts**,[1,3] **Ali Salama**,[1] **Tiziano Volatili**,[1,2,3] **Maurizio Giorgioni**,[4] **and Emanuele Tondi**[1,2,3]

[1]*School of Science and Technology-Geology Division, University of Camerino, Italy*
[2]*GeoMORE s.r.l, Camerino, Italy*
[3]*Reservoir Characterization Project, Italy*
[4]*Shell Italia Exploration and Production, Italy*

Preface:

This chapter presents work from a recent publication in which Ph.D Candidate Pitts was the second author. This work integrates SfM scanning of fracture surfaces to better characterize surface roughness to provide a more quantitative approach to surface roughness measurements in a way that can be used for further studies in involving fluid flow simulations. PhD Candidate Pitts' specific contributions to this work were: 1) Participating in 2 field campaigns to assess the section and extract and collect suitable samples containing ideal fracture surfaces. 2) Preparing samples for 3D scanning. 3) Designing the SfM workflow in the laboratory conditions in order to process the samples. 4) Processing the samples using SfM procedures to render ultra-high-resolution 3D fracture surfaces. 5) Post-Processing of fracture surfaces including filtering, trimming, and scaling. 6) Directly involved with the drafting of the manuscript and figures for the published work.

Analysis of fracture roughness control on permeability using SfM and fluid flow simulations: Implications for carbonate reservoir characterization

Miller Zambrano [1, 2, 3], Alan Pitts [1, 3], Ali Salama [1], Tiziano Volatili [1, 2, 3], Maurizio Giorgioni [4], Emanuele Tondi [1, 2, 3]

1. School of Science and Technology - Geology Division, University of Camerino, Italy.

2. GeoMORE s.r.l, Camerino, Italy. (www.geomore.it)

3. Reservoir Characterization Project (www.rechproject.com)

4. Shell Italia Exploration and Production, Italy.

*Corresponding author: Miller Zambrano

Corresponding author main affiliation: School of Science and Technology - Geology Division, University of Camerino. Via Gentile III da Varano 7, 62032 Camerino, Italy. E-mail: miller.zambrano@unicam.it

Published in GEOFLUIDS

Abstract

Fluid flow through a single fracture is traditionally described by the cubic law, which is derived from the Navier-Stokes equation for the flow of an incompressible fluid between two smooth-parallel plates. Thus, the permeability of a single fracture depends only on the so-called hydraulic aperture which differs from the mechanical aperture (separation between the two fracture wall surfaces). This difference is mainly related to the roughness of the fracture walls, which has been evaluated in previous works by including a friction factor in the permeability equation or directly deriving the hydraulic aperture. However, these methodologies may lack adequate precision to provide valid results. This work presents a complete protocol for fracture surface mapping, roughness evaluation, fracture modeling, fluid flow simulation, and permeability estimation of individual fracture (open or sheared joint/pressure solution seam). The methodology includes laboratory-based high-resolution Structure from Motion (SfM) photogrammetry of fracture surfaces, Power Spectral Density (PSD) surface evaluation,

synthetic fracture modeling, and fluid flow simulation using the Lattice-Boltzmann method. This work evaluates the respective controls on permeability exerted by the fracture displacement (perpendicular and parallel to the fracture walls), surface roughness, and surface pair mismatch. The results may contribute to defining a more accurate equation of hydraulic aperture and permeability of single fractures, which represents a pillar for the modeling and upscaling of the hydraulic properties of a geofluid reservoir.

Keywords: *Joints, Pressure solution seems, Fracture permeability, Hydraulic aperture*

1. Introduction

Fractures exert a vital contribution on determining the migration and storage for geofluids, such as groundwater, and hydrocarbons. Thus, the analysis and modeling of fractures are imperative for characterizing reservoirs and simulating their behavior during the production stage. Fluid flow through fractures is traditionally described by the cubic law, derived from the Navier-Stokes equation for the flow of an incompressible fluid between two smooth-parallel plates [1]. Thus, the permeability (intrinsic permeability) of a single fracture may be represented by the equation:

$$k = \frac{e^2}{12} \quad , \qquad \text{(eq. 1)}$$

Where e corresponds to the hydraulic aperture. Since fractures are normally rough, the hydraulic aperture differs from the mechanical aperture (separation between the two fracture wall surfaces). The hydraulic aperture is in fact an equivalent value which can be derived from field analysis like tracer tests and hydraulic tests [2], and laboratory fluid flow experiments [*e.g.* 3].

Several authors have studied the effect of roughness of the walls on fracture permeability working with various materials, such as glass [4], rocks [5], and concrete [6]. These authors included a correction term, a so-called friction factor (f), on the permeability of rough fractures:

$$k = \frac{e^2}{12f} \quad , \qquad \text{(eq. 2)}$$

where the friction factor is defined by the common base equation:

$$f = \left[1 + c_1 \left(\frac{r_a}{2e}\right)^{c_2}\right] \quad , \qquad \text{(eq. 3)}$$

where, r_a is the difference between the highest peak and the lowest valley of the physical roughness, and both terms c_1 and c_2 are constants with slightly different values depending on the author. Thus, the friction factor depends only on the relative hydraulic roughness ($\frac{r_a}{2e}$) ignoring the frequency (or wavelength) of the asperities.

Another widely used methodology derives the hydraulic aperture from the mechanical aperture, E, and the joint roughness coefficient (JRC) as proposed by Barton *et al*. [7]:

$$e = \frac{E^2}{JRC^{2.5}} \quad , \qquad \text{(eq. 4)}$$

where the JRC is derived by comparing the fracture profile obtained with the Barton Comb with the standards tables provided by Barton & Choubey [8]. This methodology is perhaps the simplest and cheapest way to obtain fracture surface roughness values and has been widely used in outcrops studies [9-13]. The disadvantages of this method are related to the moderate resolution (about 1 mm) and the inaccuracy of the equation (4) at relatively wide apertures (with respect to the JRC value). For instance, considering a fracture with 100 μm mechanical aperture and a JRC equal to 2, the equation (4) gives a hydraulic aperture equal to 1767 μm.

Considering the previous arguments, the main objective of this work is to find empirical equations that describe the effect of fracture roughness on permeability at different apertures. In order to reach this goal, some problems which should be overcome are: i) to develop a protocol for mapping the fracture surface, ii) to evaluate the fracture roughness as a function of

the wavelength of the asperities, iii) to validate the relationships using a significant number of samples, roughness values and aperture scenarios.

Various approaches have been reported in the literature for mapping the surface of fractures and faults in the field or laboratory involving the use of Lidar [14, 15], laboratory profilometers [16-18], and SfM photogrammetry [*e.g.,* 12, 19]. Corradetti *et al.* [19] applied SfM photogrammetry for mapping fracture surfaces obtaining 3D reconstructions with point-cloud densities of equal quality to Lidar-derived data. Among these methods, SfM photogrammetry shows great promise as it is inexpensive (photo-camera and processing software) and extremely flexible regarding the scales and conditions (applicable in the field and laboratory). For example, SfM photogrammetry has been successfully used as an analytical tool to gather geologic data from outcrop studies [20-23], as well as at smaller scales on fault surfaces [19] and fossilized human footprints [24].

Evaluation of fracture roughness is achieved by implementing the Power Spectral Density (PSD), which provides a more objective description based on the frequency distribution of the asperities in the Fourier domain. This approach has been successfully applied by previous authors for describing the roughness of fractures [*e.g.,* 25] and fault surfaces [14, 15, 18, 19]. To increase the statistical significance of the results, approximately 2000 fractures were modeled using the software SYNFRAC [25-27] creating computer generated synthetic fractures, using input parameters of the fractal dimension, fracture roughness (an output of the PSD analysis of real fractures), and the standard deviation of the asperities height.

A key benefit of incorporating computer-generated synthetic fractures is the capability to work with a large amount of fracture data to perform direct fluid flow simulations, such as: i) the finite difference method [*e.g.,* 28], ii) the finite element method [*e.g.,* 29, 30], iii) the finite volume method [*e.g.,* 31], and the lattice-Boltzmann method [*e.g.,* 32]. The lattice-Boltzmann method

(LBM) describes the flow of many particles interacting with a medium and among themselves following the Navier-Stokes equation at the macroscopic scale [*e.g.,* 33]. The LBM has been implemented to compute permeability using 3D images of rocks and soft sediments obtained by micro-CT imaging techniques [34-38] and from reconstructed models [39-41] generating results consistent with laboratory measurements [40, 42]. The simplest LBM is based on the Bhatnagar-Gross-Krook (BGK) collision operator, which consists of a single relaxation time approximation [43]. Despite its widespread use, the BGK-LBM brings some issues, for example, the computed permeability values may be viscosity-dependent [44]. An alternative approach involves the use of multiple relaxation times (MRT) methods, which solve the drawbacks of the BGK method and are characterized by more stability [45-47].

In this study, the permeability values of single isolated fractures (synthetic and natural) were calculated via LBM, using the PALABOS open source library [48]. The method and the code have been previously implemented by Zambrano *et al*. [38] for quantifying the permeability in deformed porous carbonates using X-Ray microtomography synchrotron-based images [49]. Following these authors, rather than the BGK method [*e.g.,* 34], the MRT approach has been adopted in the present study to assure that permeability values are viscosity-independent.

The selected study area, the Roman Valley Quarry (Fig. 1a), is an inactive quarry located at the northern termination of the Majella Mountain (Abruzzo region, Italy). The Majella Mountain is the orogenic expression of a thrust-related anticline, with internal deformation characterized by high-angle normal, strike-slip and oblique-slip normal faults, small folds, multiple sets of opening-mode fractures, pressure solution seams, and deformation bands [50-57].

The Roman Valley quarry has been heavily studied by previous authors focusing on the structural, sedimentological and diagenetic properties [54, 56], and the fluid flow behavior of the fractured carbonates at the macroscale [13]. Here, the bitumen distribution suggests the

main hydrocarbon flow occurred through the damage zones of the principle NW-SE oriented oblique slip faults [54] (Fig. 6.1b). The distribution of major lithofacies at the Roman Valley Quarry is another element influencing the presence of bitumen which has been previously described by Rustichelli *et al*. [56] (see Table 6.1). Concerning the fractures, the most pervasive ones are represented by both pressure solution seams (often sheared with sliding/tearing mode displacement) and joints (opening mode fractures).

Considering the significance of these fractures, this work focused on investigating both cases of open mode and sheared fractures with a small sliding/tearing mode displacement, in the order of millimeters, allowing to assume a negligible wall wearing. For this last case, the mismatch between opposite walls was also computed due to its importance as a mechanism for maintaining fracture openings even at reservoirs depths.

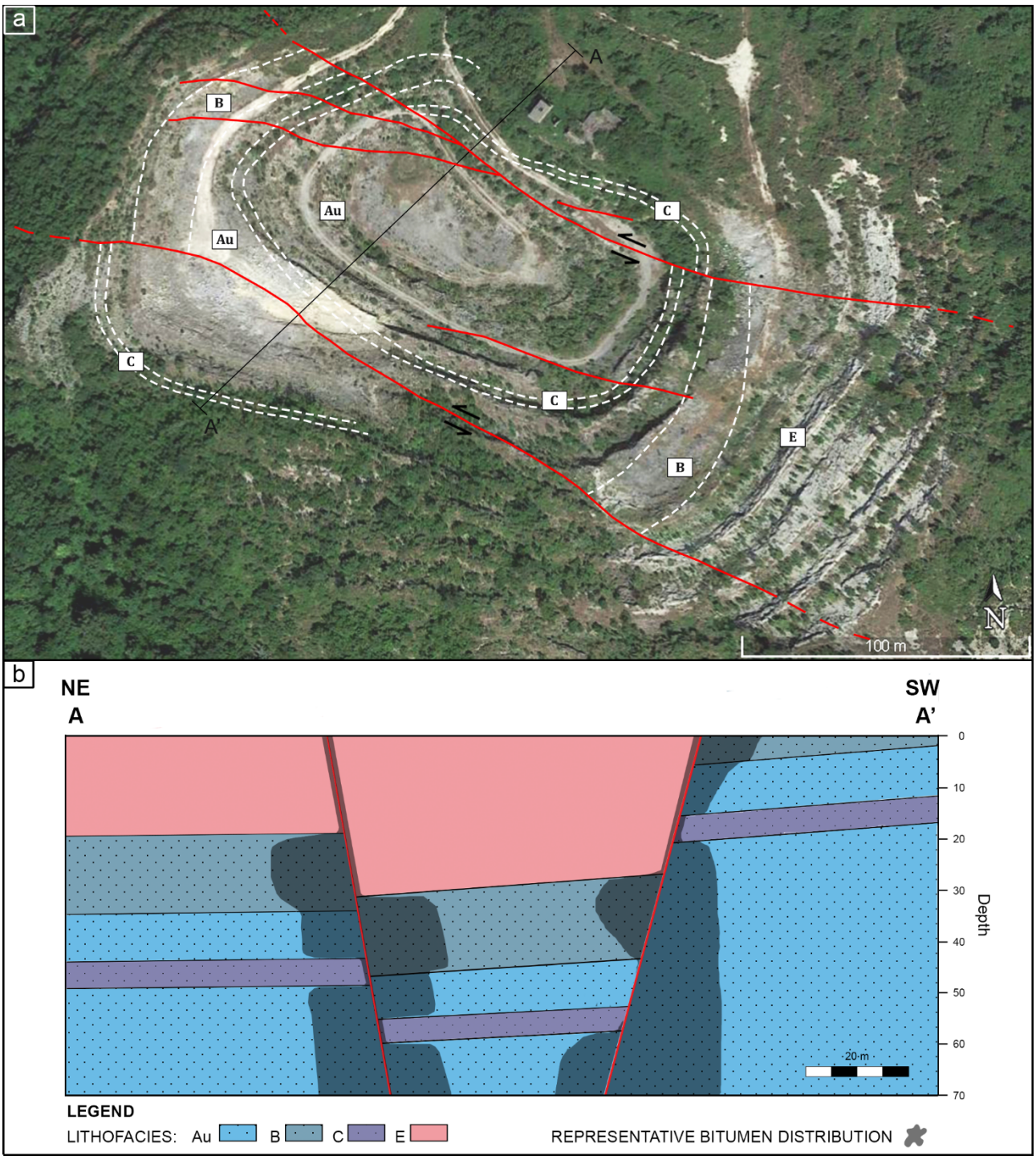

Figure 6.1. a) Structural map of the Roman Valley Quarry (modified after Volatili *et al*. [13]). Notes: red lines= faults, white dashed lines= lithofacies boundaries (see Table 6.1 for details), b) Stratigraphic and structural scheme of the study area, oil distribution is arbitrarily representative considering field observations (see Volatili *et al*. [13] for more details).

2. Methodology

In this work, we present a multi-phase integrated methodology for characterizing fracture surfaces and their effect on permeability. This approach combines fracture surface scanning using Structure from Motion photogrammetry, a statistical and spectral description of individual natural fracture surfaces, modeling of synthetic fractures, and computational calculation of permeability by fluid flow simulation.

2.1. Sample Collection

During the summer of 2018, a suite of oriented hand samples was collected from the study site comprising three (*i.e.,* Au, B, C) of the four major lithofacies of the Bolognano Formation present in the quarry (Fig. 6.2, Table 6.1). The field sampling procedure involved manually removing blocks containing fracture surfaces that showed minimal signs of physical and chemical weathering. Sampling targeted these specific lithofacies based on accessibility, quality of well-developed fracture surfaces, and the fact that they have been well documented in previous studies focused on fracture distribution and mechanical properties [13, 54, 56]. After removal from the outcrop but prior to analysis, the rock samples were cleaned using a soft-bristled brush to remove debris and other obstructions but without abrading the surface.

Table 6.1. Characteristics of lithofacies exposed in the Roman Valley Quarry

Lithofacies		Thickness	Φ_m [%]	k_m [mD]	Bitumen distribution
Au:	Alternation of medium- to coarse-grained bioclastic grainstones (Au1) and medium-grained bioclastic grainstones (Au2).	40-to 60-m	~ 27.5	83.13 (V) 160.09 (H)	Abundant in both matrix and fractures near to faults
B:	Medium-grained grainstones.	10-to 15-m	~ 26.4	444.82(V) 530.94 (H)	Abundant in both matrix and fractures near to faults
C:	Alternations of two echinoid plates and spines rich facies: fine-grained bioclastic grainstones (C1) and fine- to very fine-grained bioclastic packstones (C2). Argillaceous to marly beds (<3 cm thick) are common.	10-to 15-m	~ 10.9	~ 0.30 (V) ~ 2.51 (H)	Absent in matrix and oil stain in fractures.
E:	Alternation of two planktonic foraminifera facies: marly wackestones (E1) and marly mudstones (E2).	60–65-m	~ 28.8	~ 0.085 (V) ~ 0.081 (H)	Absent in both matrix and fractures.

Notes: Lithofacies description from Rustichelli *et al*. [56], matrix porosity (Φ_m) obtained with helium pycnometer and gas permeability (k_m) measurements (performed in both horizontal, H, and vertical, V, direction) were reported by Volatili *et al*. [13], bitumen distribution from field observations [13, 54, 56].

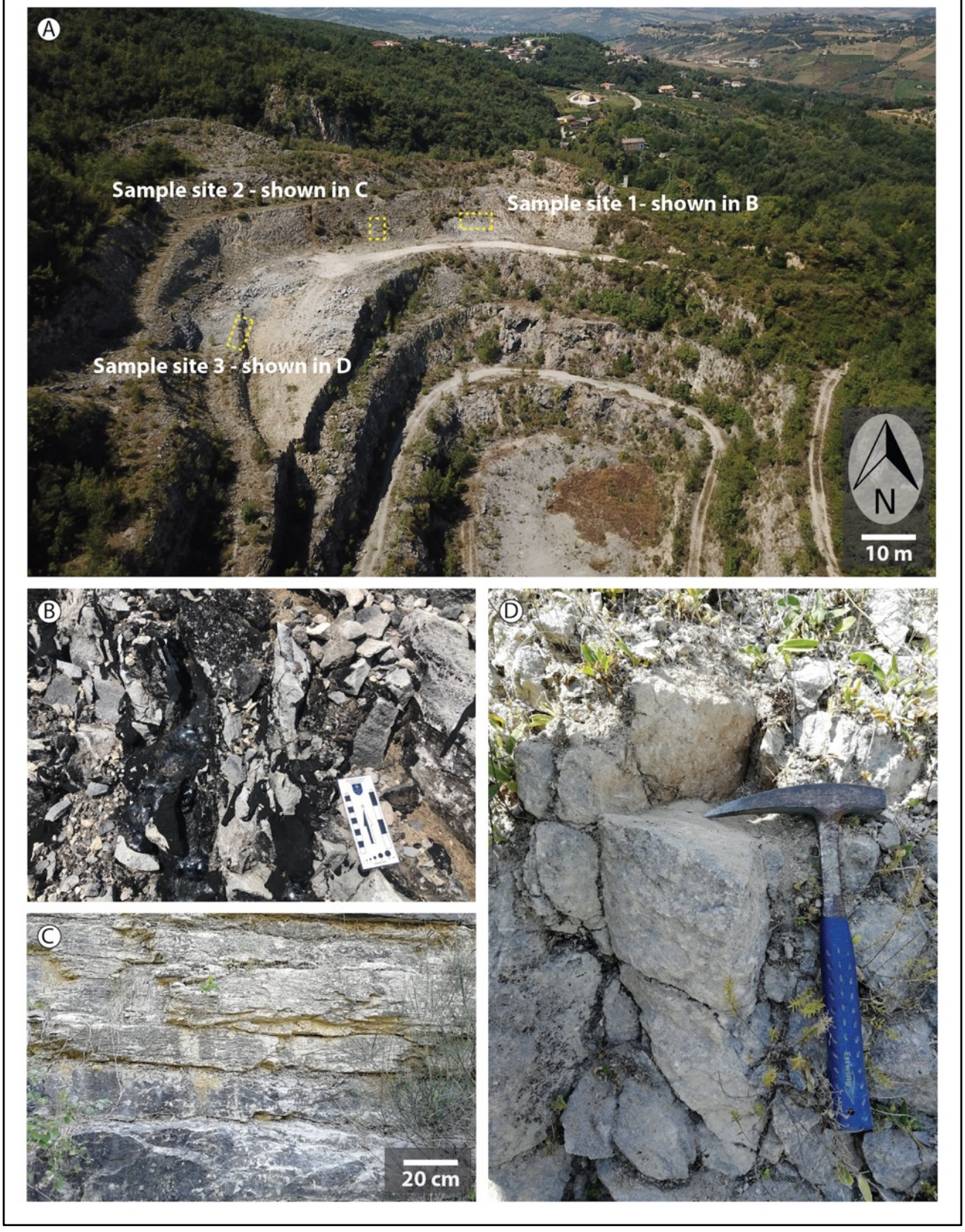
A
Sample site 2 - shown in C
Sample site 1- shown in B
Sample site 3 - shown in D
N
10 m
B
C
20 cm
D

Figure 6.2. Sample location sites. A) Sampling locations inside the Roman Valley Quarry, B) Sample site 1 from lithofacies B with scale card showing centimeter increments. C) Sample site 2 from lithofacies Au, D) Sample site 3 from lithofacies C. Rock hammer for scale, 22 cm in length.

2.2. Mapping surface topography

The workflow for mapping surface topography involves the following key stages: (1) Fracture surface image set acquisition, (2) image alignment and three-dimensional digital rock model creation using SfM.

2.2.1. Image Set Acquisition

SfM photo scanning was performed at the University of Camerino photogrammetry laboratory (Fig. 6.3a). We used a tripod-mounted Canon EOS 100D with the standard kit lens fixed at 55mm. Images of samples were recorded inside a photo-lightbox to maintain full control of camera positions, ambient lighting and to reduce shadows and glare ensuring high image quality. To achieve the desired >70% inter-photo overlap, fracture samples were placed on a 360-degree rotating stage and manually rotated at 10-degree angular increments between photos. After completing a full orbit of the object, the camera was reset at a new vertical position, and the next orbit was conducted adhering to the same 10-degree increments however offset one position from the initial starting point. This procedure was repeated along three horizontal rotations from different vertical positions followed by 2-3 photos directly above the object oriented normal to the fracture surface.

2.2.2. Image alignment and three-dimensional model creation

Fracture surface models were aligned and processed using AGISOFT PHOTOSCAN PRO (www.agisoft.com). For each fracture surface, approximately 63 photos were used as input images to create the digital point cloud model. We follow the procedure described by Carrivick *et al*. [59] and Zimmer *et al*. [24] for camera settings and photo procedure, and Pitts *et al*. [22] for image alignment and point cloud generation.

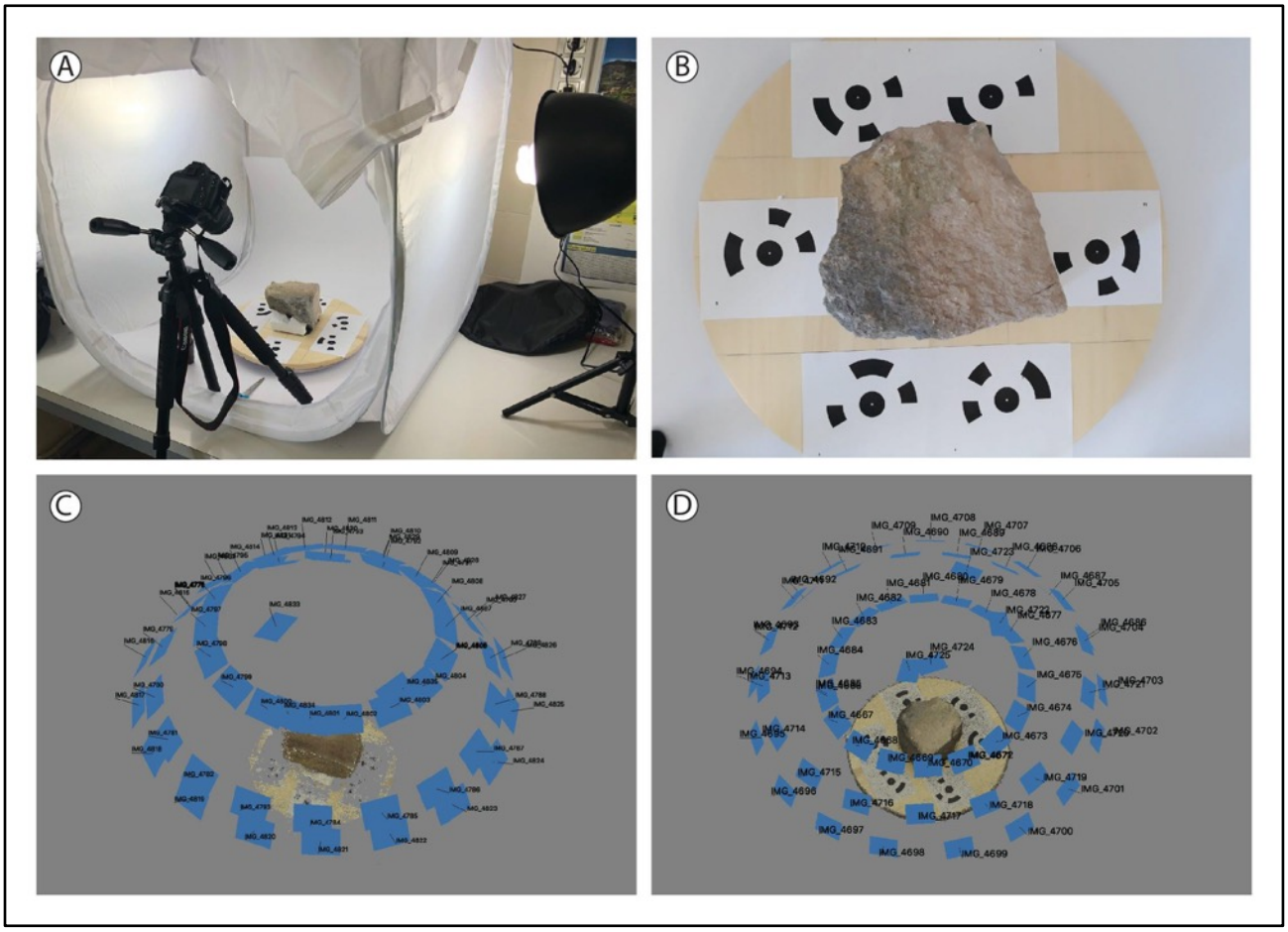

Figure 6.3. Photogrammetry setup and three-dimensional SfM procedure. A) Photo light box used in the photogrammetry lab. B) The collected sample placed on the rotating stage with unique photo-targets generated by AGISOFT PHOTOSCAN. C) Sparse point cloud generated during the photo alignment phase of the SfM procedure. D) Fully rendered photo-realistic 3D model showing camera positions.

Agisoft-generated coded targets were placed inside the scene to aid in the imagery processing, these coded targets are automatically recognized by the software and help build connection points between the image sets (Fig. 6.3 b). Additionally, a 5-centimeter scale was placed on the sample surface to calibrate the spatial reference.

As a measure to define the error of the model, we follow the methodology established by Corradetti *et al.* [19]. This calls for modeling a piece of graph paper under the same condition as fracture imaging (same light, relative distance, number of photos). Under the assumption the graph paper is perfectly planar, the standard deviation of the height of the scanned asperities is considered as the error of the model [19]. In our case, this value is approximately 20 μm, whereas the point density (points/area) is 34 points / mm.

2.3. Fracture Surface Processing and Analysis

2.3.1. Extraction and processing of 3D fracture surface model.

Trimmed 3D Point clouds were exported from Agisoft as '.xyz' text files. Then, a rectangular subregion of each fracture surface of interest was extracted from the point cloud and processed to remove undesirable trend and eventual noise (Fig. 6.4). This technique, previously documented by Corradetti *et al.* [19], consists of: i) removing the artificial trend of the surface, ii) surface interpolation, and ii) sampling in a regular grid.

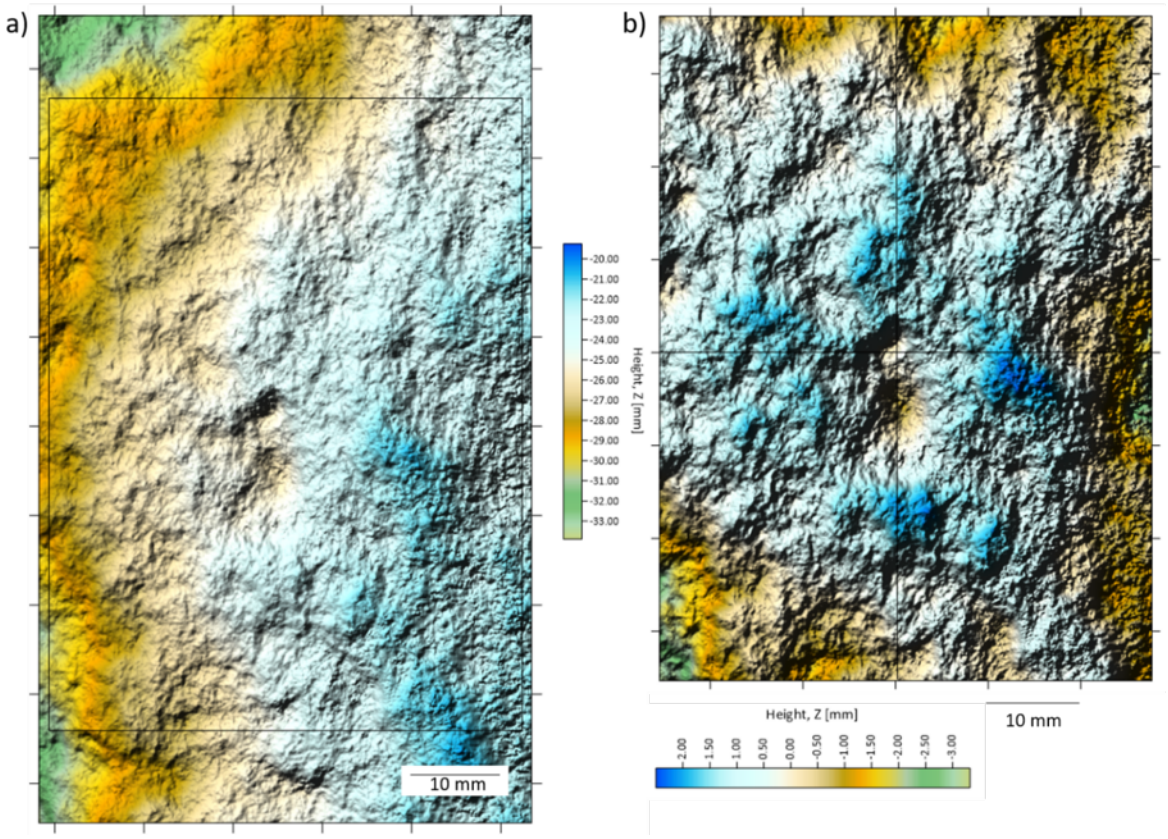

Figure 6.4. Fracture surface processing. a) Original exported fracture surface containing an artificial trend, b) resulting image after removing the artificial trend and assigning a new reference grid according to a millimeter scale.

2.3.2. Fracture roughness assessment

A complete description of the fracture roughness is given by the specification of two functions: the probability density function (depending on the media and standard deviation) for heights, and the PSD [58] (Fig. 6.5).

The Fourier power spectrum, P(k), is defined as the square of the modulus of the Fourier transform [60]. Considering a cross-section of the rock, this profile can be represented as a summation of sinusoidal components, each with its own amplitude, wavelength, and phase. The squared amplitude of each sinusoid component is referred to as its “power” (Fig. 6.5b). The

power spectrum regulated in an appropriate manner is referred to as the PSD, G (k), and it provides a valuable definition of surface roughness. The PSD as a function of k in a bi-logarithmic scale graph of a self-affine function exhibits an apparent linear slope, which is defined from the following power-law equation:

$$G(k) \propto k^{-\alpha} \quad , \qquad \text{(eq. 6)}$$

where the exponent of the power law α is related with the fractal dimension, D, (Brown, 1995), as follow:

$$D = ((7 - \alpha)) \; / \; 2 \qquad \text{(eq. 7)}$$

From a physical aspect, the fractal dimension shows the proportion of high-frequency to low frequency sinusoid components (roughness). High D values are related to greater surface roughness. By stacking and normalizing the power spectra, it is possible to reduce the noise associated with a single profile and create a single spectrum which represents the entire rough surface in each direction [*e.g.,* 15, 19]. The MATLAB script used to perform the procedures described above is partially modified from Corradetti *et al.* [19].

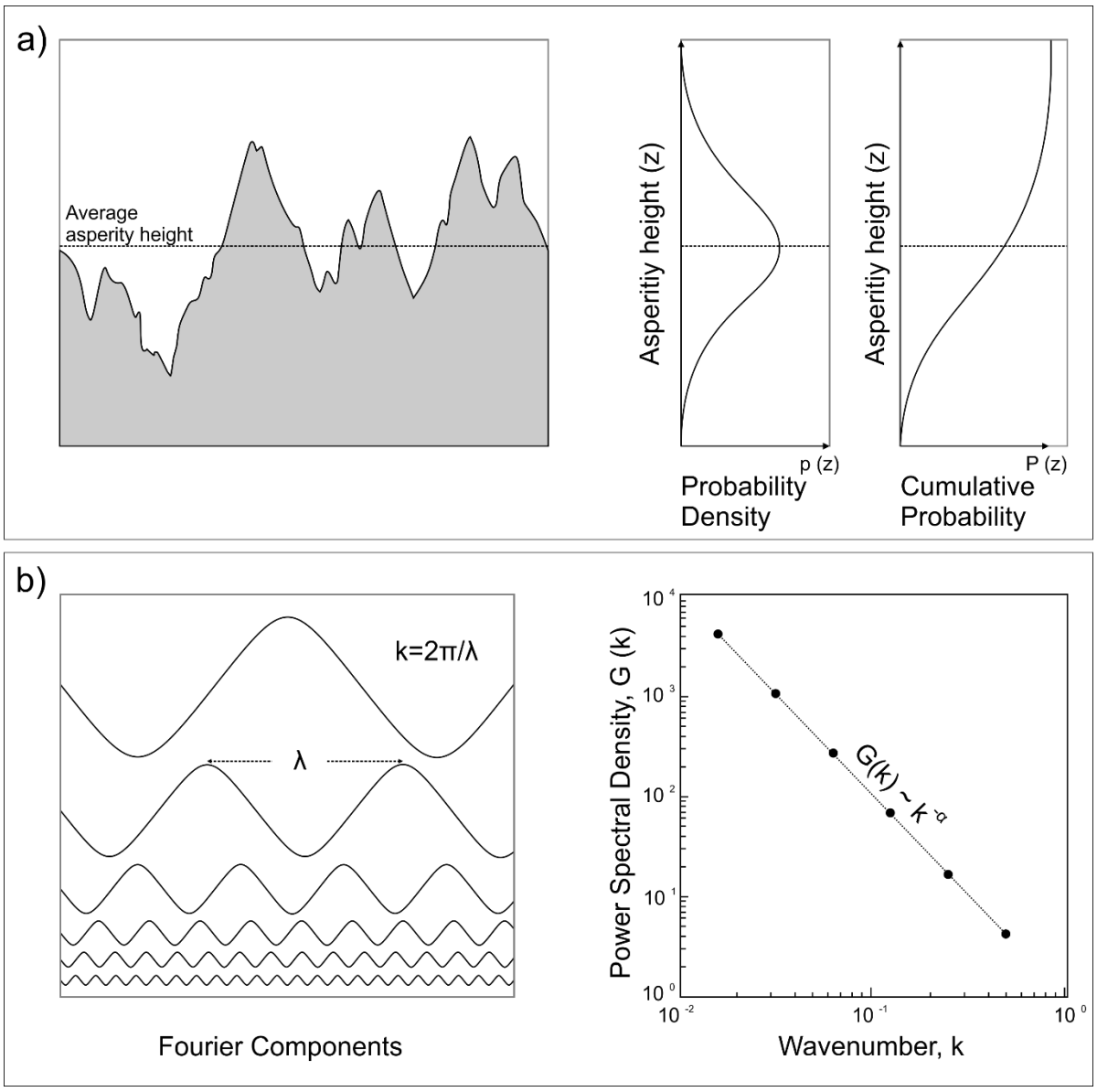

Figure 6.5. Illustration of a complete description of surface roughness: a) in terms of statistical height distribution, probability density, b) in terms of frequencies distribution, Fourier power spectrum (modified from Brown [58]).

2.4. Single Fracture Modeling

Since a limited number of natural fracture surfaces were available, additional synthetic fracture surfaces were used to strengthen the statistical significance of the results. Following the procedure described by Ogilvie [25], more than 2000 computer-generated synthetic fractures were created using the software SYNFRAC [25-27]. SYNFRAC is based on a mathematical

model of a rough surface reported by Brown (1995). The software can model open fractures by introducing mismatch values with the spatial and spectral roughness parameters. For the scope of the present study, the mismatch values were not considered for surface modeling, however, were measured after the fracture modeling (see section 2.5.1).

The individual fracture surfaces (natural and synthetic) were used to model dilation associated with (Fig. 6.6): i) opening mode displacement (joint and/or opened pressure solution seam), various ranges of aperture, and ii) sliding/tearing mode displacement (sheared joint and/or sheared pressure solution seam). In both cases, it is assumed that both walls are identical. In the second case, because the shear process is minimum, and the displacement in the order of mm, it is assumed that not physical wearing of the fracture surfaces has occurred. To illustrate different scenarios, a wide range of displacements (opening and sliding/tearing mode) were considered (The PYTHON code for fracture modeling is available at https://github.com/superrostom/synthetic-fracture).

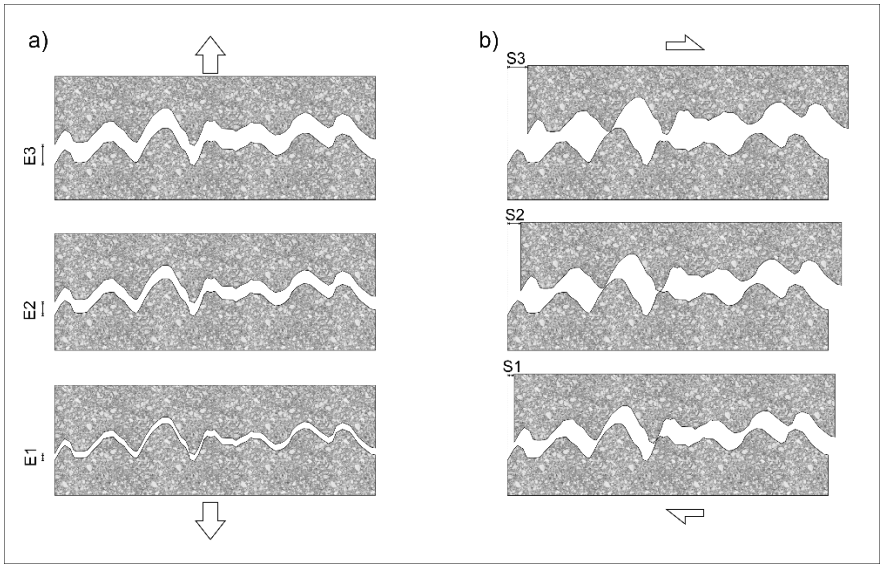

Figure 6.6. Mechanisms considered for possible fracture aperture generation in the study area: a) Opening mode displacement (joint and/or opened pressure solution seam), and b) sliding/tearing mode displacement (sheared joint and/or sheared pressure solution seam).

2.5. Lattice-Boltzmann method and permeability computation

Lattice-Boltzmann simulations were performed using the open-source computational fluid dynamics software PALABOS [48] following the methodology described by Zambrano *et al.* [38].

This procedure consists of imposing a single-phase fluid flow through a 3D porous media maintaining a fixed pressure gradient between the inlet and outlet opposing faces of the model, the rest of the faces were padded (Fig. 6.7). A bounce-back boundary condition was assigned to the fracture surfaces. An MRT collisional operator [45, 46], with a D3Q19 lattice, is used instead of the popular BGK [43] as in Degruyter *et al.* [34]. Moreover, the geometry of the media is obtained by the SfM photogrammetry outputs and modeling differently than Degruyter *et al*. [34] and Zambrano *et al.* [38] who used X-ray micro CT images.

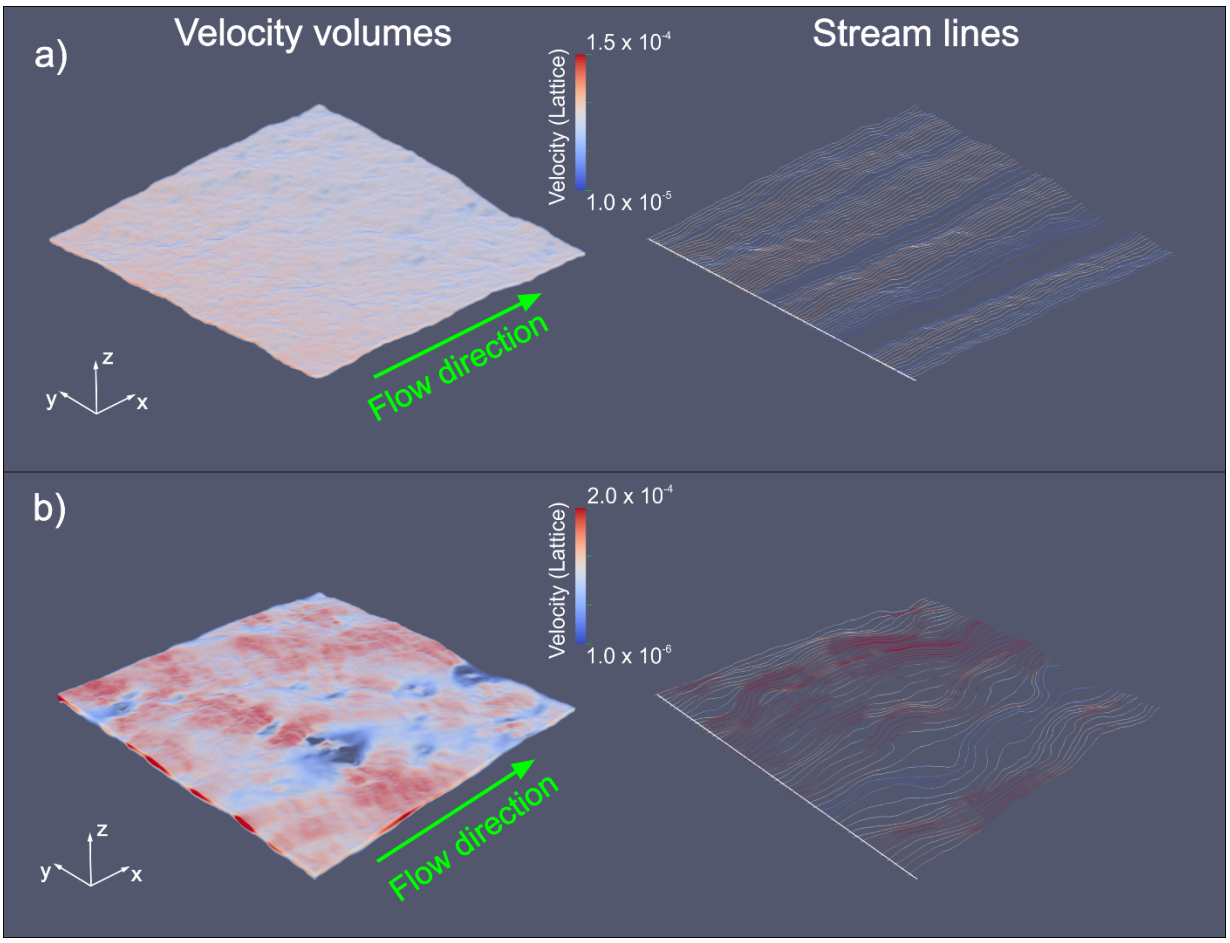

Figure 6.7. Examples of lattice velocity fields volumes with the corresponding streamlines: a) Fracture with opening mode displacement equals to 1 mm, and b) Fracture with sliding/tearing mode displacement equals to 50 mm. Both fractures have a considerable roughness (D = 2.5; Std. Dev. = 4 mm). The size of the samples is about 50 x 50 mm. Images are rendered using PARAVIEW software [61].

The simulation ended once the imposed steady state condition was reached (standard deviation of the average energy<10^{-4} after 1000 steps). Then, the permeability component parallel to the imposed flow was calculated applying Darcy's law,

$$\frac{\delta P}{\delta x} = \frac{\mu}{k} U \quad , \qquad \text{(eq. 9)}$$

where $\delta P/\delta x$ is the pressure gradient, μ the fluid kinematic viscosity, and U the average fluid velocity per unit of area. The permeability was calculated, using the same procedure, in two

orthogonal directions: along strike and along dip (k_x and k_y, respectively). In the case of sliding/tearing mode displacement, the x-direction corresponds to the slip direction. All the variables are handled in lattice units prior to permeability calculation. For convenience, permeability values were converted to millidarcy which is the most commonly used permeability unit in the oil industry. All the provided values of permeability correspond to a volume of 1.25 x 10^{-4} m^3 (50 x 50 x 50 mm^3).

2.5.1. Mismatch evaluation

The mismatch between the opposite fracture walls is of extreme importance since this factor may keep fractures open even at reservoir depths. Since the mismatch was not imposed during fracture modeling, it was measured after the generation of the synthetic fractures. The mismatch was evaluated only for the sliding/tearing mode fractures, whereas it was unnecessary in the case of opening mode fractures since the aperture is constant. For the evaluation of the mismatch value, the methodology of the Power Spectral Density ratio (PSDr), introduced by Ogilvie *et al*. [25] was followed. The methodology consists of obtaining a relationship between the PSD of the aperture and both surfaces of the fracture, as follows:

$$PSDr = \frac{PSD_{aperture}}{(PSD_{upper\_wall} + PSD_{lower\_wall})} \quad \text{(eq. 8)}$$

The results of this calculation can be represented in a graph where the parameters associated with the mismatch and the degree of mismatch between the surfaces at different wavelengths can be obtained (Fig. 6.8).

Following the definition of Ogilvie *et al.* [25], these parameters are the following:

- Minimum Mismatch Length (ML_min): Wavelength at which the fractures start to match, indicated by the wavelength where the PSD ratio values fall below its maximum value (PSDr_max).
- Maximum Mismatch Length (ML_max): Wavelength at which the fracture opposing surfaces reach the maximum matching, thus the minimum value of PSD ratio (PSDr_min).

The calculation of these parameters was made using a MATLAB code. In this case, the (ML_min) is considered as the only reliable indicator of the mismatch since the (ML_max) often falls outside the scale of the study (Fig. 6.8).

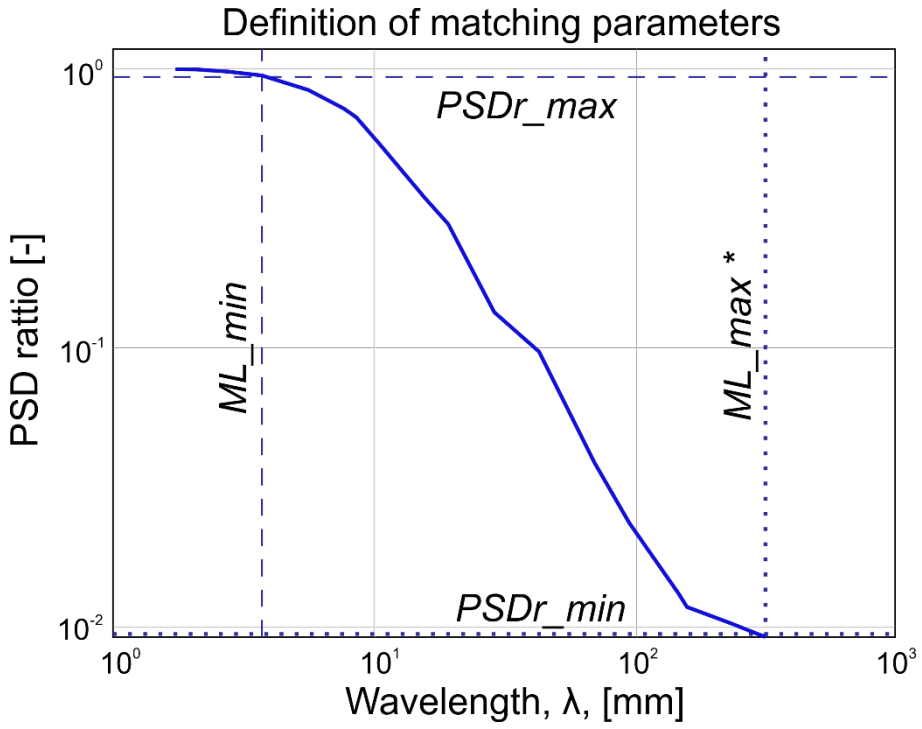

Figure 6.8. A typical PSD ratio graph use for defining the mismatching parameters. *The Maximum Mismatch Length (ML_max) often falls at the limit or outside the studied wavelength range.

3. Results

The results of this work consist of an analysis of surface topography performed on fracture samples from three lithofacies (Au, B, C), and the computed permeability in function of the fracture properties, including fractal dimension, opening and sliding/tearing displacement, and minimum mismatch length.

3.1. Fracture surface properties

In table 6.2, the values correspond to the fractal dimension (D), the average height of asperities and their standard deviation. The traditional roughness measurement, JRC, was added to compare both techniques and the results with previous works in the same outcrop. For the fracture description, we followed Agosta *et al.* [54]. The set PS2a corresponds to pressure solution seams (generated during background deformation) often sheared, with normal or left lateral kinematics, often impregnated by tar. The set PS2b corresponds to pressure solution seams (generated during background deformation) generally not-sheared.

Table 6.2. Results of the surface analysis

Field description				**Surface Analysis**			
ID	**Orientation**	**Set**	**Lithofacies**	**JRC**	**SD**	**Dx**	**Dy**
F-1	200/72	PS2a	Au	10	1.22	1.89	1.91
F-2	285/85	PS2b	Au	12	2.85	1.85	1.93
F-3	195/80	PS2a	B	9	1.49	1.90	1.78
F-4	210/V	PS2a	C-2	8	1.97	1.90	1.67
F-5	200/80	PS2a	C-1	10	1.66	1.85	1.96

F-6	120/85	PS2b	C-1	11	0.82	1.96	1.95

Notes: Orientation noted as dip direction/dip angle; SD stands for the standard deviation of asperity height, Dx and Dy are the fractals dimensions in the strike and dip directions, respectively.

3.2. Permeability results

The results of the work are presented in Figures 6.9-6.14. In each graph, the different surface roughness values (expressed in fractal dimension) are illustrated. When pertinent, error bars are added to show the variability of the results.

In the case of opening mode displacement, the results indicate the permeability increased proportionally to the mechanical aperture following a positive power-law relationship (Fig. 6.9a). Similarly, the hydraulic aperture (derived from equation 1) is related with the mechanical aperture by means of a positive power law with exponents varying from 1.6 to 1.8 for fractal dimension (D) values between 1.6 to 2.5, respectively (Fig. 6.9b).

With respect to the case of sliding/tearing displacement, the results indicate that the permeability component parallel to the displacement (k_x) increases proportionally to the sliding/tearing displacement (S_x) following a positive power-law relationship (Fig. 6.10a). The permeability component perpendicular to the displacement (k_y) is also related by a power-law with the sliding/tearing displacement (S_x). The anisotropy ratio, k_y / k_x, is generally higher for low values of fractal dimension (Fig. 6.10b). The anisotropy ratio value tends to decrease as a function of the sliding/tearing displacement (S_x) following a negative power-law relationship. The highest value of anisotropy was near 2.6 for fractal dimension (D) equal to 2.0 and sliding/tearing displacement (S_x) equal to 0.5 mm.

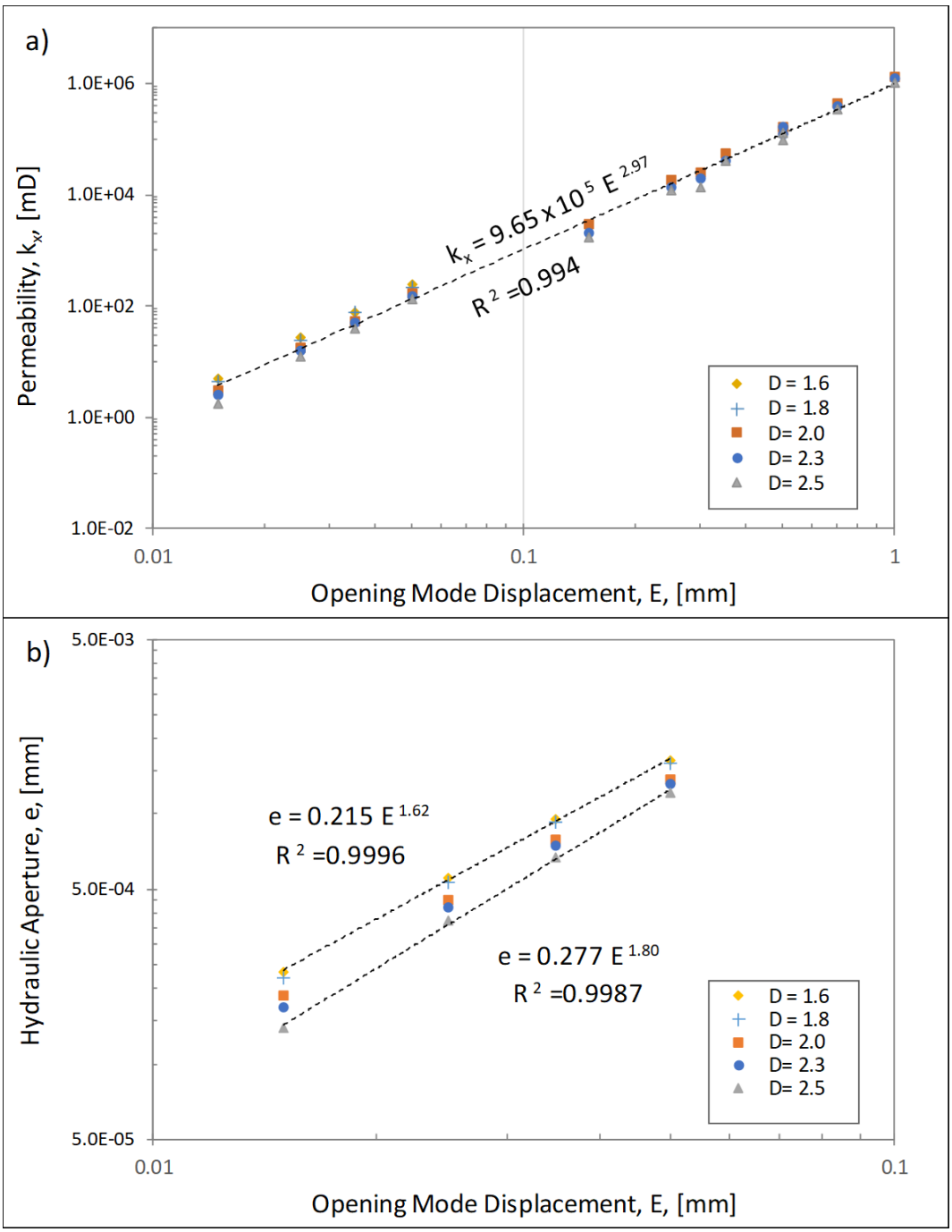

Figure 6.9. a) Single-fracture permeability versus opening mode displacement; results indicate a positive power-law relationship (nearly cubic), b) Hydraulic Aperture (computed with the equation 1) versus the opening mode displacement (mechanical aperture); the relationship follows a positive power law with exponent between 1.6 and 1.8. Axes are in logarithmic scale, and the dashed lines correspond to the best-fitting power laws.

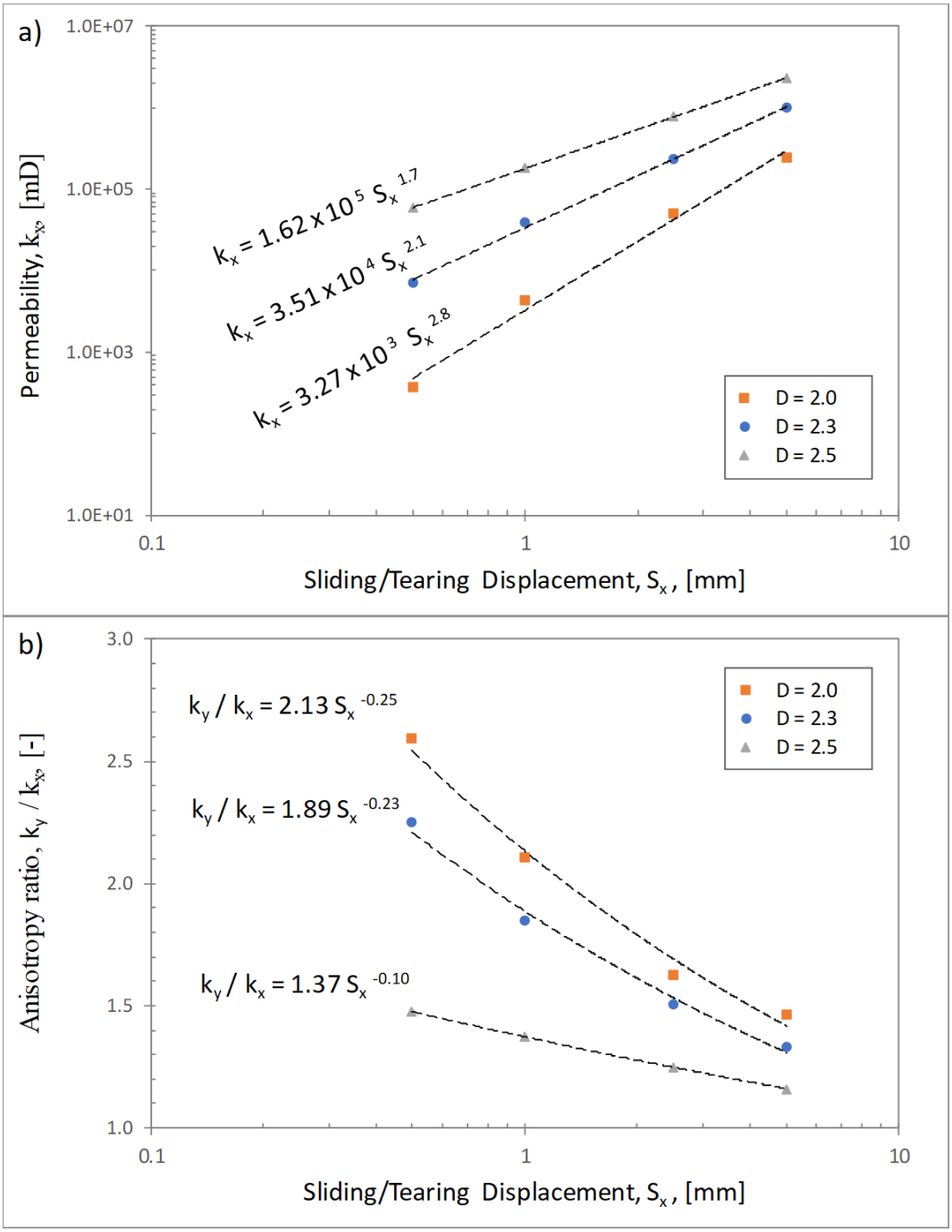

Figure 6.10. Single fracture permeability versus sliding/tearing displacement: a) permeability along the shear direction, b) Anisotropy permeability ratio, k_y / k_x, as a function of sliding/tearing displacement. Axes are in logarithmic scale, and the dashed lines correspond to the best-fitting power laws.

The fracture roughness, expressed in terms of fractal dimension (D), showed a different influence in the permeability on single fractures depending on their kinematic: opening or sliding/tearing mode. For the opening mode displacement case, the permeability is inversely proportional to the fractal dimension (Fig. 6.11a). This relationship follows a negative power-law with the slope depending on the opening mode displacement values. A higher roughness (fractal dimension) implies a decrease in permeability. For the simulated scenarios, rough fractures (D = 2.5) showed permeability values between 45% to 65% lower than smooth fractures (D = 1.6). For fractures with the sliding/tearing displacement, the permeability is proportional to the fractal dimension following a positive power-law (Fig. 6.11b). In this case, an increment of the fractal dimension (roughness) from 2.0 to 2.5 represents an enhancement of the permeability in approximately one order of magnitude.

It is expected that this positive relationship between displacement-permeability should stabilize at a certain point, as the permeability and porosity cannot increase indefinitely. This behavior is observed when the porosity is evaluated at higher displacement values (Fig. 6.11). In this case, thanks to the simplified calculation of porosity in comparison with permeability, a large volume of data was considered (more than 2000 fractures). The porosity is proportional to the sliding/tearing displacement following a non-linear relationship with variable slope. The most significant change of slope occurs near 10 mm and after approximately 30 mm of sliding/tearing displacement where the porosity seems to stabilize at values between 3% and 4%. The fractures with higher fractal dimension (roughness) tend to have higher porosity, which agrees with the permeability results. As previously mentioned, these results do not consider the possible physical wearing of the surfaces due to shearing particularly at high sliding/tearing displacement.

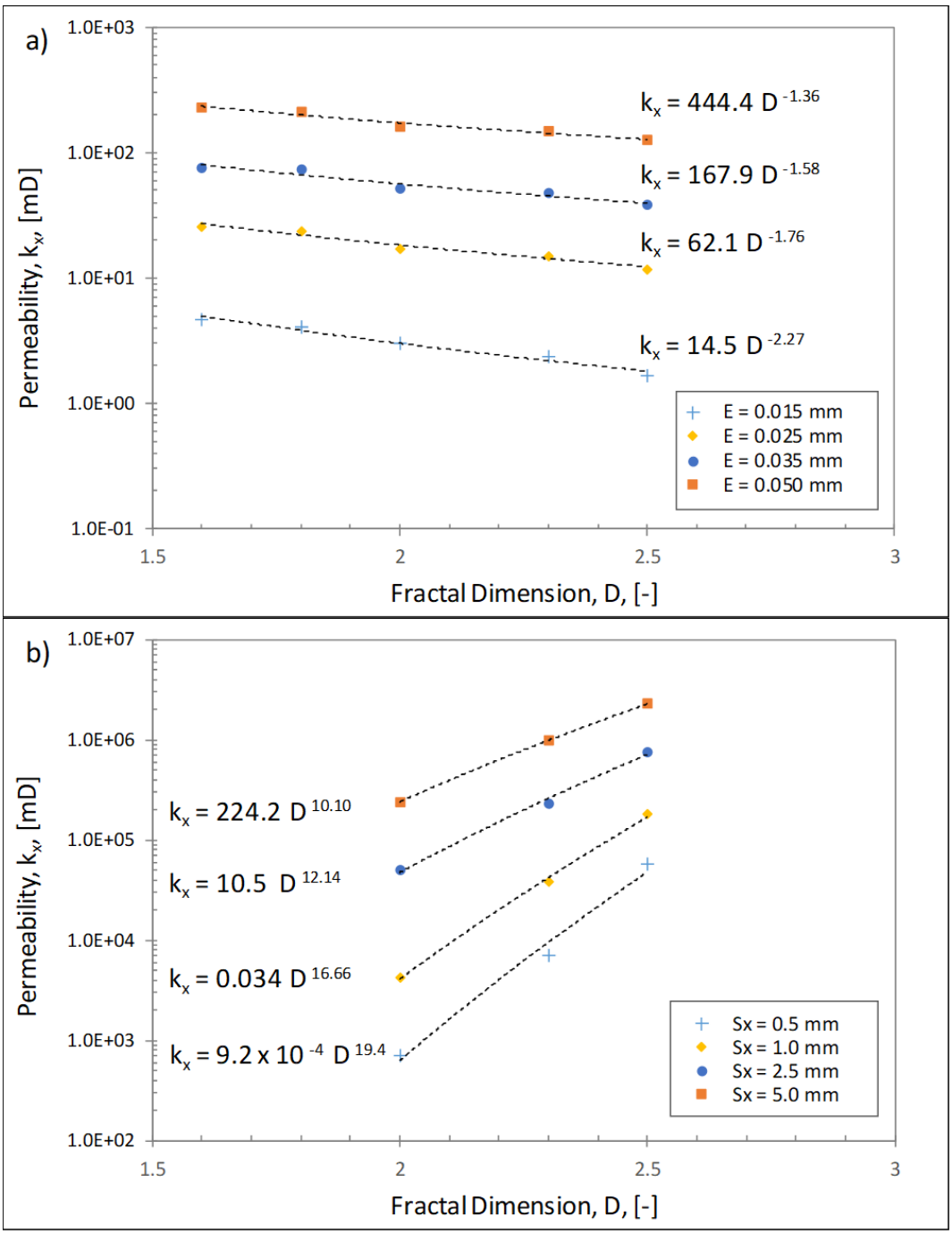

Figure 6.11. Permeability as a function of fractal dimension. a) Permeability versus open mode displacement. Note the inversely proportional control of the fractal dimension on permeability. b) permeability versus sliding/tearing displacement. Note the proportional control of the fractal dimension on permeability. Axes are in logarithmic scale, and the dashed lines correspond to the best-fitting power laws.

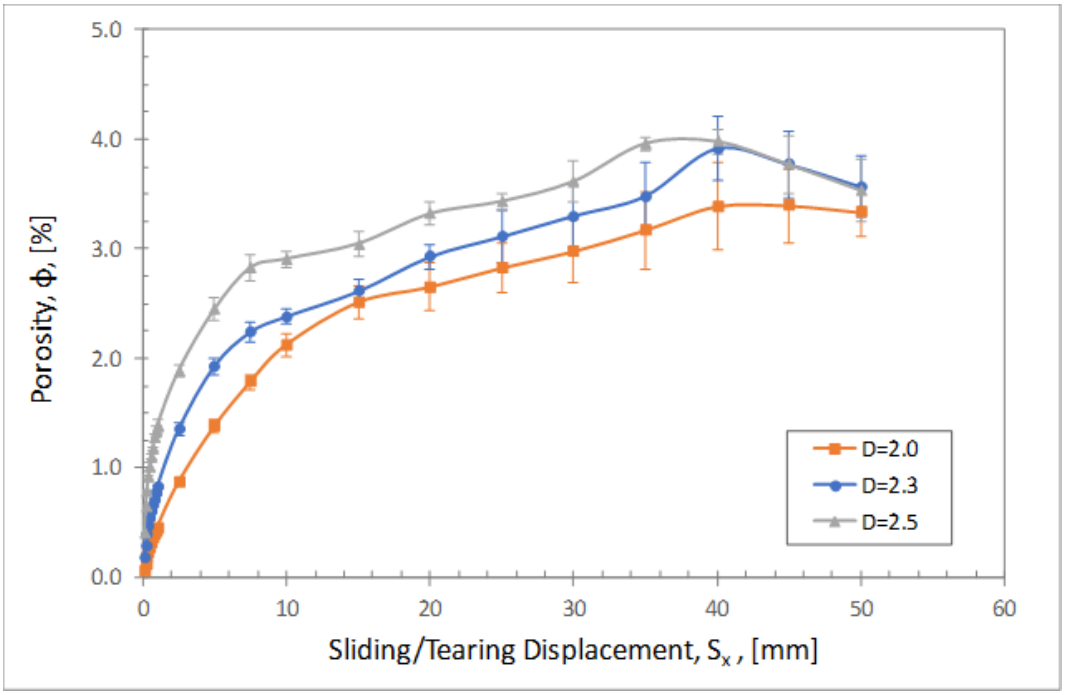

Figure 6.12. Porosity versus sliding/tearing displacement. Error bars indicate the standard error.

The fracture permeability is related to the porosity following a power law (Fig. 6.13), which differs from the theoretical relationship based on the smooth parallel-plates equation here we also assumed smooth parallel plates for the porosity). The power-law relationship seems to be unaffected by the roughness (fractal dimension). Similar behaviors where obtained for both permeability components k_x, and k_y.

The minimum mismatch length, ML_min, was evaluated as a function of the displacement (Fig. 6.14a). Results indicate that within the evaluated range (a maximum displacement of 5 mm) the minimum mismatch is linearly proportional to the displacement. The permeability is proportional to the minimum mismatch length following a power-law relationship (depending on the fractal dimension). In other words, higher values of fractal dimension imply a higher permeability for similar mismatch values.

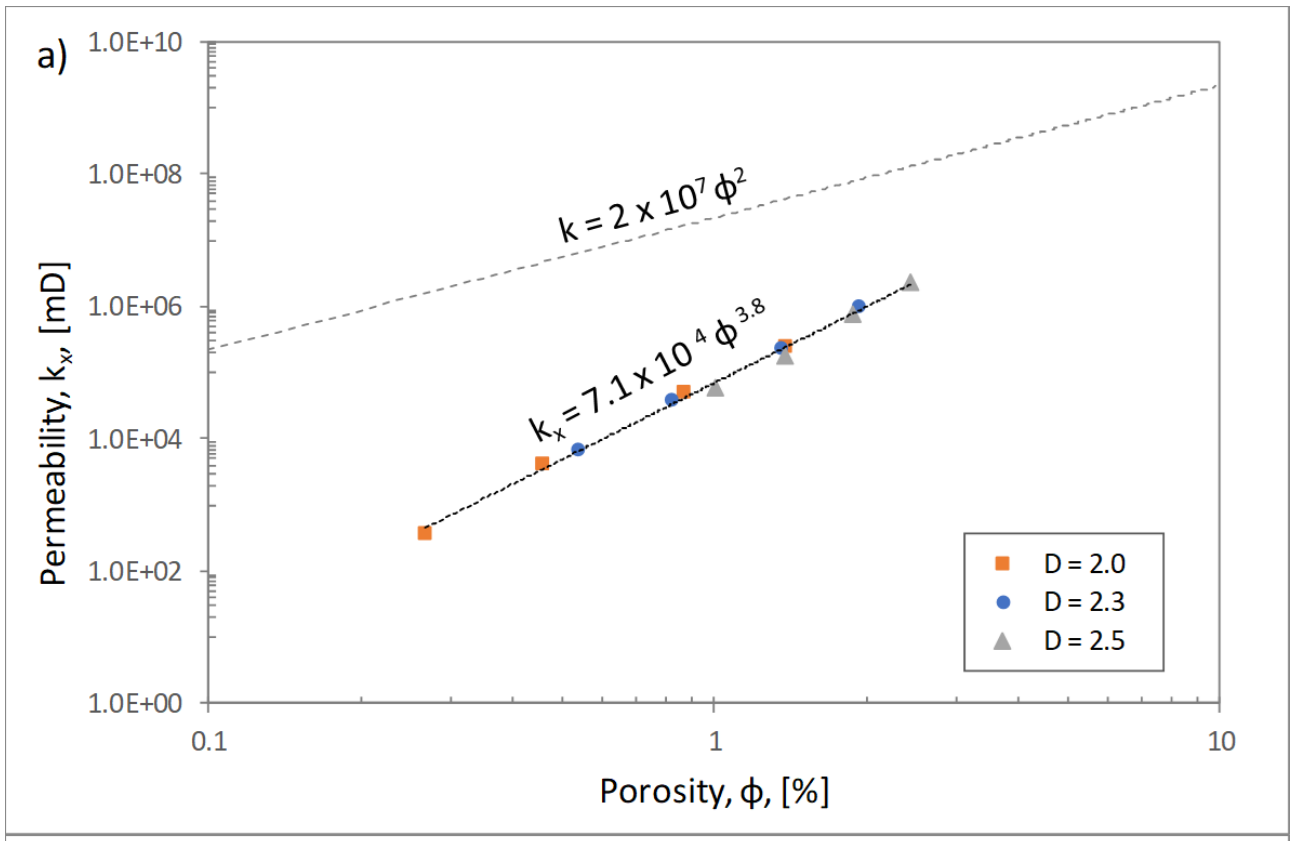
a)
1.0E+10
1.0E+08
1.0E+06
1.0E+04
1.0E+02
1.0E+00
Permeability, k_x, [mD]
$k = 2 \times 10^7 \phi^2$
$k_x = 7.1 \times 10^4 \phi^{3.8}$
D = 2.0
D = 2.3
D = 2.5
0.1
1
10
Porosity, ϕ, [%]

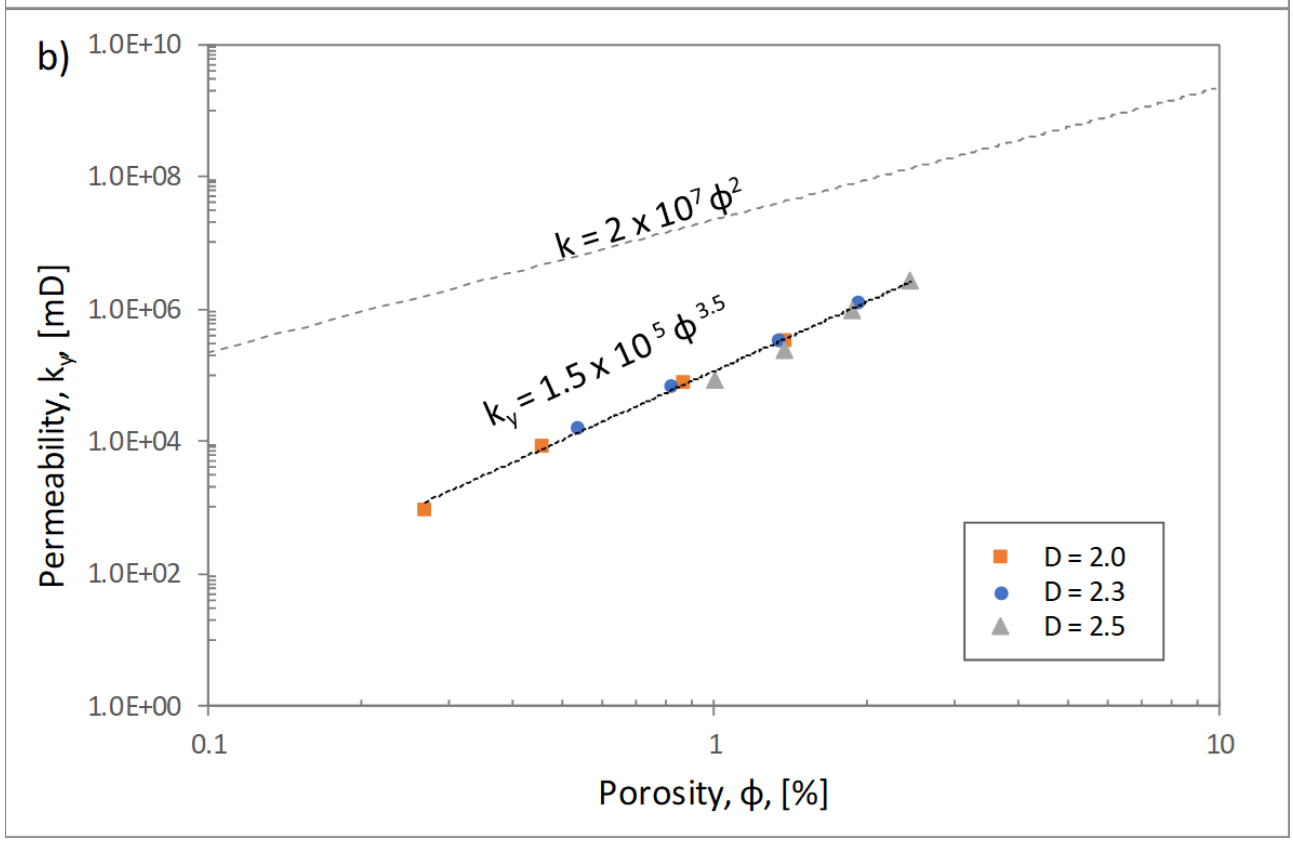
b)
1.0E+10
1.0E+08
1.0E+06
1.0E+04
1.0E+02
1.0E+00
Permeability, k_y, [mD]
$k = 2 \times 10^7 \phi^2$
$k_y = 1.5 \times 10^5 \phi^{3.5}$
D = 2.0
D = 2.3
D = 2.5
0.1
1
10
Porosity, ϕ, [%]

Figure 6.13. Permeability components – a) parallel to shear, k_x, and b) perpendicular to shear, k_y – versus porosity of a single fracture after sliding/tearing displacement. Dashed line represents the relationship permeability-porosity for ideal smooth fractures, whereas the dotted line (best-fitting power law) indicates the same relationship when roughness is included.

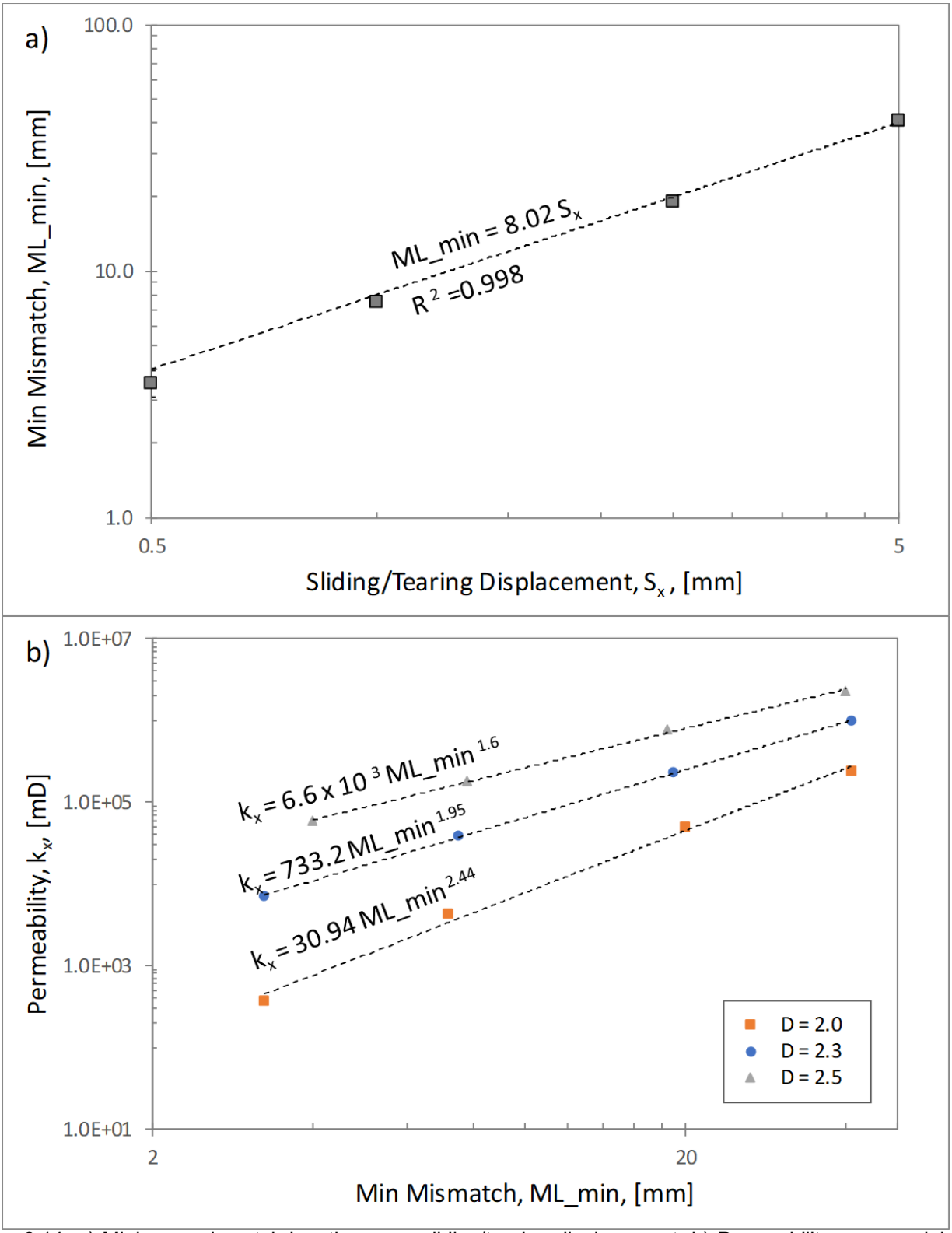

Figure 6.14. a) Minimum mismatch length versus sliding/tearing displacement, b) Permeability versus minimum mismatch length. Permeability is directly proportional to the minimum mismatch length, which is related to the shear displacement.

Discussion

The present work evaluates the effect of fracture surface features such as roughness, aperture, and mismatch on permeability using fracture surface scanning by SfM photogrammetry, numerical modeling, and lattice-Boltzmann fluid flow simulation.

3.3. SfM photogrammetry surface scanning

The results of this study demonstrate the versatility of the SfM procedure as an analytical tool which can be applied at a wide range of scales including millimeter-scale features such as fracture surfaces. The controlled conditions in the photogrammetry laboratory allowed a highly detailed scan and extraction of the micro surface topography of samples sized 30 x 30 x 30 cm producing a point clouds with a density of 34 points/mm and an estimated error of 20 μm. This method produces more realistic and applicable results than the traditional Barton Comb, with results comparable to those reported by Candela *et al*. [14], Renard *et al*. [18], and Corradetti *et al*. [19] using both Lidar or laser profilometers. However, the SfM methodology is several orders of magnitude more cost-effective and is readily accessible. A future implementation of this study could include developing a workflow suitable for in situ field studies. However, more variables need to be controlled and results yielding lower accuracy are expected.

3.4. Fracture Roughness Characterization

This methodology proved to be highly efficient in expressing the fracture roughness allowing a more accurate and representative measure with respect to the relative hydraulic roughness [4-6] or the JRC [7, 8]. However, more data is necessary for evaluating control of the lithofacies in

the fracture roughness, as it is observed for other properties such as distribution and spacing [*e.g.,* 62]-

Another important aspect of these results is the reproducibility of synthetic fractures with similar characteristics. This step was important to increase the data volumes leading to a greater statistical significance of the results and validity of the inferred relationships. The lattice-Boltzmann procedure also played a key role in this study as it allows the estimation of permeability values for controlled scenarios with different imposed properties (i.e., roughness, opening mode, and sliding/tearing displacement). This permits evaluation of the relationship between permeability, porosity, mismatch, and other imposed properties. The computed permeability may present some inaccuracy in low resolution models as previously reported by Zambrano *et al*. [38]. Therefore, permeability results may be considered not as the real values but only as approximations.

3.5. Permeability in function of fracture properties

Two situations were considered to explain the presence of open fractures: i) dilation due to opening mode displacement (joint or opened pressure solution seam) and ii) dilation due to mismatch caused by shearing and sliding/tearing displacement.

In the first case, the results followed the expectation and confirmed previous interpretations: i) permeability tends to increase with opening following a non-linear relationship, ii) a higher fractal dimension (greater roughness) correlates to lower permeability, iii) the effect of roughness is less significant at greater opening values. It is expected that higher roughness (higher frequencies of asperities) may expose a wider area in contact with the migrating fluid, diminishing its velocity due to friction. Evidently, at higher opening values this effect should be

less evident because it is the specific area (area/volume) which has a control on the permeability, as has been previously reported by Zambrano *et al*. [38] for porous media.

The second case (sliding/tearing displacement) creates an aperture due to the mismatch between the opposite walls of the fracture. We found significant differences between these two cases concerning the effect of the roughness of the permeability. In fact, the effect of roughness on permeability is inverse. Given the same displacement, fractures with higher roughness values permit the creation of larger voids and therefore enhance the fluid flow. So, the effect of friction exerted by the roughness on fluid flow has a secondary role in the case of mismatch due to sliding/tearing displacement. The continuous dilatancy of the fracture due to sliding/tearing displacement should cease at a certain value depending on the asperity frequencies present in the fracture. Nevertheless, it is difficult to verify this behavior for real fractures, where a 20 mm sliding/tearing displacement likely leads to fracture wall wearing and the generation of cataclastic material [54], eventually reducing permeability. However, our model has greater applicability to small displacements where the damage of the fracture walls is negligible.

The permeability anisotropy in fractures with sliding/tearing displacement is significant and dependent on the roughness (fractal dimension). For low displacement (0.5 mm), the anisotropy can reach values up to 2.6 for fractures with a fractal dimension of 2.0. For the same displacement, fractures with high roughness (D = 2.5) showed lower values of permeability anisotropy near to 1.5. For higher sliding/tearing displacement the permeability anisotropy decrease approaching to the value 1.

The mismatch itself has a positive control on the permeability. The importance of this result is that the mismatch could also be produced by diagenetic processes (*e.g.,* cementation, dissolution) and shearing. Zambrano *et al.* [38] using X-ray microtomographic images in shear compactive bands hosted in porous carbonates, showed the existence of complex channelized porous networks along the shear surface within these structures.

3.6. Consequences to reservoir modeling

The results agree with the macroscale observations of previous authors in the study area, where both opened/sheared pressure solution seams and fault-related joints present the greatest values of aperture and the most important bitumen impregnation [13, 54, 56].

The relationship between permeability and porosity for rough fractures clearly deviates from the ideal smooth parallel plate case (for the studied scenarios). Fracture permeability is lower for the same porosity range (< 0.2 %) in comparison to the theoretical values. Instead, the power-law slope is higher, indicating a more important control of porosity as it was expected. The equation itself may be useful to estimate the permeability of fractures if the fracture porosity is known.

After their formation, both closing and opening mode fractures are often subjected to a shear process, and even with a small imperceptible sliding/tearing displacement they cannot be modeled as simple opening mode fracture. At reservoir depth, preexisting fractures (joints and pressure solution seams) that are favorably oriented to be sheared (accordingly to the orientations of the stress field which affected the area) may be characterized by a mismatch between the fracture walls enhancing the fracture opening. Therefore, the findings of this work may have a significant impact on fracture modeling workflows for sub-resolution faults [*e.g.,* 63]. In fractures with small shear displacement, contrary to the open mode case, the roughness

may influence positively the permeability. Sliding/tearing displacement also may enhance the fracture permeability eventually decelerating when cataclasis process starts. If the shear displacement is small (S_x < 1mm), the permeability anisotropy is significant enough to be considered in the fracture modeling workflow.

4. Conclusions

We presented a new multi-faceted approach to characterize surface fracture roughness by SfM photogrammetry, numerical modeling, and computational fluid dynamics simulation. This methodology provides a better quantification of surface parameters that are not possible to obtain using former surface roughness measurement and analysis tools.

In addition, this study illustrates the crucial relationships between permeability and other fracture properties, such as roughness, porosity, opening mode-sliding/tearing displacement, and mismatch. The obtained relationships pointed out the following statements:

- In joints (opening mode fractures) and/or opened pressure solution seams, the roughness tends to reduce the permeability. Thus, the permeability is inversely proportional to the fractal dimension.
- In sheared joints and/or pressure solution seams (assuming an insignificant surface wearing) the sliding/tearing mode displacement may cause mismatch and therefore enhance the porosity and permeability. The validity of this behavior may depend on the point that displacement starts to produce cataclastic material. Small shear displacements and mismatch may be extremely important to guarantee storage and migration of geofluid at depth thanks to asperities-supported aperture. Permeability anisotropy is very significant for small shear displacements, characterized by higher values of permeability component perpendicular to the shear displacement.
- Porosity exerts a more important control on permeability in rough fractures (higher power-law slope). The empiric relationship may result in greater utility for estimating the fracture permeability if the fracture porosity is known.

Acknowledgements

This research was supported by the FAR Project 2014 “Characterization and modeling of natural reservoirs of geofluids in fractured carbonate rocks”, funded by the University of Camerino, Principal investigator Emanuele Tondi and the Reservoir Characterization Project (www.rechproject.com). We also acknowledge and thank Amerigo Corradetti for generously sharing his code for Power Spectral (PSD) analysis of surfaces and thoughtful conversations that helped move this work forward.

References

[1] Snow D., 1965. A parallel Plate Model of Fractured Permeable Media (Ph.D. thesis). Berkeley: University of California.

[2] Tsang, Y.W., 1992. Usage of "Equivalent Apertures " for Rock Fractures as Derived From Hydraulic and Tracer Tests. Water Resources Research, vol. 28, no. 5: 1451-1455.

[3] Witherspoon P, A., J. S. Y. Wang, K. Iwai, and J. E. Gale, Validity of cubic law for fluid flow in a deformable rock fracture, Water Resour. Res., 16(6), 1016-1024, 1980.

[4] Lomize, G. M., 1951. Flow in Fractured Rocks (in Russian), 127 pp., Gosenergoizdat, Moscow, 1951.

[5] Louis, C, 1969. A study of ground water flow in jointed rock and its influence on the stability of rock masses. Rock Mech. Res. Rep. 10,90 pp. Imp. Coll., London.

[6] de Quadros E.F., 1982. Determinação das características do fluxo de água em fraturas de rochas. Dissert. de Mestrado, Dept. of Civil Eng., Polytech. School, University of São Paulo (1982).

[7] Barton, N., Bandis, S. & Bakhtar, K., 1985. Strength, deformation and conductivity coupling of rock fractures. Int. J. of Rock Mech. Min. Sic., 22, 121-140.

[8] Barton, N. & Choubey, V., 1977. The shear strength of rock joints in theory and practice. Rock Mechanics, 10 (1/2), 1-54.

[9] Zambrano, M., Tondi, E., Korneva, I., Panza, E., Agosta, F., Janiseck, J.M., Giorgioni, M., 2016. Fracture properties analysis and discrete fracture network modeling of faulted tight limestones, Murge Plateau, Italy. Ital. J. Geosci. 135 (1), 55–67. https://doi.org/ 10.3301/IJG.2014.42.

[10] Panza, E., Agosta, F., Zambrano, M., Tondi, E., Prosser, G., Giorgioni, M., Janiseck, J.M., 2015. Structural architecture and Discrete Fracture Network modeling of layered fractured carbonates (Altamura Fm., Italy). Ital. J. Geosci. 134 (3), 409.

[11] Panza, E., Agosta, F., Rustichelli, A., Zambrano, M., Tondi, E., Prosser, G., Giorgioni, M., Janiseck, J.M., 2016. Fracture stratigraphy and fluid flow properties of shallow water, tight carbonates: the case study of the Murge Plateau (southern Italy). Mar. Petrol. Geol. 73, 350–370.

[12] Kim, D. H., Gratchev, I., & Balasubramaniam, A. (2013). Determination of joint roughness coefficient (JRC) for slope stability analysis: a case study from the Gold Coast area, Australia. Landslides, 10(5), 657-664.

[13] Volatili, T., Zambrano, M., Cilona, A., Huisman, B. A. H., Rustichelli, A., Giorgioni, M., Vittori, S., & Tondi, E., 2019. From fracture analysis to flow simulations in fractured carbonates: The case study of the Roman Valley Quarry (Majella Mountain, Italy). Marine and Petroleum Geology. 100, 95-110. https://doi.org/10.1016/j.marpetgeo.2018.10.040.

[14] Candela, T., Renard, F., Bouchon, M., Brouste, A., Marsan, D., Schmittbuhl, J., Voisin, C., 2009. Characterization of fault roughness at various scales: implications of three-dimensional high-resolution topography measurements. Pure Appl. Geophys. 166 (10–11), 1817–1851. http://dx.doi.org/10.1007/s00024-009-0521-2.

[15] Candela, T., Renard, F., Klinger, Y., Mair, K., Schmittbuhl, J., Brodsky, E.E., 2012. Roughness of fault surfaces over nine decades of length scales. J. Geophys. Res. 117 (B8), B08409. http://dx.doi.org/10.1029/2011JB009041.

[16] Renard, F., Voisin, C., Marsan, D., Schmittbuhl, J., 2006. High resolution 3D laser scanner measurements of a strike-slip fault quantify its morphological anisotropy at all scales. Geophys. Res. Lett. 33 (4), L04305. http://dx.doi.org/10.1029/2005GL025038.

[17] Renard, F., Mair, K., Gundersen, O., 2012. Surface roughness evolution on experimentally simulated faults. J. Struct. Geol. 45, 101–112. http://dx.doi.org/10.1016/j.jsg.2012. 03.009.

[18] Renard, F., Candela, T., Bouchaud, E., 2013. Constant dimensionality of fault roughness from the scale of micro-fractures to the scale of continents. Geophys. Res. Lett. 40 (1), 83–87. http://dx.doi.org/10.1029/2012GL054143.

[19] Corradetti, A., McCaffrey, K., De Paola, N., & Tavani, S., 2017. Evaluating roughness scaling properties of natural active fault surfaces by means of multi-view photogrammetry. Tectonophysics, 717, 599-606.

[20] Bemis, S. P., Micklethwaite, S., Turner, D., James, M. R., Akciz, S., Thiele, S. T., & Bangash, H. A., 2014. Ground-based and UAV-Based photogrammetry: A multi-scale, high-resolution mapping tool for structural geology and paleoseismology. J. Struct. Geol. 69, 163–178.

[21] McCaffrey, K. J. W., Jones, R. R., Holdsworth, R. E., Wilson, R. W., Clegg, P., Imber, J., ... & Trinks, I., 2005. Unlocking the spatial dimension: digital technologies and the future of geoscience fieldwork. J. Geol. Soc. London. 162, 927–938.

[22] Pitts, A. D., Casciano, C. I., Patacci, M., Longhitano, S. G., Di Celma, C., & McCaffrey, W. D., 2017. Integrating traditional field methods with emerging digital techniques for enhanced outcrop analysis of deep-water channel-fill deposits. Marine and Petroleum Geology, 87, 2-13.

[23] Nesbit, P. R., Durkin, P. R., Hugenholtz, C. H., Hubbard, S. M., & Kucharczyk, M., 2018. 3-D stratigraphic mapping using a digital outcrop model derived from UAV images and structure-from-motion photogrammetry. Geosphere. 14(6). DOI: 10.1130/GES01688.1

[24] Zimmer, B., Liutkus-Pierce, C., Marshall, S. T., Hatala, K. G., Metallo, A., & Rossi, V., 2018. Using differential structure-from-motion photogrammetry to quantify erosion at the Engare Sero footprint site, Tanzania. Quaternary Science Reviews, 198, 226-241.

[25] Ogilvie, S. R., Isakov, E., & Glover, P. W., 2006. Fluid flow through rough fractures in rocks. II: A new matching model for rough rock fractures. Earth and Planetary Science Letters, 241(3-4), 454-465.

[26] Isakov, E., Ogilvie, S. R., Taylor, C. W., & Glover, P. W., 2001. Fluid flow through rough fractures in rocks I: high resolution aperture determinations. Earth and Planetary Science Letters, 191(3-4), 267-282.

[27] Ogilvie, S. R., Isakov, E., Taylor, C. W., & Glover, P. W. J., 2003. Characterization of rough-walled fractures in crystalline rocks. Geological Society, London, Special Publications, 214(1), 125-141.

[28] Blunt, M. J., Bijeljic, B., Dong, H., Gharbi, O., Iglauer, S., Mostaghimi, P., Paluszny, A., and Pentland, C. H., 2013. Pore-scale imaging and modeling. Adv. Water Resour., 51, 197–216.

[29] Cardenas, M.B., 2008. Three-dimensional vortices in single pores and their effects on transport. Geophys. Res. Lett. 35, L18402. https://doi.org/10.1029/ 2008GL035343.

[30] Cardenas, M.B., 2009. Direct simulation of pore level Fickian dispersion scale for transport through dense cubic packed spheres with vortices. Geochem. Geophys. Geosyst. 10, Q12014. https://doi.org/10.1029/2009GC002593.

[31] Bijeljic, B., Raeini, A., Mostaghimi, P., Blunt, M.J., 2013. Predictions of non-Fickian solute transport in different classes of porous media using direct simulation on pore-scale images. Phys. Rev.E 87 (1), 013011. https://doi.org/10.1103/PhysRevE. 87.013011

[32] Sukop, M.C., Huang, H., Lin, C.L., Deo, M.D., Oh, K., & Miller, J.D., 2008. Distribution of multiphase fluids in porous media: Comparison between lattice Boltzmann modeling and micro-x-ray tomography. Physical Review E, 77(2), 026710.

[33] Ladd, A. J. C., 1994. Numerical simulations of particulate suspensions via a discretized Boltzmann equation: Part 2. Numerical results, J. Fluid Mech., 271, 311-339.

[34] Degruyter, W., Burgisser, A., Bachmann, O., Malaspinas, O., 2010. Synchrotron X-ray microtomography and lattice Boltzmann simulations of gas flow through volcanic pumices. Geosphere, v. 6, no. 5, p. 470-481, doi: 10.1130/GES00555.1.

[35] Khan, F., Enzmann, F., Kersten, M., Wiegmann, A., Steiner, K., 2012. 3D simulation of the permeability tensor in a soil aggregate on basis of nanotomographic imaging and LBE solver. J. Soils Sediments 12, 86–96. http://dx.doi.org/10.1007/s11368-011-0435-3.

[36] Andrä, H., Combaret, N., Dvorkin, J., Glatt, E., Han, J., Kabel, M., Keehm, Y., … Zhan, X., 2013. Digital rock physics benchmarks—part II: computing effective properties. Comput. Geosci. 50, 33–43. http://dx.doi.org/10.1016/j.cageo.2012.09.008.

[37] Shah, S.M., Gray, F., Crawshaw, J.P., Boek, E.S., 2015. Micro-computed tomography pore scale study of flow in porous media: effect of voxel resolution. Adv. Water Resour. 000, 1–12. http://dx.doi.org/10.1016/j.advwatres.2015.07.012.

[38] Zambrano, M., Tondi, E., Mancini, L., Lanzafame, G., Trias, F.X., Arzilli, F., Materazzi, M., Torrieri, S., 2018. Fluid flow simulation and permeability computation in deformed porous carbonate grainstones. Adv. Water Resour. 115. https://doi.org/10.1016/j. advwatres.2018.02.016.

[39] Jin, G., Patzek, T.W., Silin, D.B., 2004. Direct prediction of the absolute permeability of unconsolidated consolidated reservoir rock. In: Proceedings of the SPE annual technical conference exhibition, Houston, TX. (SPE 90084)

[40] Keehm, Y., Mukerji, T., Nur, A., 2004. Permeability prediction from thin sections: 3D reconstruction and Lattice-Boltzmann flow simulation. Geophys. Res. Lett., 31, L04606, doi:10.1029/2003GL018761.

[41] Wu, K., Dijke, M.I.J., Couples, G.D., Jiang, Z., Ma, J., Sorbie, K.S., Crawford, J., Young, I., Zhang, X., 2006. 3D stochastic modeling of heterogeneous porous media - applications to

reservoir rocks. Transp. Porous Media 65, 443–467. http://dx.doi.org/10.1007/ s11242-006-0006-z.

[42] Keehm, Y., 2003. Computational rock physics: Transport properties in porous media and applications, Ph.D. Dissertation, 135 pp., Stanford Univ., Stanford, Calif.

[43] Bhatnagar, P.L., Gross E.P., Krook M., 1954. A model for collision processes in gases. I: small amplitude processes in charged and neutral one-component system. Phys. Rev. 94, 511-525

[44] Narvaez, A., Zauner, T., Raischel, F., Hilfer, R., and Harting, J., 2010. Quantitative analysis of numerical estimates for the permeability of porous media from lattice-Boltzmann simulations, J. Stat. Mech., 11, P11026.

[45] d'Humières, D., 1992. Generalized Lattice-Boltzmann equations, in: Rarefied Gas Dynamics: Theory and Simulations, Prog. Astronaut. Aeronaut., vol. 159, edited by B. D. Shizgal and D. P. Weave, pp. 450-458, AIAA, Washington, D. C.

[46] d'Humières, D., Ginzburg, I., Krafczyk, M., Lallemand P., and Luo., L-S., 2002. Multiple-Relaxation-Time Lattice Boltzmann Models in Three Dimensions, Phil. Trans. R. Soc. A, 360, 437-451.

[47] Pan, C., Luo, L.S., & Miller, C.T., 2006. An evaluation of lattice Boltzmann schemes for porous medium flow simulation. Computers & fluids, 35(8), 898-909.

[48] Latt, J., 2009, Palabos, Parallel Lattice Boltzmann Solver: http://www.lbmethod.org/palabos/

[49] Zambrano, M., Tondi, E., Mancini, L., Arzilli, F., Lanzafame, G., Materazzi, M., & Torrieri, S., 2017. 3D Pore-network quantitative analysis in deformed carbonate grainstones. Marine and Petroleum Geology, 82, 251-264.

[50] Ghisetti, F. & Vezzani, L., 2002. Normal faulting, extension and uplift in the outer thrust belt of the central Apennines (Italy): role of the Caramanico fault. Basin Research, 14, 225-236.

[51] Scisciani, V., Tavarnelli, E., & Calamita, F. 2002. The interaction of extensional and contractional deformation in the outer zones of the Central Apennines, Italy. Journal of Structural Geology, 24, 1647-1658.

[52] Tondi, E., Antonellini, M., Aydin, A., Marchegiani, L., Cello, G., 2006. The role of deformation bands, stylolites and sheared stylolites in fault development in carbonate grainstones of Majella Mountain, Italy. J Struct Geol, 28: 376-391, doi:10.1016/j.jsg.2005.12.001.

[53] Lavenu, A. P., Lamarche, J., Salardon, R., Gallois, A., Marié, L., & Gauthier, B. D., 2014. Relating background fractures to diagenesis and rock physical properties in a platform–slope transect. Example of the Maiella Mountain (central Italy). Marine and Petroleum Geology, 51, 2-19.

[54] Agosta, F., Alessandroni, M., Tondi, E., Aydin, A., 2009. Oblique-slip normal faulting along the northern edge of the Majella anticline: inferences on hydrocarbon migration and accumulation. J. Struct. Geol. 31, 674–690.

[55] Aydin, A., Antonellini, M., Tondi, E., Agosta, F., 2010. Deformation along the leading edge of the Majella thrust sheet in central Italy. J. Struct. Geol. 32, 1291e1304. http://dx.doi.org/10.1016/j.jsg.2008.10.005.

[56] Rustichelli, A., Tondi, E., Agosta, F., Di Celma, C., Giorgioni, M., 2013. Sedimentologic and diagenetic controls on pore-network characteristics of Oligocene-Miocene ramp carbonates (Majella Mountain, central Italy). Am. Assoc. Petrol. Geol. Bull. 97, 487e524

[57] Iadanza, A., Sampalmieri, G., & Cipollari, P., 2015. Deep-seated hydrocarbons in the seep “Brecciated Limestones” of the Maiella area (Adriatic foreland basin): Evaporitic sealing and oil

re-mobilization effects linked to the drawdown of the Messinian Salinity Crisis. Marine and Petroleum Geology, 66, 177-191.

[58] Brown, S. R., 1995. Simple mathematical model of a rough fracture. Journal of Geophysical Research: Solid Earth, 100(B4), 5941-5952.

[59] Carrivick, J. L., Smith, M. W., & Quincey, D. J., 2016. Structure from Motion in the Geosciences. John Wiley & Sons.

[60] Schuster, A., 1898. On the investigation of hidden periodicities with application to a supposed 26-day period of meteorological phenomena. J. Geophys. Res. 3 (1), 13. http://dx.doi.org/10.1029/TM003i001p00013.

[61] Ahrens, J., Geveci, B., Law, C., 2005. ParaView: An End-User Tool for Large Data Visualization, Visualization Handbook, Elsevier, ISBN-13: 978-0123875822

[62] Rustichelli, A., Agosta, F., Tondi, E., & Spina, V. (2013). Spacing and distribution of bed-perpendicular joints throughout layered, shallow-marine carbonates (Granada Basin, southern Spain). Tectonophysics, 582, 188-204.

[63] Antonellini, M., Cilona, A., Tondi, E., Zambrano, M., & Agosta, F. (2014). Fluid flow numerical experiments of faulted porous carbonates, northwest Sicily (Italy). Marine and Petroleum Geology, 55, 186-201.

Chapter

7

Discussions and Conclusions

Discussion

This collection of works highlight some of the useful applications of SfM photogrammetry in geosciences

Benefits of SfM

The first and most important measure of the benefits is the cost. This tool is cheap enough that it is accessible for most university research groups and can even be purchased out of pocket if research funding is lacking. Considering that the price of entry level UAV systems with 12Mb onboard cameras is nearly equal to that of an entry level DSLR hand camera, this platform is accessible to most people.

Operation of the UAV and photogrammetry techniques are easy to learn and can be aided by flight planning software and open source apps that can help systematize data collection.

3D data returns from SfM provide x,y,z point cloud data that also includes RGB color info with each point. This is preferred to LIDAR returns that provide 3D point clouds without any color data. Color data can be critical, especially for sedimentology and stratigraphy applications where lithological units can be inferred from color.

This data can easily be turned into digital elevation models (DEMS), Orthomosaic, and many other data exports that can function with other geodata analysis tools, such as GIS software, and virtual outcrop analysis software.

With careful attention, the approach can provide data density and resolution equal to or greater than laser scanning.

Limitations of SfM

This thesis finds several issues with the use of Airborne and ground-based SfM. One challenge is collecting data at ranges longer than 100 meters. This is resolved by using an

airborne platform; however, they also have their limitations which means that the drone can often not approach an outcrop at the same proximity that a human can.

Secondly, SfM data collections can suffer from external aspects beyond the control the surveyor, such as inconsistent lighting, climatic changes, shadows, and overpowering lighting. This creates a situation where drone survey flights can be very difficult to repeat in the exact same manner when the survey is flown manually. The use of flight planner software and apps can resolve this, but these flight planners are not exactly suitable for all survey missions. Some flight plans have very specific obstacles and data acquisition requirements that require the careful touch of an expert pilot.

Processing 3D data presents two large challenges. One, in that data processing takes so long - the time required to process a large outcrop of greater that 500 photos can last several days in order to render the model at the highest resolution. Computers with greater processing power represent the solution - the data for this project was processed on a workstation with 128GB of RAM and 10Gb of dedicated memory to the graphics card. At the time of producing this thesis, this is considered very large for a university research workstation, and the processing times involved still lasted for several days. The second drawback of processing times involved in this type of work is that the processing can only be done “back at the lab”. This means it is difficult to check field data before leaving the area of research and, if there is a systematic error in the photo sets, such as incorrectly placed photo settings, a corrupt memory unit, or some other irregularity, this can lead to the detection of the error too late.

There are many different types of software that are available for processing data and making secondary annotations and interpretations, though there are not many standard visualization tools for the data. In some cases, due to the immense file sizes, it is not possible to render the point cloud or surface data.

In order to render the model at the highest resolution, better processing computers present the solution. The data for this project was processed on a workstation with 128 GB of ram and 10Gb of dedicated memory to the graphics card and at the time of producing this thesis is

considered very large for a university research workstation, and the processing times involved were lasting several days. The second drawback of processing times involved in this type of work is that the processing can only be done " back at the lab" this means it is difficult of check field data before leaving, if there is systematic error in the photos sets such as incorrectly placed photo settings or corrupt memory unit, or some other irregularity, this can lead to the detection of the error too late.

Since many different software is available for processing data and making secondary annotations and interpretations, there are not many standard visualization tools for the data. In some cases, due to the immense file sizes it is not possible to render the point cloud or surface data.

"Late Breaking" Applications of SfM and Digital Geologic Content for Geoscience Education

In the time span of just a few months following the submission and review of this thesis, the novel COVID-19 virus emerged as a global pandemic. The impact of the virus touched nearly every aspect of daily life including geoscience education. This thesis considers the use of SfM photogrammetry as a supplementary tool for field analysis which can enhance data sets by allowing access and perspectives that would be otherwise unreachable. However, during these past few months, the need for sharable digital geologic content has become increasingly more important, if not vital, for geoscience education. In fact, many of the 3D geologic models, Gigapans, and other digital geologic content has been repurposed for an upcoming international cooperative course titled " Virtual Field Experiences and Digital Geologic methods in the Apennines" which will be co-run by the University of Camerino and George Mason University for a pilot group of 6 US-based students. This package of digital content will provide the basis for teaching the fundamental concepts of outcrop analysis, geologic mapping, and Apennine regional geology. While this course was created in a very short period out of necessity, current trends may suggest the increasing need for digital, online-accessible geologic teaching content. Additionally, repurposing of research content into teaching tools increases the dissemination of knowledge and allows the research findings to be shared with students in more accessible format.

Conclusions

This Doctoral thesis provides a detailed application on SfM MVS, intended for geoscience research applications in sedimentology, stratigraphy, structural geology, geologic mapping, petroleum geology. The uses here breakdown into four different case studies which apply this approach at different scales and with modified instrumentation for the appropriate study. These results are summarized here:

In Chapter 3, *Integrating traditional field methods with emerging digital techniques for enhanced outcrop analysis,* the approach for SfM acquisition was applied using a handheld consumer-grade DSLR camera shot from a helicopter flying at more than 200m above the outcrop. Virtual outcrop models from this site were used to capture the broad scale geometry turbidite channels and yielded results providing meter-scale resolution. In addition, photos were taken from ground-level in order to link the large scale architecture with bed-scale features. These data helped the interpretation of depositional architecture and bedding geometry with greater certainty. This study showed how facies characterization and high-resolution stratigraphic correlation can greatly benefit by the use of these emerging digital data collection techniques. The combined methodology proposed in this chapter provides solutions to the challenges involved with outcrop characterization by creating observation points from perspectives and distances that are not physically possible in the field. Furthermore, these digital outcrop reconstructions allow researchers to return from the field with a record of the study area, which can be used to support the verification of additional interpretations during the analysis of data. While this case-study focuses on the applications of this approach as a tool for enhanced sedimentary facies analysis, the methodologies discussed here can be useful in a broad range of geoscience research applications (e.g., for the creation of high-resolution DTM's), particularly where the sole use of traditional field data collection tools is not sufficient to provide a complete perspective of the broad geological context.

In Chapter 4 *Detailed outcrop characterization of high frequency sequence boundaries in the Pliocene Peri-Adriatic shallow marine succession revealed through UAV cliff-side digital outcrop mapping,* SfM acquisition was achieved using a UAV (drone) outfitted with a 12 megapixel camera and an onboard GPS system. Results from this data acquisition method

provide the means to evaluated meter– decameter scale resolution with enabled the analysis and characterization of bed-scale sedimentary structures and stratigraphic surfaces. The data from this study enabled the interpretation of meter-scale to decameter-scale shallow marine cyclicity linked to high-frequency sequences linked to shoreline transgressive shifts linked to relative sea-level change.

At this study site the limited access and the general poor quality of the outcrop where acessible offer an incomplete interpretation. And in the rare cases of fresh exposures, the perspectives often do not permit the optimum view or proximity to observe subtle yet extremely important sedimentological and stratigraphic details. The interpretations here in this work, such as onlap strata terminations were discovered only through the use of UAV outcrop scanning which was then calibrated with the measured-reference section. This study highlights the many benefits of this approach, however, the UAV-SfM generated VOM model still contained some limitations. The first is that it is still difficult to create virtual outcrop models that contains the absolute 1:1 equivalent resolution as the input photos. This implies that the VOM is best used in conjunction with the outcrop-referenced input photos that can help to improve the interpretations.

In Chapter 5, *Sedimentological and Stratigraphic signature of the Plio-Pleistocene tectonic events in the Southern Apennines, Italy. The Calvello Basin case study,* the SfM approach was performed by UAV-based aerial photogrammetry scanning inaccessible outcrops and searching for previous unidentified exposures. This was used in conjunction with geologic mapping, sedimentary facies analysis, and structural analysis of syn-sedimentary faults. Specifically the UAV imagery was analyzed using VRGS software to extract quantitative geologic data from outcrops such as bedding and fault orientations. The accuracy of these measurements when tested against physically acquired measurements at the same location was within 2-5 degrees. The new perspectives on outcrops acquired by aerial UAV data allowed the recognition of sedimentary structures that have improved the interpretations of depositional setting and relationships to the tectonic development of the Calvello Basin and its role in the larger evolution of the Southern Apennines.

In Chapter 6, *Analysis of fracture roughness control on permeability using SfM and fluid flow simulations: Implications for carbonate reservoir characterization*, the SfM approach was

applied to a close-range setting. The data acquisition was set up in a highly controlled setting using a tripod, camera photo box, and a rotating stage individuated into 10-degree increments. In contrast to the previous data acquisition setups, which were taken in more a less a random and un-oriented manner, this study was well controlled and calibrated for specific camera positions in order to produce millimeter scale results. The data from this study achieved accuracy of .02 millimeters in order to characterize the micro-topography of fracture surfaces. In addition to achieving specific goals of the study of characterizing surface fracture roughness, it also served as a trial to understand the resolution limits of SfM photogrammetry. This approach proved to be an effective means of characterizing surface irregularities leading a more accurate and realistic description of fracture surface roughness to evaluate reservoir quality in carbonate reservoirs.

Considering the results of these 4 case studies, SfM photogrammetry proved to be a versatile tool which may be calibrated to function from a helicopter, or drone UAV, from ground based perspective, and also for microscopic features in the lab setting. This study employed this technique at distances from the subject of interest ranging from several hundred meters to 10-15 centimeters, proving that this method is a scale-independent method that can be easily adjusted depending on the desired spatial resolution of the subject. For different research intentions, this technique could also be upscaled to apply to satellite imagery, or similarly downscaled to microscopic images such as SEM.

As photographic technology and computer processing power continues to accelerate, in the future, this technique will likely continue to expand in suitability to other research efforts.